SLAC-66
UC-34, Physics
TID-4500 (48th Ed.)

NEUTRON-PROTON ELASTIC SCATTERING FROM 1 TO 6.3 GEV

July 1966

M. N. Kreisler

Technical Report
Prepared Under
Contract AT(04-3)-515
for the USAEC
San Francisco Operations Office

Printed in USA. Price $4.00. Available from CFSTI, National Bureau of Standards, U. S. Department of Commerce, Springfield, Virginia.

ACKNOWLEDGMENTS

It is a pleasure to acknowledge the assistance of the many people who made this experiment possible.

Professor Martin L. Perl, advisor to this project, is to be thanked not only for his supervision, support, and guidance during the course of the experiment, but also for his willingness to discuss and help solve the many problems associated with the experiment. Dr. Michael Longo and Smith Powell III from the University of Michigan and Fred Martin from SLAC are to be thanked for all their efforts in the design and execution of all phases of the experiment.

The author is grateful for the very able assistance from Mr. T. R. Elder, Mr. O. Haas, Mr. J. Moss, and Mr. R. Seefred during the setup and execution of the experiment. The assistance of T. Elioff, W. Hartsough, K. Lou, and the entire Bevatron staff is also acknowledged.

The members of the scanner group at SLAC--K. Eymann, S. Faulk, R. Lumactod, and M. Slattery--are to be thanked for the superb job of scanning and measuring that they did. The author is grateful for conversations with Professor J. Ballam, Dr. W. B. Johnson, Dr. R. Larsen, and Dr. T. Tan.

The machine shop at SLAC under the direction of R. Atherton built parts of the equipment for the experiment. Mr. I. Zavialoff designed the rail system and the magnet support. Mr. A. Barna and Mr. R. Carman are to be thanked for their help with electronics. M. Corey, G. Gavenman, and R. Levine are to be thanked for their conversations about computer programs.

The work on this experiment was supported in part by the U. S. Atomic Energy Commission and the U. S. Office of Naval Research Contract NONR 1224(23). In addition, the author would like to thank the National Science Foundation for its support.

The author would also like to acknowledge the continued support and encouragement from his wife, Barbara.

TABLE OF CONTENTS

LIST OF TABLES

Page

LIST OF ILLUSTRATIONS

Page

I. INTRODUCTION

Study of elastic scattering of strongly interacting particles has been used in the investigation of strong interaction physics. A great deal of experimental and theoretical effort has been put forth in this study. This effort has been motivated by the desire to learn something about the internal structure of the strongly interacting particles and about the mechanism of strong interactions. The theoretical effort has been further motivated by a desire to explain the experimental results. The study of elastic scattering has focused on a large number of strongly interacting systems, namely, pp, π^+p, π^-p, K^+p, K^-p, and $\bar{p}p$.[1] Unfortunately, despite this large effort there has been no great success in understanding elastic scattering. As Orear[2] said at the start of a lecture on strong interactions:

> "...I wish to summarize the present experimental situation in high energy scattering, mainly of pions and protons. I shall try to emphasize some common features and some differences along with various theoretical interpretations. This talk may not be too clear because at present the theory is not too clear."

In view of the theoretical difficulties, it is somewhat surprising to note that there has been relatively little experimental investigation at high energies of another strongly interacting system, the neutron-proton system. Such investigation could, perhaps, throw some light on the problem.

The n-p system has been measured in great detail for energies at or below 400 MeV.[3] There are only a handful of experiments between 400 and 1000 MeV, many of which cover only small angular regions in the center-of-mass system, and there are almost no experiments above 1 GeV. This lack of experiments is in large measure due to the difficulty of obtaining monochromatic neutron beams, the presence of large inelastic backgrounds, and the problem of constructing efficient, reliable high energy neutron detectors.

This paper presents the results of an experiment[4] to measure the differential cross section of the n-p system from 1 to 6.3 GeV using a new technique involving a neutron beam containing a broad spectrum of neutron energies, a liquid hydrogen target, and spark chambers.

In Section II, the experimental results for energies less than 1 GeV are discussed. Some of the present theories and models of elastic scattering are presented in Section III as well as a discussion of the few n-p measurements above 1 GeV. In Sections IV, V, VI, and VII, the experiment from 1 to 6.3 GeV is discussed, and in Sections VIII, IX, and X the results are presented and compared to the theoretical predictions.

II. PREVIOUS INVESTIGATIONS OF NEUTRON-PROTON SCATTERING ABOVE 400 MeV

The n-p differential cross sections at 580, 590 and 630 MeV were measured in great detail by N. S. Amaglobeli and Yu. M. Kazarinov.[5,6] The neutron beam consisted of the neutrons produced in the forward direction by bombarding a beryllium target with protons. The energy spectrum of this beam had a half-width of 130 MeV. Following a scattering in a liquid hydrogen target, the neutron was detected with an array of five scintillation counters and a block of polyethelyne which "converted" the neutrons into protons. By placing absorbers in between the counters, the minimum energy detectable could be varied. Great care had to be taken to avoid systematic errors, as the neutron detector was found to have only a one to two percent efficiency. In the region where the recoil proton had sufficient energy, the cross sections were determined by observing the proton rather than the scattered neutron. In order to present the total angular distributions, the portions of the cross sections measured in these two manners were "joined" at a given angle in the center-of-mass system. Absolute normalization was obtained by using the total elastic cross section, which was taken as the difference between the total n-p cross section and the total pion production cross section. As shown in Fig. 1, their data imply that the cross section is quite symmetric around 90° in the center-of-mass system.

G. Martelli et al.[7] measured the ratio of the 90° cross sections for p-p and n-p scattering at three energies between 600 and 1000 MeV. The measurement was made by detecting and momentum analyzing protons scattered from various targets. The cross sections were then obtained by appropriate subtractions. The p-p cross sections were the difference between scattering from polyethelyne

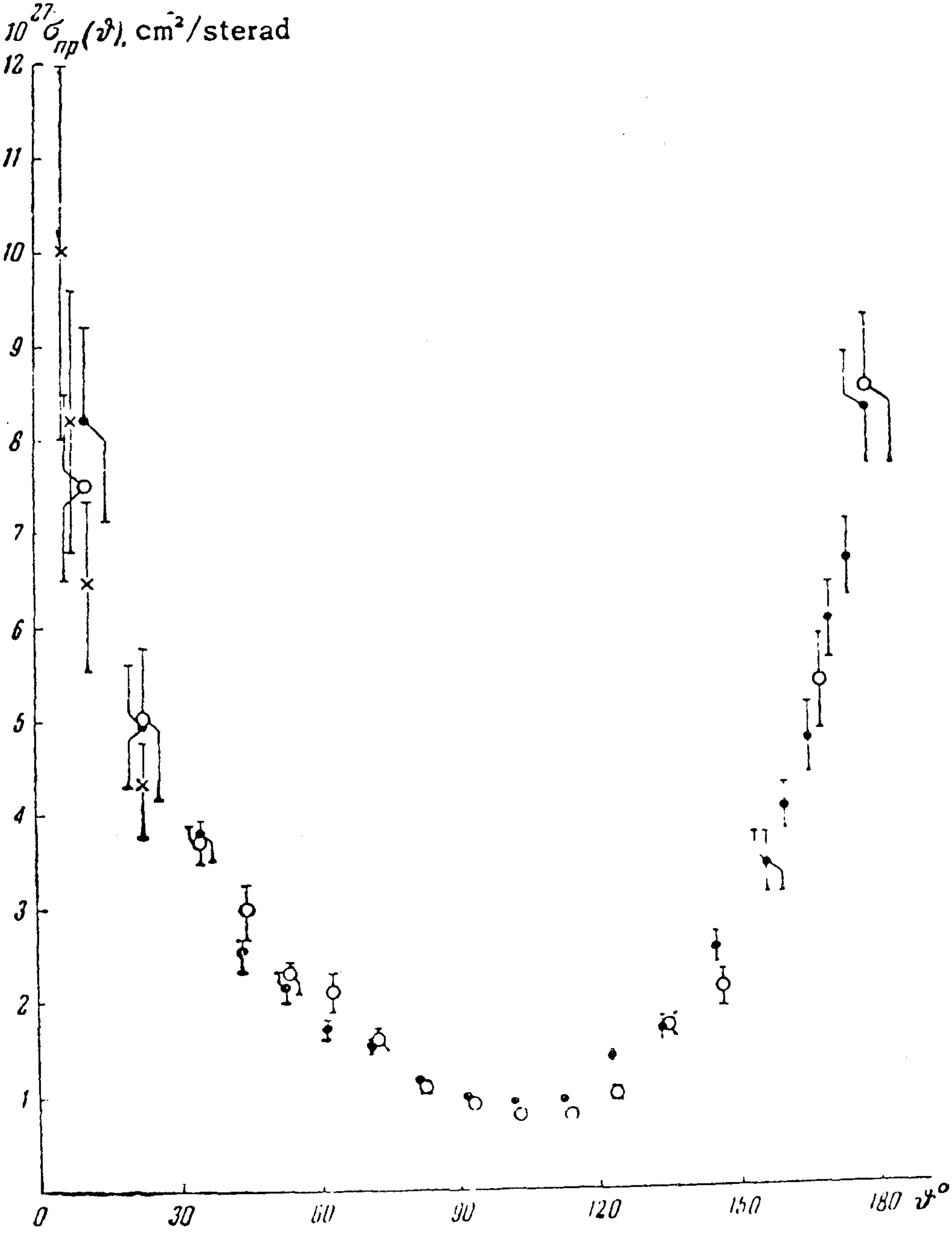

FIG. 1--Neutron-proton elastic scattering differential cross sections at 580, 590, and 630 MeV (from N. S. Amaglobeli and Yu. M. Kazarinov, Ref. 6). The cross sections approach symmetry around 90°.

and carbon and the n-p cross sections were determined from heavy water and water. The ratios obtained were:

$$\frac{\left.\frac{d\sigma}{d\Omega}\right|_{90^{o}} \text{(pp)}}{\left.\frac{d\sigma}{d\Omega}\right|_{90^{o}} \text{(np)}} = \begin{cases} 3.04 \pm 0.56 \text{ at } 595 \text{ MeV} \\ 1.00 \pm 0.18 \text{ at } 775 \text{ MeV} \\ 0.683 \pm 0.097 \text{ at } 1010 \text{ MeV} \end{cases}$$

R. R. Larsen[8] measured the distributions at 710 MeV covering center-of-mass angles from 160^{o} to 180^{o}. The neutron beam was produced by using a proton beam and a deuterium target. It was possible to obtain the energy spectrum of the neutron beam from an analysis of protons emitted from the deuterium at the same angle as the neutrons. The scattering took place in a liquid hydrogen target and the recoil proton was detected and velocity analyzed. Inelastic contaminations limited this experiment to angles greater than 160^{o}. A peak in the distribution near 180^{o} was found, and this "charge exchange" peak will be discussed later.

These measurements are the major experimental efforts in n-p elastic scattering for energies above 400 MeV. The few experiments above 1 GeV which were concerned with scattering near 180^{o} will be discussed later.

III. REVIEW OF THEORETICAL AND EXPERIMENTAL ASPECTS OF HIGH ENERGY SCATTERING

Consider the elastic scattering of two particles

$$A + B \longrightarrow A + B$$

which can be represented by the Feynman graph:

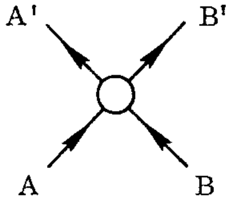

The invariant quantities that will be used are:

$$t = \left(\overset{4}{\vec{P}}_A - \overset{4}{\vec{P}}_{A'} \right)^2 \quad = \text{(four-momentum transfer)}^2$$

$$s = \left(\overset{4}{\vec{P}}_A + \overset{4}{\vec{P}}_B \right)^2 \quad = \text{(total center-of-mass energy)}^2$$

where $\overset{4}{\vec{P}}_i$ is the momentum four vector of the ith particle. If p is the momentum in the center-of-mass system and θ is the scattering angle,

$$\begin{aligned} t &= -2p^2 (1-\cos\theta) \approx -p^2 \theta^2 \text{ for small } \theta \\ s &= \left\{ \left(p^2 + m_A^2\right)^{1/2} + \left(p^2 + m_B^2\right)^{1/2} \right\}^2 \end{aligned} \tag{1}$$

The units are defined such that $\hbar = c = 1$. All kinematic quantities will refer to the center-of-mass system unless otherwise specified.

The discussion of elastic scattering is divided into four parts, each one covering a small region of the angular distributions.

A. Small Angle Elastic Scattering

The high energy differential cross sections of all the strongly interacting systems that have been measured so far exhibit a very predominant forward peak. This peak, which occurs for values of $|t|$ less than 1.0 $(\mathrm{GeV/c})^2$, can be understood in terms of an optical model[9] in which all spin effects are ignored.

Schiff[10] shows that in the center-of-mass system, the differential elastic cross section can be expressed as

$$\frac{d\sigma}{d\Omega} = \left| f(\theta) \right|^2 \tag{2}$$

where $f(\theta)$ is the scattering amplitude. This amplitude can be expanded in terms of a sum over partial waves with orbital angular momentum quantum numbers ℓ as:

$$f(\theta) = \sum_{\ell} \frac{(2\ell+1)\left[\exp(2i\delta_\ell') - 1\right]}{2ip} P_\ell(\cos\theta) \tag{3}$$

$P_\ell(\cos\theta)$ are the Lengendre polynomials of order ℓ, normalized such that

$$\int_{-1}^{1} P_\ell(x)\, P_{\ell'}(x)\; dx = \frac{2}{2\ell+1}\, \delta_{\ell\ell'}$$

δ_ℓ' is the phase shift and expresses the effect of the scattering potential on the wave function.

Absorption or inelastic effects can be included by letting the phase shift δ_ℓ' become complex, that is,

$$\delta'_\ell = \delta_\ell + i\beta_\ell$$

Thus,

$$f(\theta) = \frac{1}{2ip} \sum_{\ell} (2\ell+1) \left(\eta_{\ell} e^{2i\delta_{\ell}} - 1\right) P_{\ell} (\cos \theta) \tag{4}$$

$$\eta_{\ell} = e^{-2\beta_{\ell}} \quad \text{and} \quad 0 \leq \eta_{\ell} \leq 1$$

We note that $\eta_{\ell} = 1$ is just elastic scattering with no absorption and $\eta_{\ell} = 0$ implies complete absorption of the ℓ^{th} partial wave by inelastic processes.

The optical model that will be used consists of the assumptions that

$$\eta_{\ell} = \begin{cases} \eta & \ell \leq L_{\max} \\ 1 & \ell > L_{\max} \end{cases} \tag{5}$$

$$\delta_{\ell} = 0$$

Therefore,

$$f(\theta) = \frac{1}{2ip} (\eta - 1) \sum_{\ell=0}^{L_{\max}} (2\ell + 1) P_{\ell} (\cos \theta) \tag{6}$$

These assumptions can be interpreted in terms of an absorbing black disk that has a maximum impact parameter or radius R such that

$$R = L_{\max}/p \tag{7}$$

For the case that $L_{\max} \gg 1$, we have[11]:

$$\sum_{\ell=0}^{pR} (2\ell + 1) P_{\ell} (\cos \theta) \approx 2 \int_{o}^{pR} \ell J_{o} (\ell\theta) \, d\ell = p^2 R^2 \left[\frac{2 J_1(pR\theta)}{pR\theta} \right] \tag{8}$$

Then, using Eq. (2), we see that the angular distribution is

$$\frac{d\sigma}{d\Omega} = \frac{(\eta-1)^2}{4} \; p^2 R^4 \left(\frac{2 J_1(pR\theta)}{(pR\theta)}\right)^2 \tag{9}$$

This form is the standard oscillatory Bessel function. The peaking in the forward direction can be seen clearly by putting Eq. (9) into a more convenient form. For small angles, one can approximate

$$\left(\frac{2 J_1(x)}{x}\right)^2 \approx e^{-(x/2)^2}$$

In the Appendix, it is shown that the total cross section, which is the sum of the elastic and inelastic cross sections, is just

$$\sigma_{\text{total}} = 2\pi (\eta - 1) R^2$$

Using these relations, and the small angle approximation for the four-momentum transfer we obtain

$$\frac{d\sigma}{d\Omega} = \left(\frac{p\,\sigma_{\text{total}}}{4\pi}\right)^2 e^{-\frac{R^2}{4}|t|} \tag{10a}$$

or

$$\frac{d\sigma}{d|t|} = \frac{\sigma^2_{\text{total}}}{16\pi} \; e^{-\frac{R^2}{4}|t|} \tag{10b}$$

The slope of the diffraction peak, $R^2/4$, and the dependence of this slope upon the energy of the incident particle have been the subjects of much experimental investigation.

1. Values of the Slope

The systems measured so far seem to fall into three groups as far as the values of the slope are concerned. At high energies, the slope is largest for $\bar{p}p$, intermediate for pp, π^+p, π^-p, and K^-p, and smallest for K^+p. The slopes and the equivalent radii for energies from 7 to 25 GeV[1] are:

Systems	Slope	Radius
$\bar{p}p$	$\approx 12 - 13\ (\text{GeV}/c)^{-2}$	≈ 1.35 f
pp, $\pi^{\pm}$ p, K^- p	$\approx 9 - 10\ (\text{GeV}/c)^{-2}$	≈ 1.1 f
K^+p	$\approx 6.5\ (\text{GeV}/c)^{-2}$	≈ 0.95 f

It is, of course, very interesting to see into which general group the n-p cross sections fall.

2. Energy Dependence of the Slopes

It has been observed that the slopes of some of these systems show a marked energy dependence. There have been many attempts to explain this and other behavior of two-body final states.

"The Regge pole theory was one such promising attempt several years ago. Unfortunately, the experimental behavior of the elastic scattering cross sections has demonstrated that an ever increasing and excessive number of arbitrary parameters must be introduced into the theory to explain the experimental data. Therefore, although the theory may be of formal interest, it appears to have questionable practical usefulness."[1]

Although any attempt to apply the Regge formalism to elastic scattering must include many poles and must involve many different systems at the same time,[12] the one-pole Regge fit still is a useful parameterization of the data, which clearly exhibits the energy dependence of the small angle region.

It can be shown[13] that if one Regge pole dominates, the scattering amplitude can be approximated for large s and small $|t|$ by

$$f(\theta, E) \approx \frac{\beta(t)}{\sin \pi \alpha(t)} s^{\alpha(t)}$$

The dependence of this amplitude on $|t|$ may be rather complicated. However, the amplitude exhibits a fairly simple s dependence, and it is this simple behavior which is easily compared with experimental results.

Using this expression for the scattering amplitude, the differential cross sections can be expressed as

$$\frac{d\sigma}{d\Omega} = |f(s,t)|^2$$

and

$$s = 4p^2 + 4M_n^2 \approx 4p^2 \quad \text{for large } s,$$

$$\frac{d\sigma}{d|t|} = \frac{\pi}{p^2} \frac{d\sigma}{d\Omega} = \frac{4\pi}{s^2} \left| \frac{\beta(t)\, s^{\alpha(t)}}{\sin \pi \alpha(t)} \right|^2$$

or

$$\lim_{s\to\infty} \frac{d\sigma}{d|t|} = |g(t)|^2 \, s^{2\alpha(t)-2} \tag{11}$$

The latest values of $\alpha(t) = c - d|t|$ are shown in Table I. As can be seen, the values of $\alpha(t)$ for the pp and K^+p systems indicate that for fixed $|t|$, the cross sections decrease with increasing s. The decrease, or shrinkage, is also reflected in an increase in $R^2/4$ with s. The π^-p and π^+p systems seem to remain roughly constant while the $\bar{p}p$ and K^-p systems indicate an expansion of the diffraction peak, although the K^-p data is not conclusive at present. The "shrinkage score" is thus two systems shrink, two expand, and two remain constant.

TABLE I

Values of $\alpha(|t|)$ in the Energy Range from 7 to 20 GeV.[*]

$$\alpha(|t|) = c - d|t|$$

System	c	d
p-p	(1.046 ± 0.020)	+(0.685 ± 0.051)
π^--p	(0.982 ± 0.030)	-(0.062 ± 0.068)
$\bar{p}$-p	(0.900 ± 0.084)	-(0.914 ± 0.376)
K^--p	(1.000 ± 0.140)	-(0.398 ± 0.322)
π^+-p	(0.943 ± 0.023)	+(0.103 ± 0.074)
K^+-p	(1.06 ± 0.07)	+(0.50 ± 0.16)

[*] From Reference (1).

B. Intermediate Angles

The most interesting feature of the angular distributions for $|t| > 0.7\ (\mathrm{GeV/c})^2$ is the existence of shoulders or peaks in some of the systems. This secondary peak or bump is quite prominent in the π^-p system.[14, 15] The center of the peak is at $|t| \approx 1.2\ (\mathrm{GeV/c})^2$, and the position seems to be roughly energy independent. A secondary peak is also seen in the K^-p angular distributions[16] at the same $|t|$ value. Recent data[17] indicate that the π^+p system behaves similarly to the π^-p system. The $\bar{p}p$ distributions have only weak hints of structure,[18] while there is no evidence for the bump in either pp[19] or K^+p[20] scattering.

This bump is usually explained as being simply a second diffraction maximum, but there is not universal agreement[1,2,21] on this point. Some authors feel that this may be due to enhancements in certain partial waves or due to some complicated phenomenon.

It is interesting to note that the three systems that have small or non-existent bumps proceed through pure isotopic spin channels, while two of the three systems that exhibit a second peak involve more than one isotopic spin amplitude. If any part of this peak can be explained in terms of interference between different I-spin channels, then one would hope that np scattering, which involves contributions from two isotopic spin amplitudes $(I = 0;\ 1)$, would exhibit such a peak.

C. Large Angle Scattering

1. Statistical Model

The large angle region has been the subject of a great deal of theoretical interest. Some years ago, Fast, Hagedorn, and Jones[22] proposed that large angle scattering was not due to diffraction, as in the small angle case, but rather proceeded through a mechanism that was statistical in nature. The theory was developed in analogy with the low energy nuclear physics phenomenon of compound nucleus formation. In the collision, there is a small probability, P_c, that the two particles will interact and form a compound state. In this state, the particles "forget" their initial states. The compound state then decays into one of the many final states energetically available to it. The branching ratio into a given final state can be calculated by dividing the phase space open to it by the sum of the phase space for all possible final states. Choosing the elastic channel as the final state of interest and realizing that the cross section for compound state formation is the product of P_c and the total cross section, σ_{total}, the large angle cross section can be expressed as

$$\left.\frac{d\sigma}{d\Omega}\right|_{\substack{\text{large}\\ \text{angle}}} = P_c \cdot \sigma_{\text{total}} \cdot \frac{\text{(Phase space for elastic scattering)}}{\begin{array}{c}\text{(Phase space for all energetically}\\ \text{possible final states)}\end{array}} \qquad (12)$$

where the last term is dependent upon the total center-of-mass energy, E. Fast, Hagedorn and Jones computed the branching ratios of πp and pp elastic scattering as a function of energy using digital computers. They found that the behavior of the cross sections with energy could be fit quite well with an exponential of the form:

$$\left.\frac{d\sigma}{d\Omega}\right|_{\substack{\text{large}\\ \text{angle}}} \propto \exp^{-KE} \qquad (13)$$

This energy dependence can also be "derived" using a simple thermodynamic model put forth by Cocconi.[23] In this model, phase space factors are ignored. The compound system decays with equal probability into N final states, only one of which is the elastic channel. Therefore, the elastic cross section is

$$\left.\frac{d\sigma}{d\Omega}\right|_{\substack{\text{large}\\ \text{angles}}} \propto P_c\,\sigma_{\text{total}} \cdot \frac{1}{N} \tag{14}$$

Thermodynamic arguments now yield T, the "temperature" of the compound system. The Boltzmann definition of the entropy S of a system is

$$S = k \log N \tag{15}$$

where k is Boltzmann's constant and N is the number of independent orientations of the system. N is interpreted to be the number of channels into which the system can decay in this application. One also has the following relation when the compound system is held at constant volume:

$$dE = T\,dS \tag{16}$$

Now, if S is proportional to a power of the energy

$$S = a\,E^n \tag{17}$$

then combining Eqs. (14), (15) and (17) yields

$$\frac{d\sigma}{d\Omega} \propto \exp\left(-KE^n\right) \tag{18}$$

where $K = a/k$. It also follows from Eq. (16) that

$$T = \frac{1}{n\,a\,E^{n-1}} \tag{19}$$

In all systems measured so far, the measurements are not accurate enough to determine the value of n in the range 1/2 to 1. The calculations of Fast, Hagedorn and Jones yield n = 1. However, independent of the choice of N, the "temperature" is a well defined quantity:

$$B = \frac{\frac{d\sigma}{d\Omega}(E_1)}{\frac{d\sigma}{d\Omega}(E_2)} = \exp\left(K\left(E_2^n - E_1^n\right)\right) = \exp\left(KnE_{\text{average}}^{n-1}\,\Delta E\right)$$

$$T = \Delta E/k \log B \tag{20}$$

Using these relations and the Fast, Hagedorn and Jones calculations, the values of K and T for proton scattering are:

$$K = 3.30 \text{ GeV}^{-1} \tag{21a}$$

$$T = 2.18\, m_\pi = 0.30 \text{ GeV} \tag{21b}$$

The statistical model makes no specific predictions regarding angular distributions except the following general statements. If the decay to a final state is made from a compound formation that has truly "forgotten" its origin, the angular distributions of the decay products must be isotropic as there then exists no preferred direction. If there are no interference terms between partial waves of different angular momenta in the decay process, then symmetry around 90° in the center-of-mass system is expected.[23, 24] However, if there is any appreciable interference, "the angular distribution need not be symmetric about 90°".[24]

2. "Rigid" Proton Model

Orear[25] has made the remarkable observation that it is possible to fit proton-proton differential cross sections over a very large range of energies and angles with a surprisingly simple expression of the form:

$$\frac{d\sigma}{d\Omega} = \frac{A}{s} e^{-P_\perp/0.15} \tag{22}$$

where $P_\perp = p \sin\theta$ and is the transverse momentum imparted to the target nucleon.

Wu and Yang[26] make some interesting predictions based on Eq. (22). They speculate that the exponential fall-off with increasing $P_\perp$ is a manifestation of the difficulty of transferring large amounts of transverse momentum in elastic scattering. In addition, they postulate that such a difficulty exists in <u>all</u> high energy nuclear collisions, because this difficulty must be an inherent characteristic of the nucleon. In an attempt to explain this postulate in terms of a model, they picture the nucleon as an extended object held together with an internal rigidity of a few hundred MeV. The fall-off with increasing $P_\perp$ is attributed to the difficulty of accelerating this extended object without "breaking it up" and producing an inelastic final state.

The fact that large longitudinal momentum transfers do not cause such a rapid decrease in the cross sections can also be accounted for in this model. In the collision, the two nucleons can be interpreted as exchanging pieces of each other. These exchanges yield large longitudinal momentum transfers.

It is further assumed that in a large angle collision there are many final states available to the nucleons and that there is no strong energy dependence in the choice of the final state. This assumption and their interpretation of the Orear fit lead to the statement that any nucleon-nucleon two-body interaction obeys Eq. (22) with suitable changes in A as long as the final state satisfies all of the necessary conservation laws. In the limit of very high energies, cross sections for different reactions that involve the same $P_\perp$ should appear quite similar. In particular it is predicted that

$$\lim_{s \to \infty} \frac{\ln \left.\frac{d\sigma}{d\Omega}\right|_{\substack{\text{large}\\ \text{angles}}} (\theta,\ np \to np)}{\ln \left.\frac{d\sigma}{d\Omega}\right|_{\substack{\text{large}\\ \text{angles}}} (\theta,\ pp \to pp)} \to 1 \tag{23}$$

$$\lim_{s \to \infty} \frac{\ln \left.\frac{d\sigma}{d\Omega}\right|_{\substack{\text{large}\\ \text{angles}}} (\theta,\ np \to np)}{\ln \left.\frac{d\sigma}{d\Omega}\right|_{\substack{\text{large}\\ \text{angles}}} (\pi-\theta,\ np \to np)} \to 1 \tag{24}$$

3. "Random Phase" Isotopic Spin Model

Wu and Yang[26] make another prediction about large angle scattering. It is assumed that the elastic differential cross sections in different isotopic spin channels have, on the average, the same absolute amplitudes and random relative phases. Thus, if a_I is the matrix element for a scattering process with total isotopic spin I, then on the average:

$$a_I \, a_{I'} = \delta_{II'} \, a_I^2 \tag{25}$$

It is convenient to express the wave functions for the pp and np systems in terms of the isotopic spin wave functions, $\phi_I^{I_3}$, where the superscript is the third component of the total isotopic spin and the subscript is the total isotopic spin. Thus,

$$\Psi\,(\mathrm{pp}) = \phi_1^1$$

$$\Psi\,(\mathrm{np}) = \frac{1}{\sqrt{2}}\,(\phi_1^o - \phi_o^o)$$

The cross sections are then expressed in terms of the strong interaction operator M as

$$\left.\frac{d\sigma}{d\Omega}\right)_{pp} = \left|\langle \Psi(\mathrm{pp})\ |M|\ \ \Psi(\mathrm{pp})\rangle\right|^2 = \left|\langle\phi_1^1\ |M|\ \phi_1^1\rangle\right|^2 = \left|a_1\right|^2 \qquad (26a)$$

$$\left.\frac{d\sigma}{d\Omega}\right)_{np} = \left|\langle \Psi(\mathrm{np})\ |M|\ \Psi(\mathrm{np})\rangle\right|^2 = \left|\langle\frac{1}{\sqrt{2}}\ (\phi_1^o - \phi_o^o)\ |M|\ \frac{1}{\sqrt{2}}\ (\phi_1^o - \phi_o^o)\rangle\right|^2$$

$$= \frac{1}{4}\left|\langle\phi_1^o\ |M|\ \phi_1^o\rangle + \langle\phi_o^o\ |M|\ \phi_o^o\rangle - \langle\phi_1^o\ |M|\ \phi_o^o\rangle - \langle\phi_o^o\ |M|\ \phi_1^o\rangle\right|^2$$

$$= \frac{1}{4}\left|a_1 + a_o\right|^2 \qquad (26b)$$

where the fact that the strong interactions conserve I has been used. Using Eq. (25) and the assumption that the absolute applitudes for different I are the same, it is clear that

$$\left.\frac{d\sigma}{d\Omega}\right)_{pp} = |a|^2$$

$$\left.\frac{d\sigma}{d\Omega}\right)_{np} = \frac{1}{2}|a|^2 \tag{27}$$

or

$$\left.\frac{d\sigma}{d\Omega}\right)_{pp} = 2\left.\frac{d\sigma}{d\Omega}\right)_{np} \tag{28}$$

4. Test of Charge Independence

Comparison of np and pp differential cross sections at 90° provides a check of the charge independence of nuclear forces.[27] At 90° in the center-of-mass system, only <u>even</u> angular momentum waves contribute to the scattering amplitude because $P_\ell(\cos\theta) = 0$ at $\theta = \pi/2$ for ℓ odd. This implies that the space wave function is symmetric. Proton-proton scattering always takes place with total isotopic spin, I, equal to 1. Therefore, in order to have a totally antisymmetric wave function, the scattering must take place in the singlet spin state, that is, with S, the total spin, equal to 0. We can thus write

$$\left.\frac{d\sigma^{pp}}{d\Omega}\right|_{90^{\circ}} = \left|\sum_{\ell\,\text{even}} A_\ell^{pp}(I = 1, S = 0)\right|^2$$

where $A_\ell(I,S)$ is the scattering amplitude for the ℓ^{th} partial wave with total isotopic spin I and total spin S.

The neutron-proton scattering can proceed with either I = 1 and S = 0 or I = 0 and S = 1. After summing over final spin states and averaging over initial spin states, the differential cross section can be written as

$$\left.\frac{d\sigma}{d\Omega}^{np}\right|_{90^{o}} = \frac{1}{4}\left|\sum_{\ell\,\mathrm{even}} A_{\ell}^{np}(I = 1,\ S = 0)\right|^{2} + \frac{3}{4}\left|\sum_{\ell\,\mathrm{even}} A_{\ell}^{np}(I = 0,\ S = 1)\right|^{2}$$

Charge independence involves the statement that the non-Coulomb forces between the nucleons depend only on I, S and ℓ and not on the charge states of the nucleons; that is,

$$A_{\ell}^{np}(I,\ S) = A_{\ell}^{pp}(I,\ S)$$

Putting this into the expressions for the 90° differential cross sections, it can be seen that charge independence of nuclear forces requires

$$\left(\frac{d\sigma}{d\Omega}^{np}\right)_{90^{o}} \geq \frac{1}{4}\left(\frac{d\sigma}{d\Omega}^{pp}\right)_{90^{o}} \tag{29}$$

D. Backward Angles

The only previous experimental investigations of the neutron-proton elastic scattering system at high energies concerned the study of a very small angular region near 180° in the center-of-mass system. Near 180°, the recoil proton comes forward with most of the energy of the incident neutron. Because an uncharged neutron appears to have changed into a proton, this reaction became known as "charge exchange scattering," even though it is just a small angular region of n-p elastic scattering. Palevsky *et al.*[28] and Friedes *et al.*[29] measured the charge exchange cross section at 2.04, 2.2, and 2.85 GeV at the Cosmotron, and Manning et al.[30] measured it at 6.6 GeV at Nimrod.

Basically, the method of measuring the cross sections was as follows. As sketched in Fig. 2, the internal proton beam hit a production target which was beryllium in one case and lithium deuteride in the other. The particles emerging from the target were collimated after charged particles were removed with sweeping magnets. The remaining neutrons then interacted in a liquid hydrogen target and the angle and momentum of the outgoing proton was measured. Note that the neutrons were produced by a charge exchange scattering, $\sigma_{\text{charge exchange}}$ (p, n) and then underwent another charge exchange scattering, $\sigma_{\text{c.e.}}$ (n, p). Since $\sigma_{\text{c.e.}}(p, n) = \sigma_{\text{c.e.}}(n, p)$, a comparison of the flux of protons emerging from the hydrogen target with the flux of protons entering the production target yields a value proportional to the square of the charge exchange cross section. Because of inelastic contamination, this method is limited to angles very close to 180° in the center-of-mass system. Friedes et al.[29] were able to get measurements out to approximately 140° at 2.2 GeV.

In this charge exchange region the cross section has the general characteristic of a very large, sharply peaked backward distribution (see Fig. 3). This peak is usually fit with the sum of two exponentials in $|t|$. In the region closest to 180°, the slope of the exponential is between 40 and 50 $(\text{GeV}/c)^{-2}$, while as one goes toward 90°, the slope changes to approximately 4 $(\text{GeV}/c)^{-2}$. The steep slope implies that the radius of interaction, R, is greater than 2 fermis, which is larger than any measurement on the proton-proton system, while the smaller value implies $R < 1$ fermi, smaller than the pp values. The width and

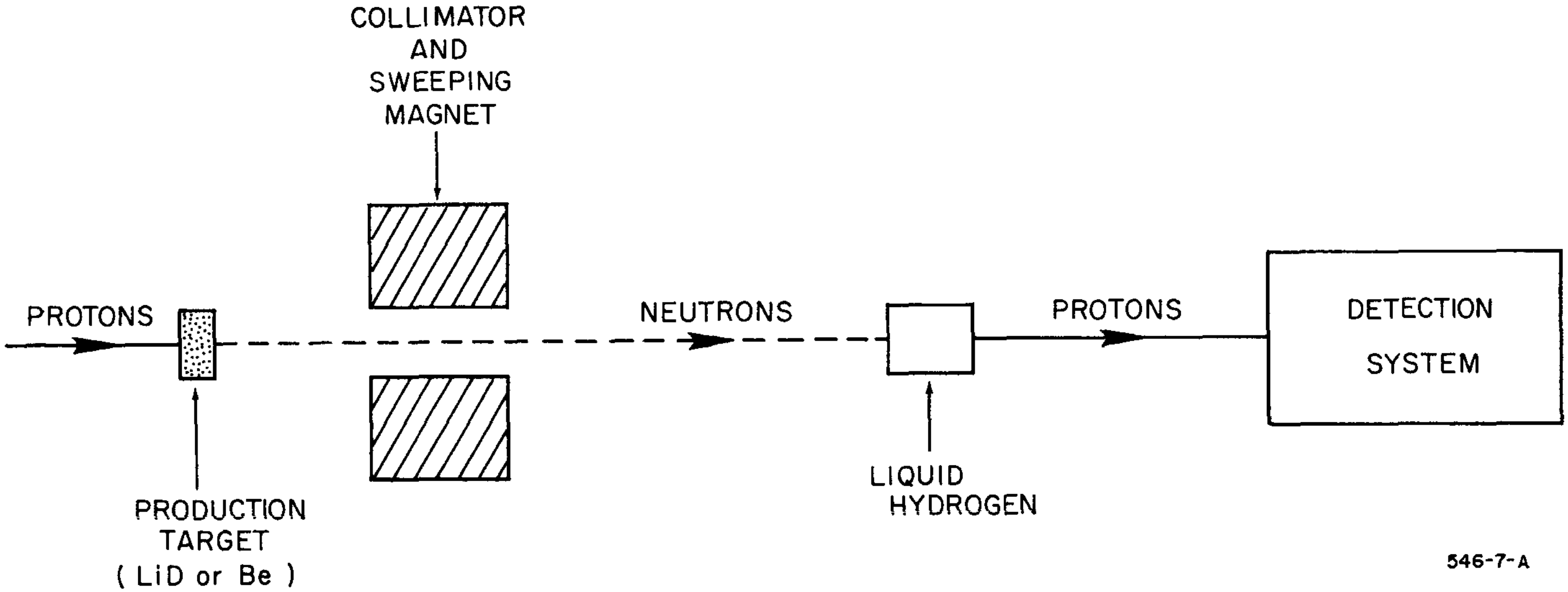

FIG. 2--Sketch of beam layout for charge exchange measurements.

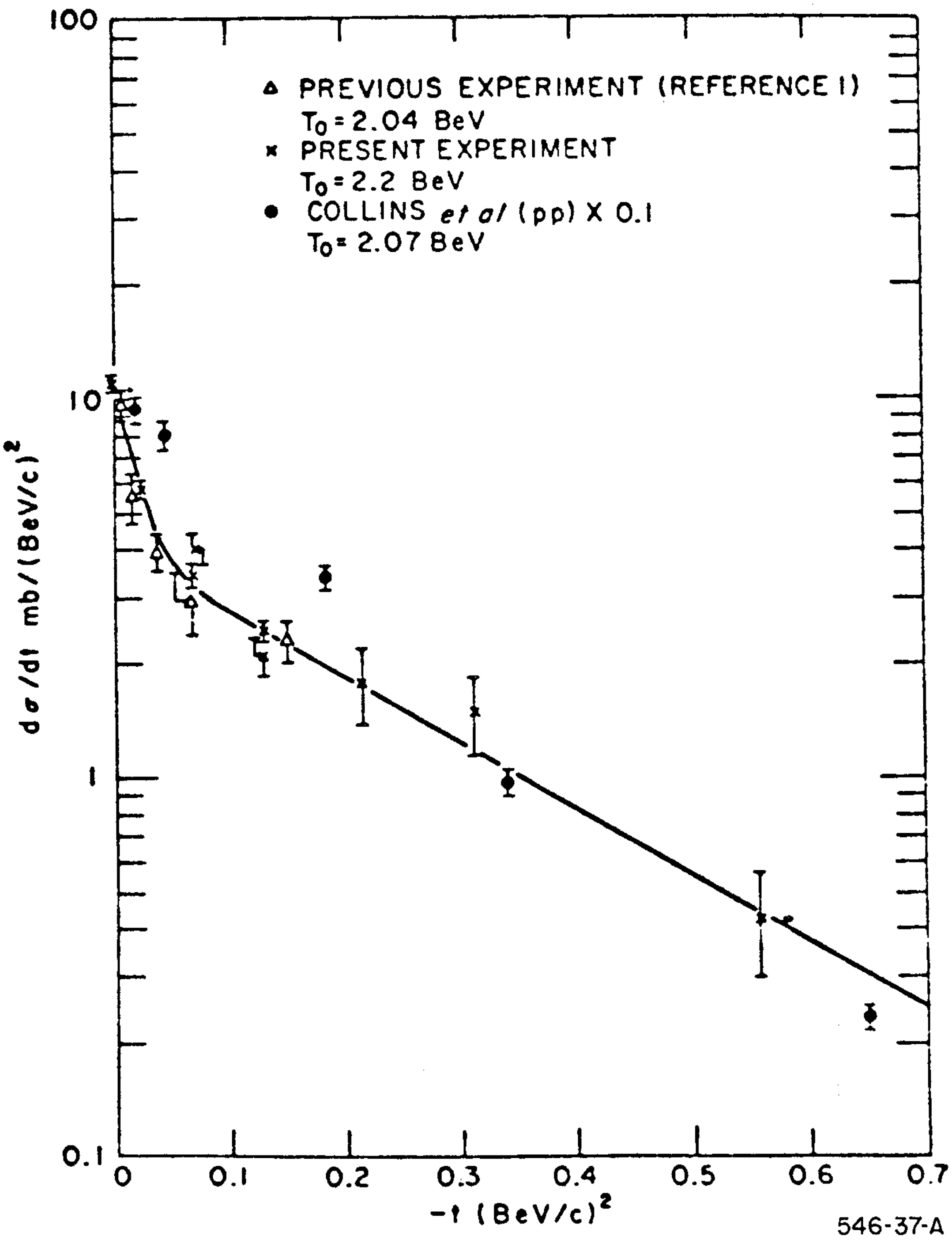

FIG. 3--Neutron-proton charge exchange cross sections at 2.04 and 2.2 GeV (from J. L. Friedes, H. Palevsky, R. L. Stearns and R. J. Sutter, Ref. 29). In this figure, t is defined as $(|t|_{max} - |t|)$, where $|t|_{max}$ is 3.828 $(GeV/c)^2$ for 2.04 GeV and 4.128 $(GeV/c)^2$ for 2.2 GeV.

slope of these peaks appear to be energy independent. Attempts[29, 31] to explain these peaks have given rather poor fits to the data.

It is important to note that these measurements of the "charge exchange" region constitute the only experimental investigations of the neutron-proton elastic scattering system at energies above 1 GeV prior to the present experiment.

E. Other Models

Serber[32, 33] uses a purely absorbing Yukawa potential in an optical model. The distributions predicted are

$$\frac{d\sigma}{d|t|} \propto \frac{1}{|t|^6} \tag{30}$$

This model does not seem to fit the data at intermediate or large angles very well.[11]

Krisch[34] has shown that it is possible to fit all the proton-proton cross sections with the sum of three exponentials in $p_{\perp}^2$, and has interpreted this as diffraction scattering from three different regions of the nucleon.

Kastrup[35] says that when two nucleons undergo large angle collisions, the long-range parts of the fields of the two particles have to readjust themselves considerably. This readjustment can be pictured as being accompanied by the emission of "soft" mesons. The energies of the mesons are small with respect to the nucleon energies; recoil effects are neglected. The emissions are statistically independent and can be described by Poisson's distribution. Elastic scattering is interpreted as the case in which the number of mesons emitted is zero. An exponential form results, and the terms in the exponential are equated with Orear's empirical fit, Eq. (22).

There are other theories extant, but none serve to clear up the problem of strong interaction elastic scattering. It is hoped that some help may be obtained from the measurement of the neutron-proton system to be described in the following sections.

IV. THE NEUTRON BEAM

The neutron beam for this experiment was produced by focusing a proton beam onto a beryllium target, sweeping away the charged particles, and then collimating the neutrons into a well-defined beam with a very broad energy spectrum. The details of the beam are discussed below.

The experiment was performed using the external proton beam of the Bevatron at the Lawrence Radiation Laboratory. The external beam was ejected from the main ring during a 300-msec flattop pulse and yielded a spill of 6.3-GeV protons every six-second cycle. During the course of the experiment, the intensity in the external beam was varied from 1 to 7 $\times 10^{10}$ protons per pulse.

As shown in Fig. 4, the proton beam was focused onto a beryllium target 3/8 inch by 1/4 inch in cross section and 8 inches (about 2 collision lengths) long. The position of the proton beam on the beryllium target was monitored with two independent systems. A closed-circuit television camera, looking at a thin piece of plastic scintillator placed directly upstream of the Be target, gave a visual indication of the location of the beam spot. Special monitor counters were also used. As shown in Fig. 5,these counters were 1/16 inch scintillators framing the upstream end of the Be target. They were mounted on 53 AVP photomultipliers with bases designed for low gain. By observing the output of these two tubes on an oscilloscope it was possible to detect drifts of the position of the proton beam of the order of 1/16 inch to 1/8 inch. The Be target itself was mounted on a hinge attached to the first bending magnet. The hinge allowed easy removal and accurate replacement of the target whenever a check of the alignment of the beam was necessary.

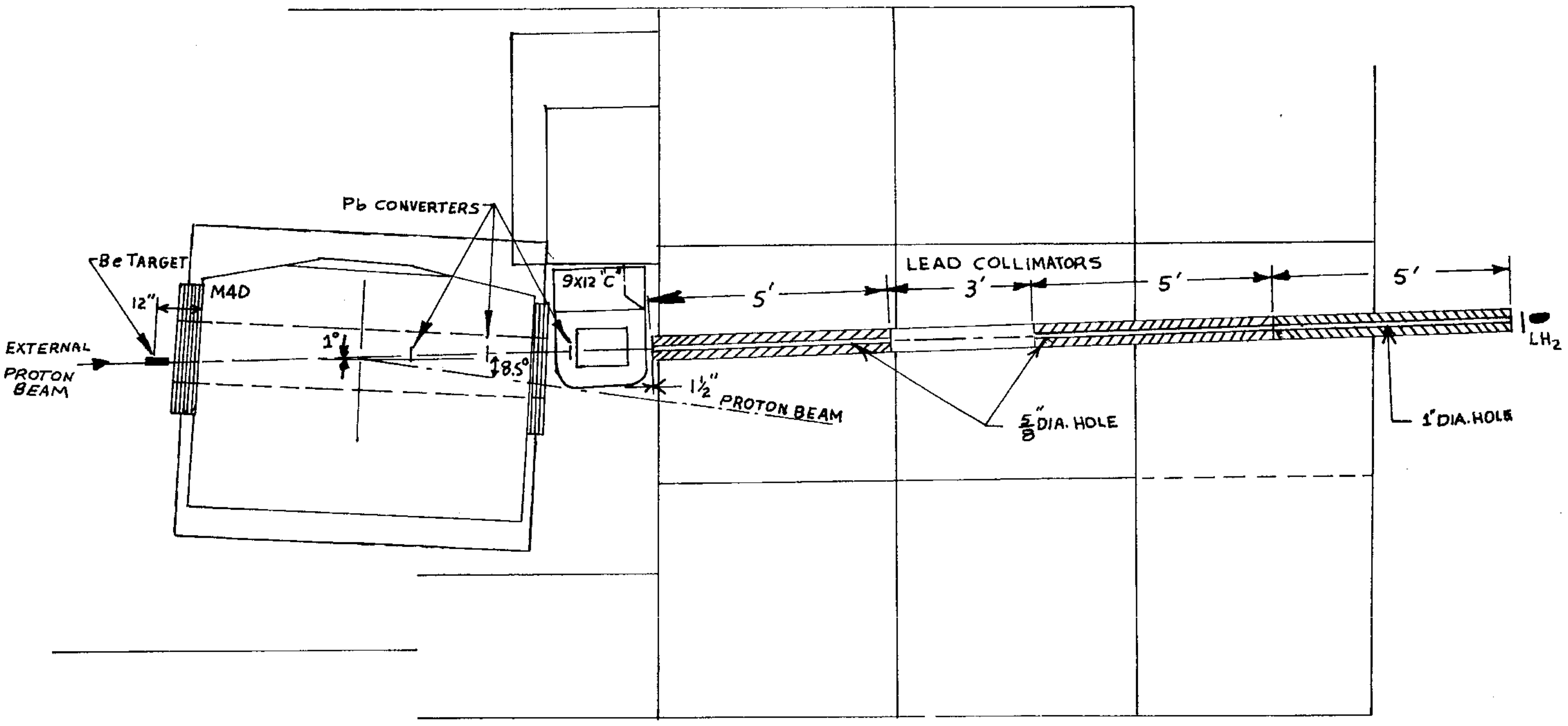

FIG. 4--Neutron beam layout.

546-39-A

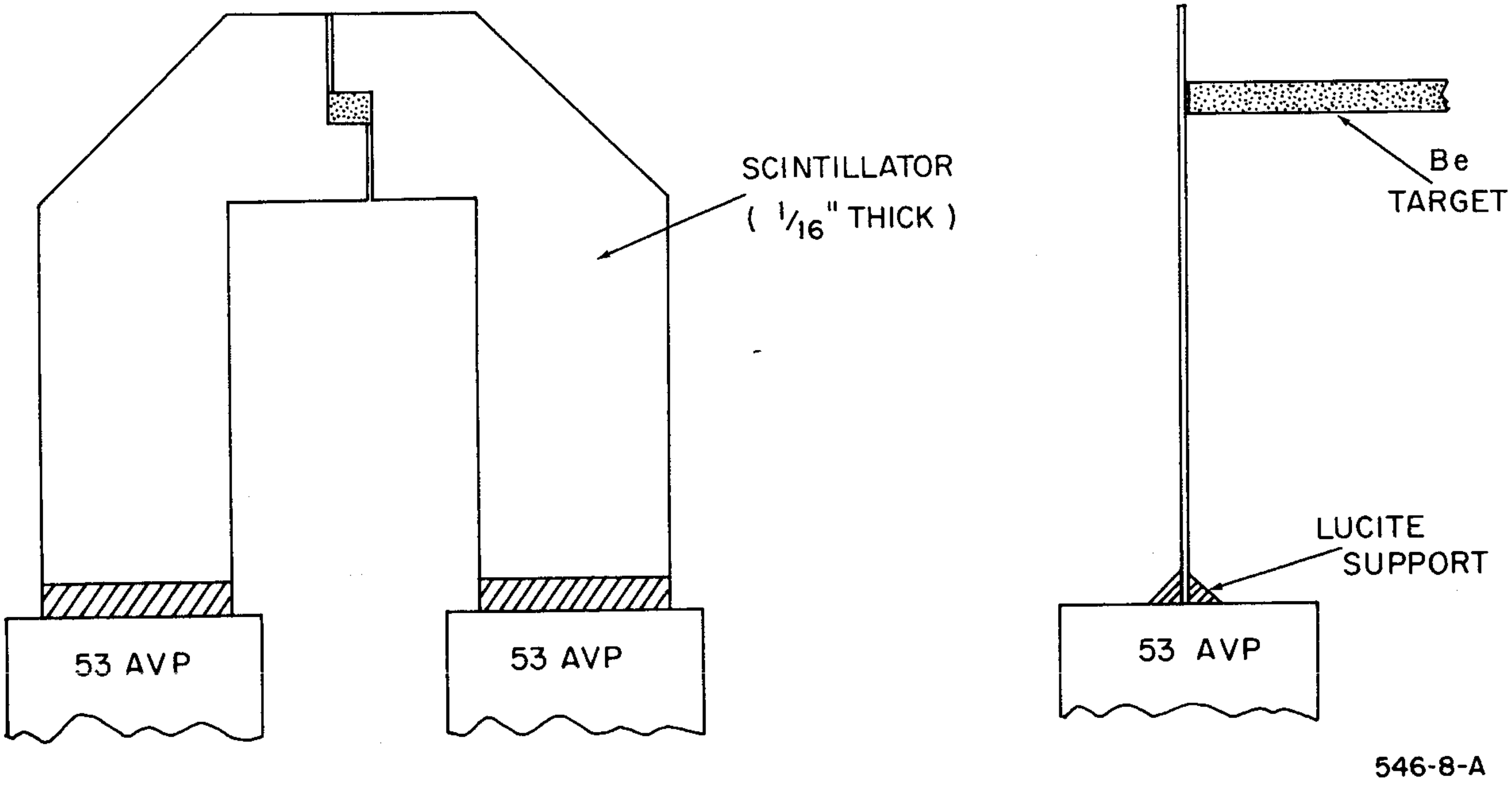

FIG. 5--Beam position monitors. The scintillators framed the upstream end of the beryllium target.

Immediately following the Be target, a large sweeping magnet, M4D, removed charged particles from the beam. M4D, an 84-inch-long, 15-inch-wide, 4-inch-high bending magnet[36] was run at a nominal current of 1000 amps (B = 14 kG) to bend the unscattered proton beam through 8.5°. Because M4D served no analyzing function, its alignment was not critical.

The photon contamination in the neutron beam was reduced with three pieces of 1/4 inch lead (a total of 3.8 radiation lengths) followed by a small 9-inch × 12-inch "C" bending magnet to sweep out the electron pairs. The lead converter was divided into three sections to increase the efficiency of the system in removing gammas.

At 15 feet from the center of the Be target, the neutrons entered the first of three lead collimators. The detail of these collimators is shown in Fig. 6. Two 5-foot-long pieces of 12-inch × 3-inch steel channel were welded to form a rectangular tube. A steel pipe was supported in the center of the tube by bars on each end and the entire tube, except for the inside of the pipe, was filled with 1575 pounds of lead. The first two of these units had pipes of 5/8-inch i.d. while the third had a pipe with a 1-inch i.d.

The central ray of the neutrons entering the collimators made an angle of 1° with respect to the original proton beam. This angle was selected because a preliminary survey experiment showed that the neutron flux is greatest at small production angles. Safety precautions prohibited angles smaller than 1°. As shown in Fig. 4,the proton beam was swept to the opposite side of the 0° line so that at the entrance of the collimator, the neutron beam and the charged particles were separated by 1.1 feet. The solid angle subtended by the collimator system was determined by the downstream end of the second collimator and was 3.87×10^{-6} steradians. As the beam was defined by the first two

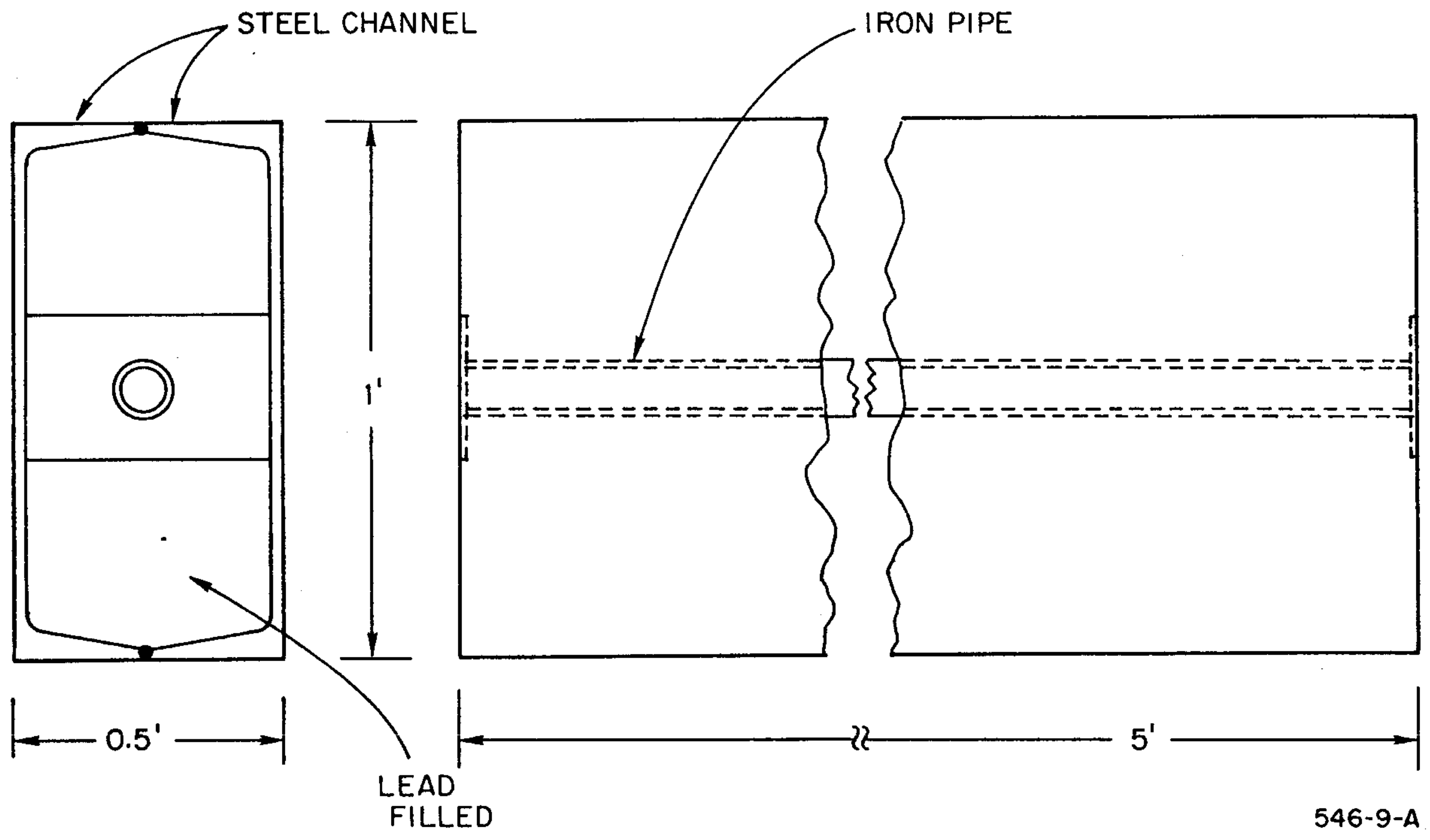

FIG. 6--Detail of neutron beam collimators.

collimators, the larger diameter of the third unit of the collimator system reduced the number of neutrons in the beam that had scattered against the sides of the collimators.

The shielding wall in which the collimators were imbedded was designed to minimize neutron backgrounds in the main experimental area. The wall consisted of 5 feet of steel followed by 10 feet of heavy concrete. All crevices between the blocks of steel and concrete were filled with lead bricks and lead shot.

When the neutron beam left the collimator, it was roughly an inch in diameter with negligible spatial tails and an angular divergence of less than 0.15 degrees. The energy spectrum of the neutrons was determined from the analysis of elastic scattering events and will be discussed later.

V. THE MAIN EXPERIMENTAL AREA

After leaving the collimator system, the neutron beam entered a liquid hydrogen target. Following an interaction in the hydrogen, the angle and momentum of the recoil proton and the angle of the scattered neutron were measured. The details of the detection method are described below.

A. The Hydrogen Target

Three main considerations determined the design of the target: (1) A minimum amount of material other than hydrogen should be present in the path of the beam. (2) There should be no unnecessary material for the scattered particles to pass through for 90° on either side of the beam line. (3) All material other than hydrogen in the beam's path should be far enough from the hydrogen region to permit a clean separation of interactions in the material from interactions in the hydrogen. As can be seen on the assembly drawing in Fig. 7, the fill lines and vent lines to the Mylar flask that contained the hydrogen were arranged so that they did not obstruct the beam. In addition, the vacuum jacket leading back to the reservoir was set at an angle so that there was a clear view of the flask for 90° on either side of the beam line.

The neutron beam entered the vacuum jacket surrounding the flask through a 0.020-inch-thick Mylar entrance window. The hydrogen was contained in a 10-inch-long Mylar cylinder with domes on either end, yielding a flask 12 inches long and 2-1/2 inches in diameter with 0.0005-inch-thick walls. The flask was wrapped with 10 layers of aluminized Mylar (0.00025 inch thick) and aluminum foil (0.00025 inch thick) to reduce heat transfer by radiation. The aluminum vacuum jacket was a 15-1/4-inch-long domed cylinder, 8 inches in diameter, with 0.040-inch-thick walls. The flask was centered in the vacuum jacket,

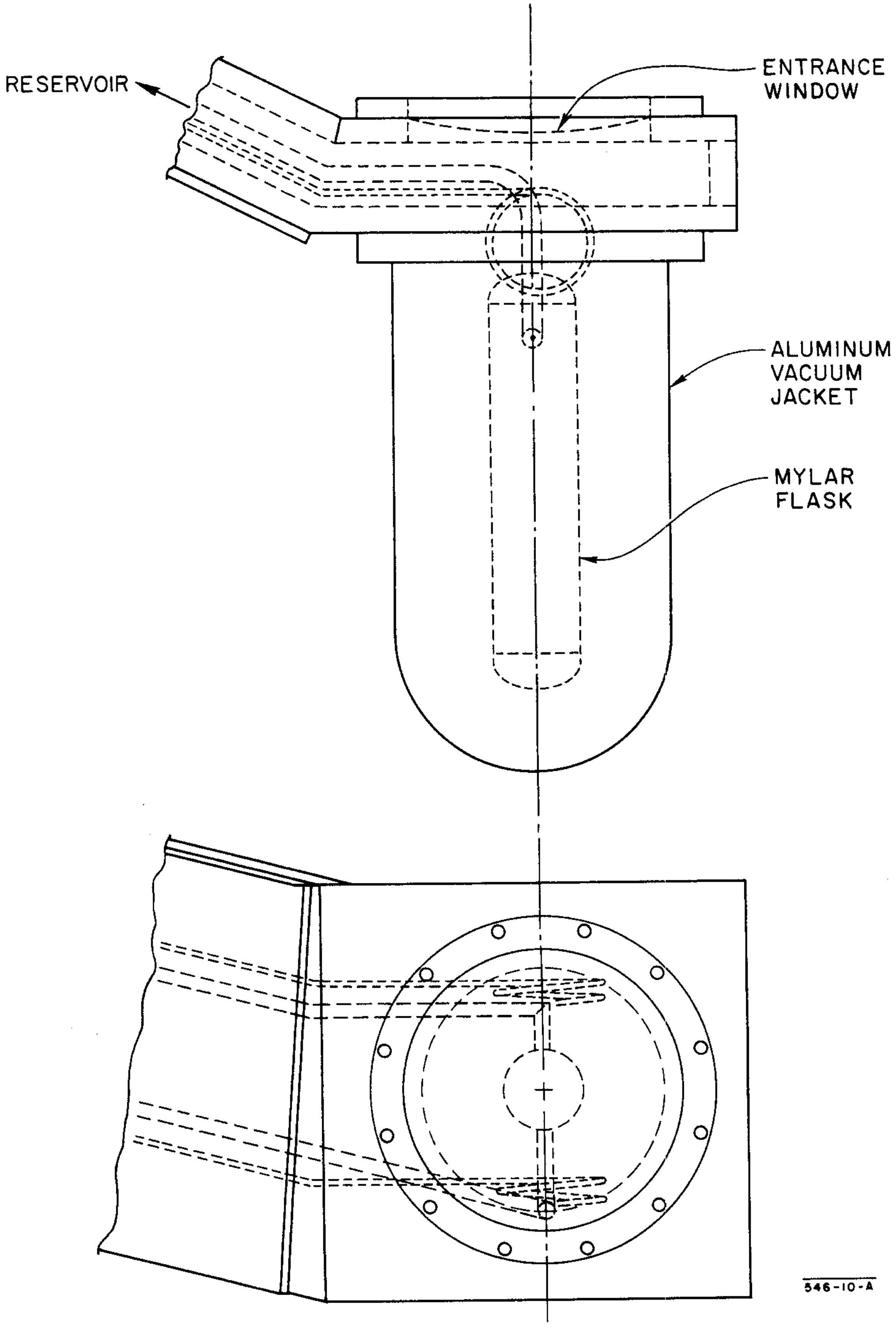

FIG. 7--Assembly drawing of liquid hydrogen target.

thereby allowing at least 2-1/2 inches between the flask and the vacuum jacket or the entrance window. The reservoir, Jake IIB,[37] permitted the use of either liquid hydrogen or deuterium.

The reservoir and the attached target could be positioned by means of adjustment bolts on the reservoir stand. In addition to their positioning function, these bolts could be used to move the target if it became necessary to check the upstream alignment.

B. The Proton Spectrometer

The momentum and angle of the recoil proton were measured with two pairs of thin-plate spark chambers before and after a bending magnet. The plan view of the spectrometer is shown in Fig. 8.

The spark chambers each had four 3/8-inch gaps with 1-mil aluminum foil plates. The chambers were constructed by stretching the foil onto lucite frames and gluing the frames together with Silastic RTV 891.[38] In order to equalize the pressure on the outside plates of the chamber when it was filled with gas, the hinged Mylar window shown in Fig. 9a was attached to the chamber. This system allowed pressure equalization by permitting expansion of the Mylar window without distortion of the frame holding the outermost plate. The active area of the two chambers on the target side of the magnet was 22 inches long and 6 inches high. The chambers on the other side of the magnet were 39 inches long and 11 inches high. The chambers were operated with a 90% Ne – 10% He gas mixture. A photograph of two of the chambers is shown in Fig. 9b.

The analyzing magnet, ATLAS,[39] was 29 inches wide and 36 inches long with an 8-inch gap. Very extensive measurements of the magnetic field were made by the LRL Magnet Test Group.[40, 41] Using Rawson probes and a computer driven system, the field was measured in a one-inch grid pattern

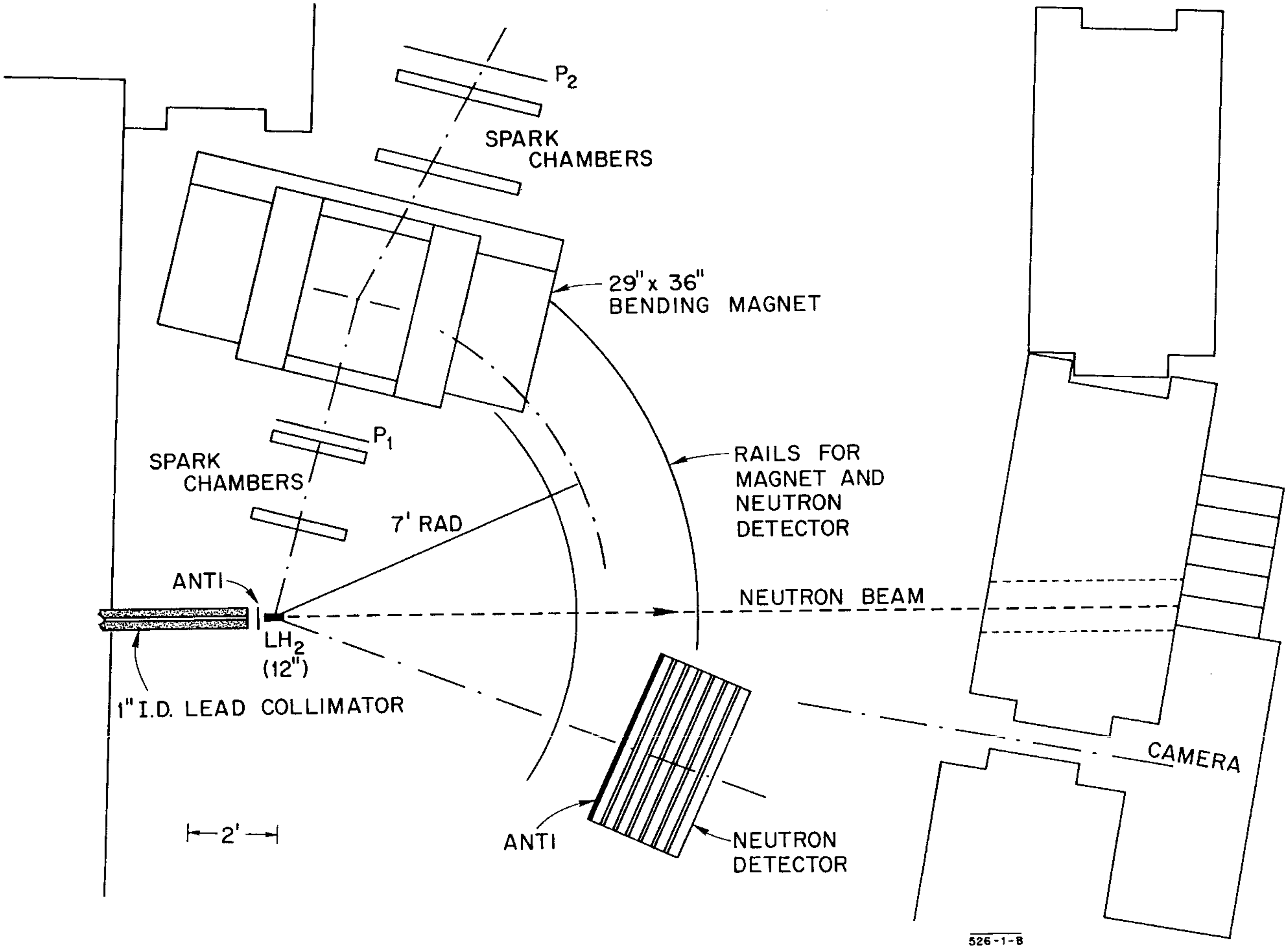

FIG. 8--Plan view of main experimental area showing liquid hydrogen target, proton spectrometer, and neutron detector.

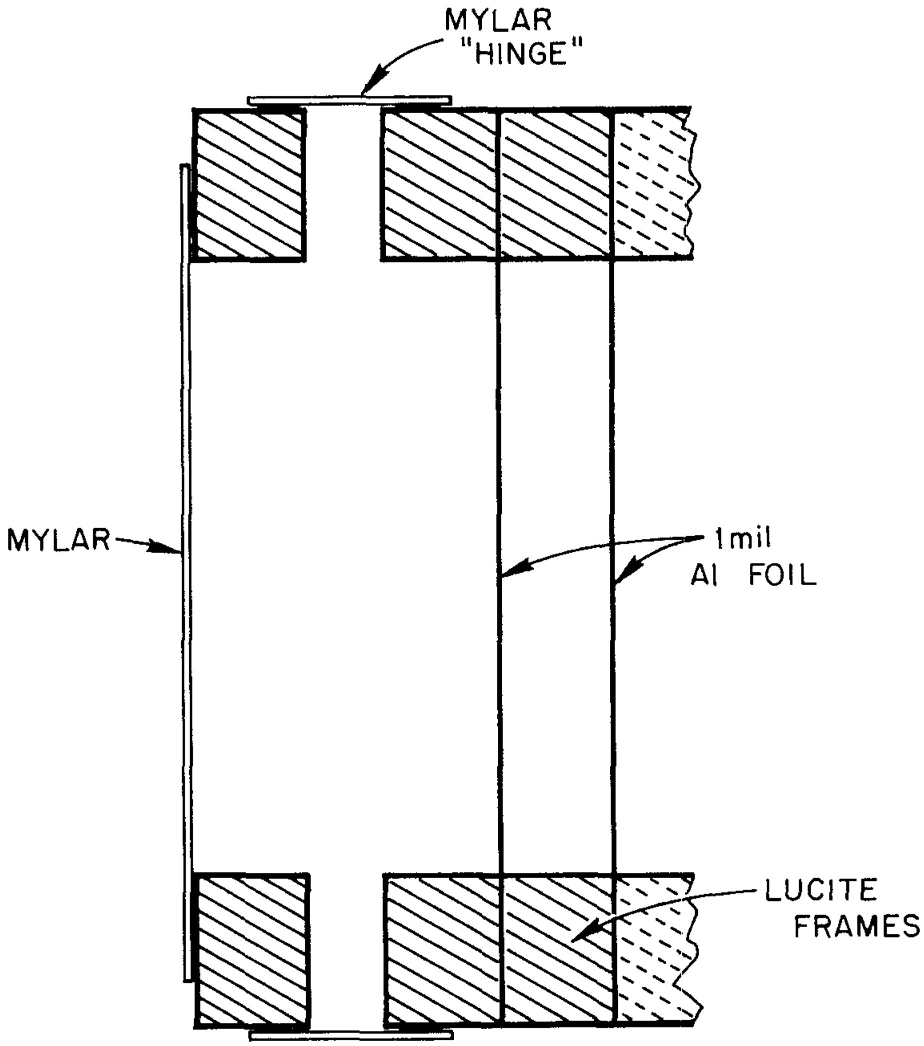

546-11-A

FIG. 9(a)--Hinged Mylar window to allow expansion of proton spark chamber.

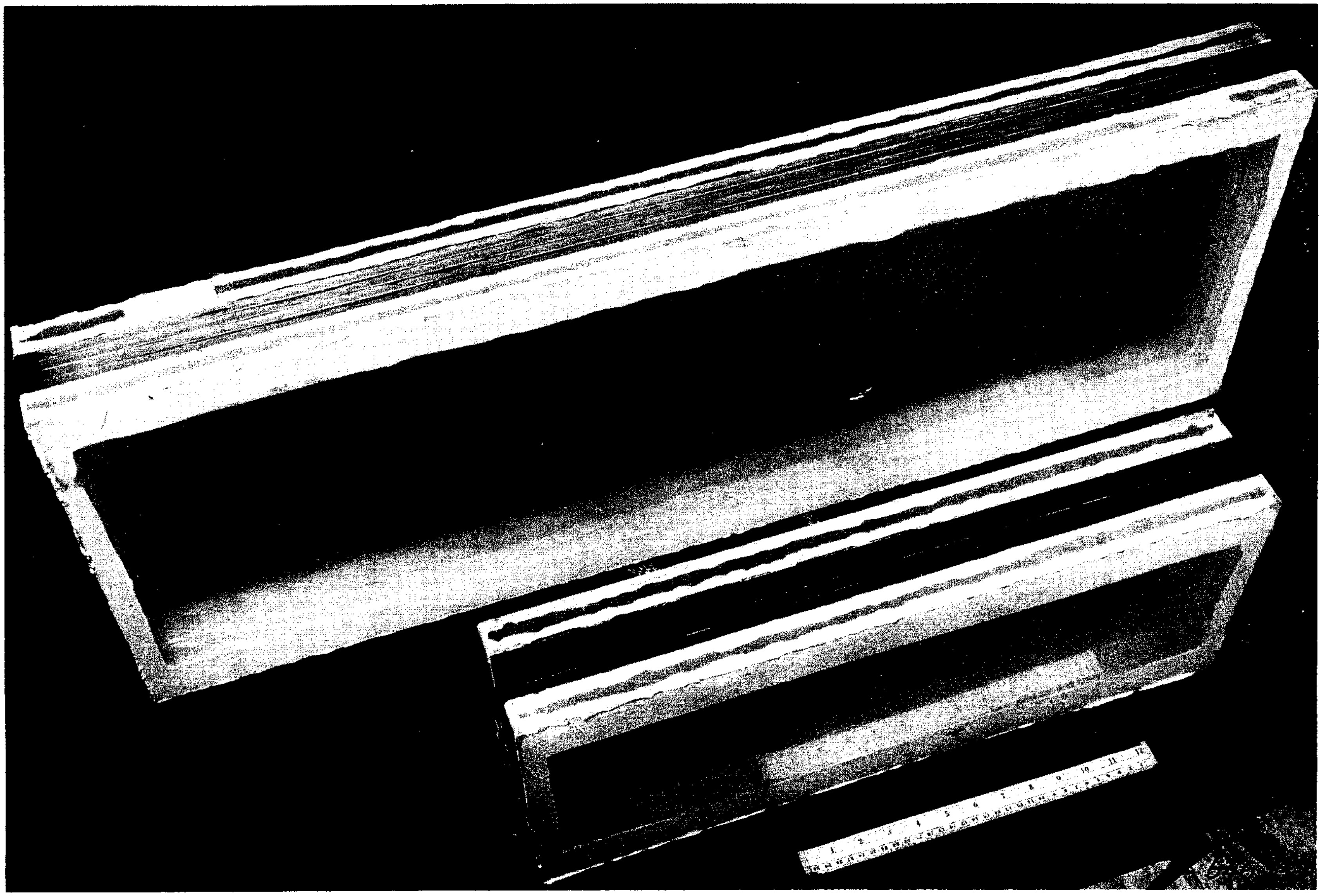

FIG. 9(b)--Photograph of two of the proton spark chambers.

(2800 points per grid) at seven elevations (0 inch, ± 2.0 inches, ± 2.8 inches, and ± 3.0 inches from the median plane) and at six current levels (I = 392, 588, 855, 960, 1084, and 1203 amperes). This data was placed on magnetic tape and used in determining the proton momentum from the position of the tracks in the spark chambers.

The magnet-spark chamber system was supported on a carriage that rode on curved railroad tracks. The tracks, centered on the liquid hydrogen target and made from American Society of Civil Engineers Standard 70-pound rail, had radii of approximately 6 feet, 4 inches and 9 feet, 7 inches. The center of the magnet system rode seven feet from the center of the target. The support system contained provisions for rotating the magnet and adjusting its height in order to align the magnet system after its position on the rails had been changed. At each setting of the system, there was roughly a 12° acceptance interval for recoil protons. For low-momentum protons, the precision of measurement of the proton angle was limited primarily by multiple-Coulomb scattering in the hydrogen and in the vacuum jacket. The momentum measurements were also limited by multiple-Coulomb scattering to a few percent.

C. The Neutron Detector

The scattered neutron was observed by requiring that a neutral particle interact and produce at least one charged particle in an array of seven steel plate spark chambers. The location of the point of interaction and the position of the liquid hydrogen target yielded the angle of the scattered neutron.

The neutron detector chambers had four 3/8-inch gaps with plates made from 3/16-inch-thick, cold rolled stainless steel, type 304 polished to a near mirror finish (320 grit polish). The chambers were constructed by sandwiching frames of lucite between the plates. The active area of each chamber was 12 inches high and 48 inches long. A typical chamber is shown in Fig. 10a.

The array of seven chambers represented a total of 1.4 collision lengths; therefore, roughly sixty percent of the neutrons that entered the detector interacted to produce charged particles. As can be seen from the event drawn in Fig. 10b, measurement of the charged particles gave the vertex of the interaction; when this was correlated with the intersection of the neutron beam and the path of the recoil proton projected into the liquid hydrogen target, the angle of the scattered neutron was known. The accuracy of measurement of this angle was, for the most part, limited by the width of the beam in the hydrogen and there was a typical uncertainty of ± 8-10 mrad.

This spark chamber array also ran on the railroad tracks on a carriage 9 feet from the target. As with the magnet system, there were provisions for rotating and leveling the array to insure alignment. At each setting of the apparatus, there was a 30° acceptance interval for scattered neutrons.

During the course of the experiment, the two carriages were placed in seven different settings to cover all scattering angles. When the "charge exchange" region was reached, the scattered neutron did not have sufficient kinetic energy to produce charged particles that would trigger the detector (170 MeV was the cut-off). Large scintillation counters were then substituted for the neutron detection chambers and a complete "charge exchange" measurement was performed, but this will not be discussed in this paper.

D. Scintillation Counters

There were nine scintillation counters involved in the triggering system, two in the proton arm and seven in the neutron arm.

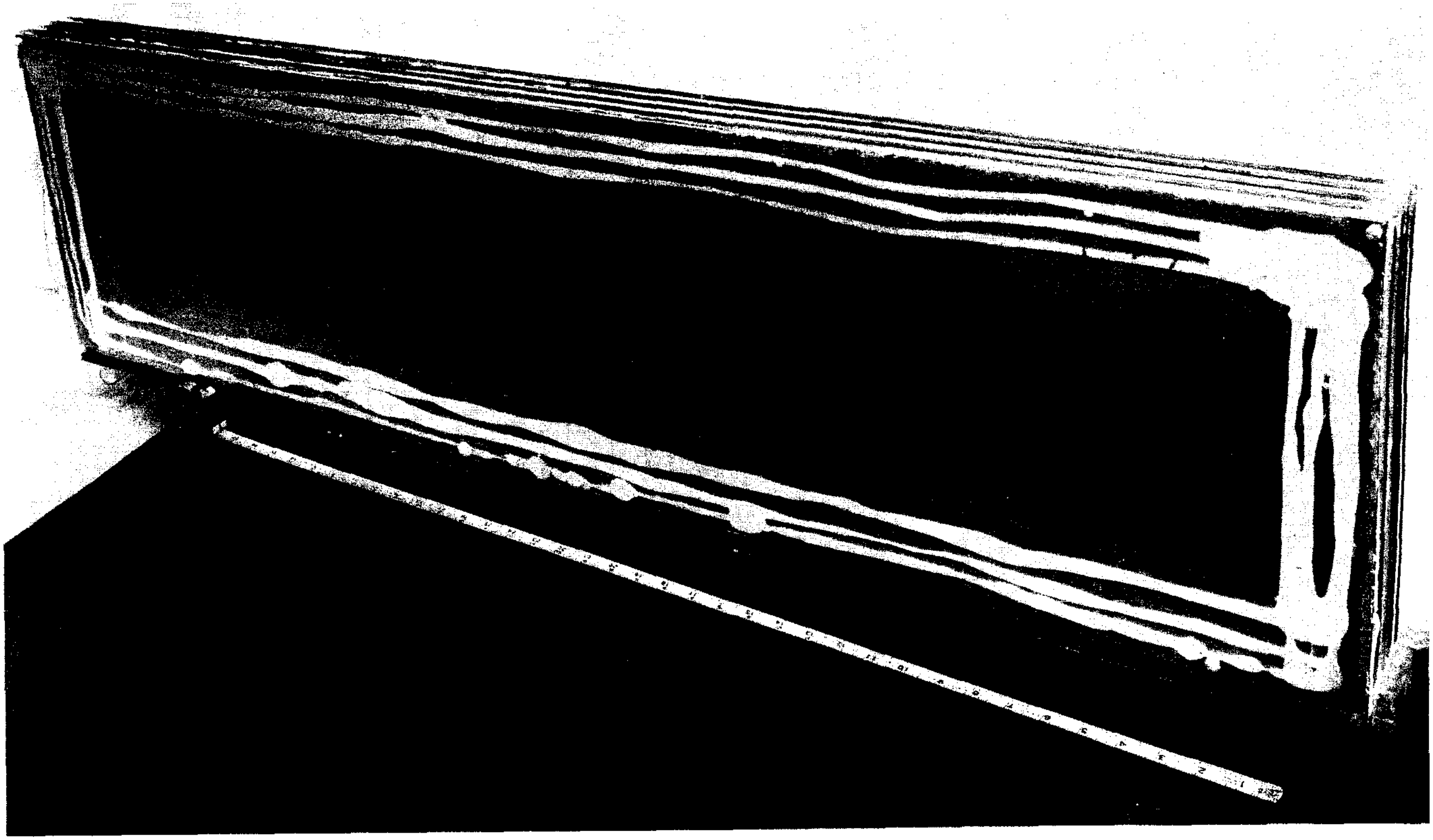

FIG. 10(a)--Photograph of a typical neutron spark chamber.

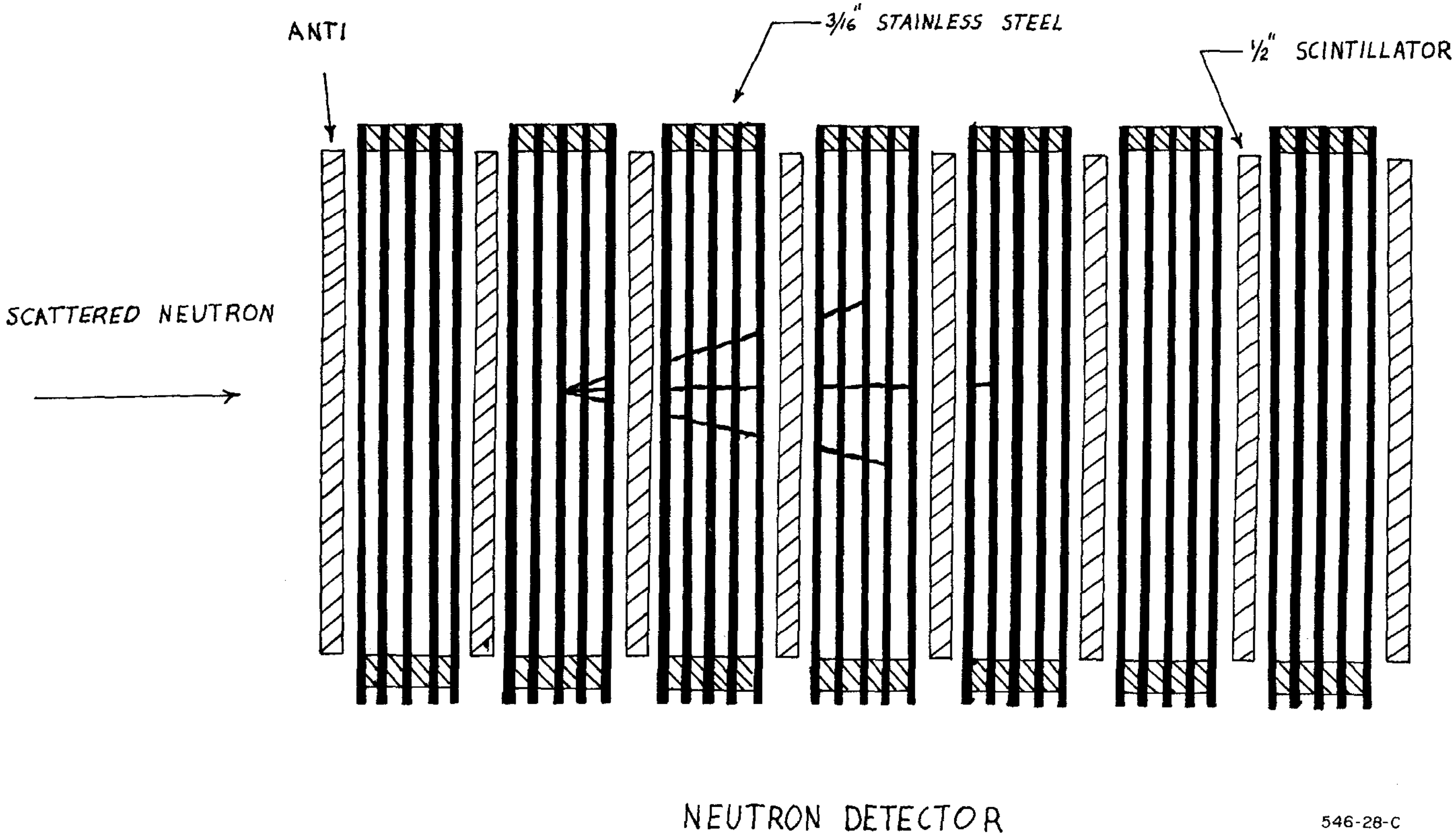

FIG. 10(b)--Sketch of neutron spark chamber detector array with the charged prongs from a neutron interaction shown.

The counters in the proton arm (P1 and P2) indicated the passage of a charged particle through the magnet system. P1, placed immediately after the first two spark chambers, was 6 inches high, 21 inches long, and 1/4 inch thick, and P2, placed after the spark chambers behind the magnet, was 9-1/8 inches high, 39 inches long, and 1/2 inch thick. 6810A photomultipliers were used on both counters. Because P1 was close to the magnet, a 3/8-inch-thick seamless steel tube was used in addition to the standard shield as protection against the fringe field.

Each of the seven counters in the neutron arm (N_i, i=1, 2, 3, . . . 7) was placed after one of the neutron detection chambers. These scintillators, made from scintillator with a 1/e attenuation length of 82 inches,[42] were 1/2 inch thick and 47 inches long. In order to reduce the trigger rate from particles not coplanar with the incident beam and the recoil proton, the neutron counters were shaped as shown in Fig. 11. The height of the ends placed closest to the unscattered neutron beam was 7.0 inches, while the height at the other end was 11.6 inches. 6810A photomultipliers were used on all the neutron counters.

Two scintillators were used as anti-coincidence counters to reject charged particle scattering. The first anti-counter, A1, was placed upstream of the liquid hydrogen target to insure neutrals in the beam. A1 was 1/16 inch thick, 1-1/8 inches square, and was viewed by a 56 AVP photomultiplier. The second anti-counter, A2, was located in front of the neutron chambers as shown in Fig. 10b. A2 was the same shape as the neutron counters and was viewed with a 6810A photomultiplier.

There were four sets of scintillation counter telescopes (the G, H, B, and M monitors) to monitor the intensity of the neutron beam. Their positions are indicated on Fig. 12. The B telescope consisted of three 1/2-inch by 1/2-inch

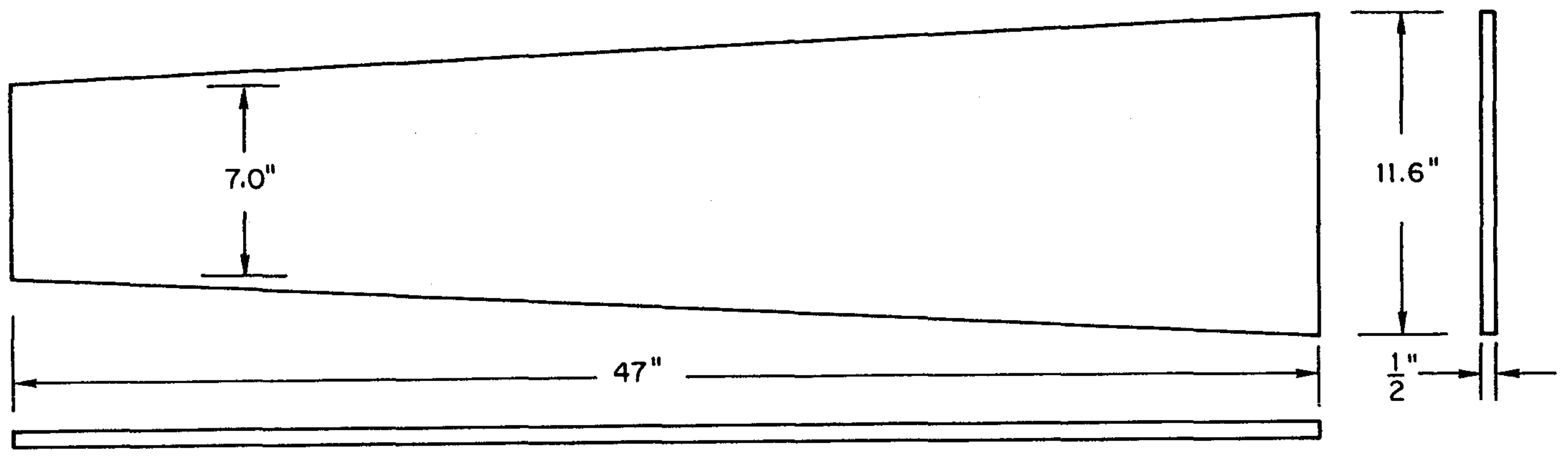

FIG. 11--Design of neutron scintillation counters.

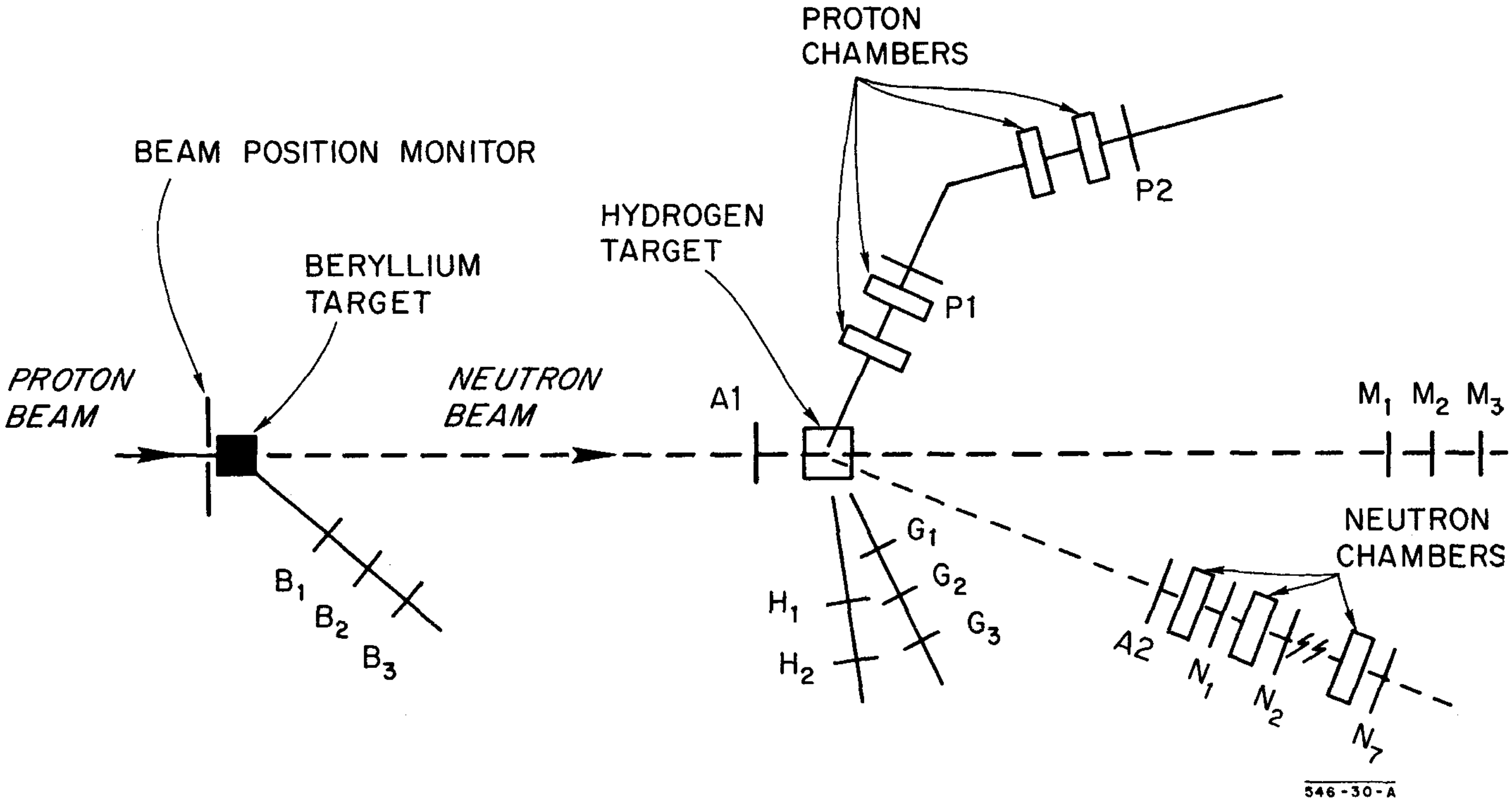

FIG. 12--Relative positions of all scintillation counters.

by 3/8-inch scintillators mounted on 53 AVP photomultiplier tubes. B was located approximately 7 feet below the Be target. The M counters were three 1/2-inch by 1/2-inch by 3/8-inch scintillators on 53 AVP's and were located in the main experimental area, approximately 15.5 feet from the liquid hydrogen target and at an angle of 0° 0.5' with respect to the central ray of the neutron beam. The G counters were three 1-inch by 1-inch by 3/8-inch scintillators viewed with 6810A's. G was located 15.7 inches from the center of the hydrogen target along a line passing through the center of the target and making an angle of 52.5° with respect to the neutron beam and an angle of 51° with respect to the plane of the rail system. The H telescope consisted of two 1-inch by 1-inch by 3/8-inch scintillators on 53AVP's and was mounted in the same fashion as G. For H, the distance to the target was 18.6 inches; the angle with the beam was 68°, and the angle with respect to the rail system was 55.5°.

VI. TRIGGERING SYSTEM AND OPTICS

A. Electronics

The triggering system consisted of the two scintillation counters in the proton arm, P1 and P2, and the seven counters, (N_i, i = 1, 2,. . . 7), in the neutron arm. The spark chambers were pulsed whenever a coincidence occurred among P1, P2, and any two successive neutron counters. This combination indicated that a charged particle had passed through the magnet and that an interaction had occurred in the neutron chambers. There were also the requirements that there be a neutral particle in the incident beam ($\overline{A1}$) and a neutral entering the neutron chamber array ($\overline{A2}$). Thus, the complete trigger requirement (see Fig. 12) was:

$$\overline{A1}\ \overline{A2}\ P1\ P2\ N_i\ N_{i+1}\quad i = 1, 2, \ldots 6 \tag{31}$$

The fact that the proton and neutron counters were quite long in the horizontal plane compared with their heights made the triggering requirement (Eq. 31) serve as a rough indication that the event was coplanar. This proved to be quite effective, for in the region where the apparatus measured small angle scattering (small $|t|$), over eighty-five percent of all triggers turned out to be elastic events.

The logic necessary to obtain this system is indicated schematically in Fig. 13. Most of the elements were General Applied Science Laboratories[43, 44] modules. The pulses from all the photomultipliers were voltage-limited to protect against large pickup pulses. As shown, the limiter outputs were split where necessary with IH-75 Fanouts.[45] A preliminary coincidence was made between $\overline{A1}$ P1 P2 (the "P" coincidence), and the output from this circuit was

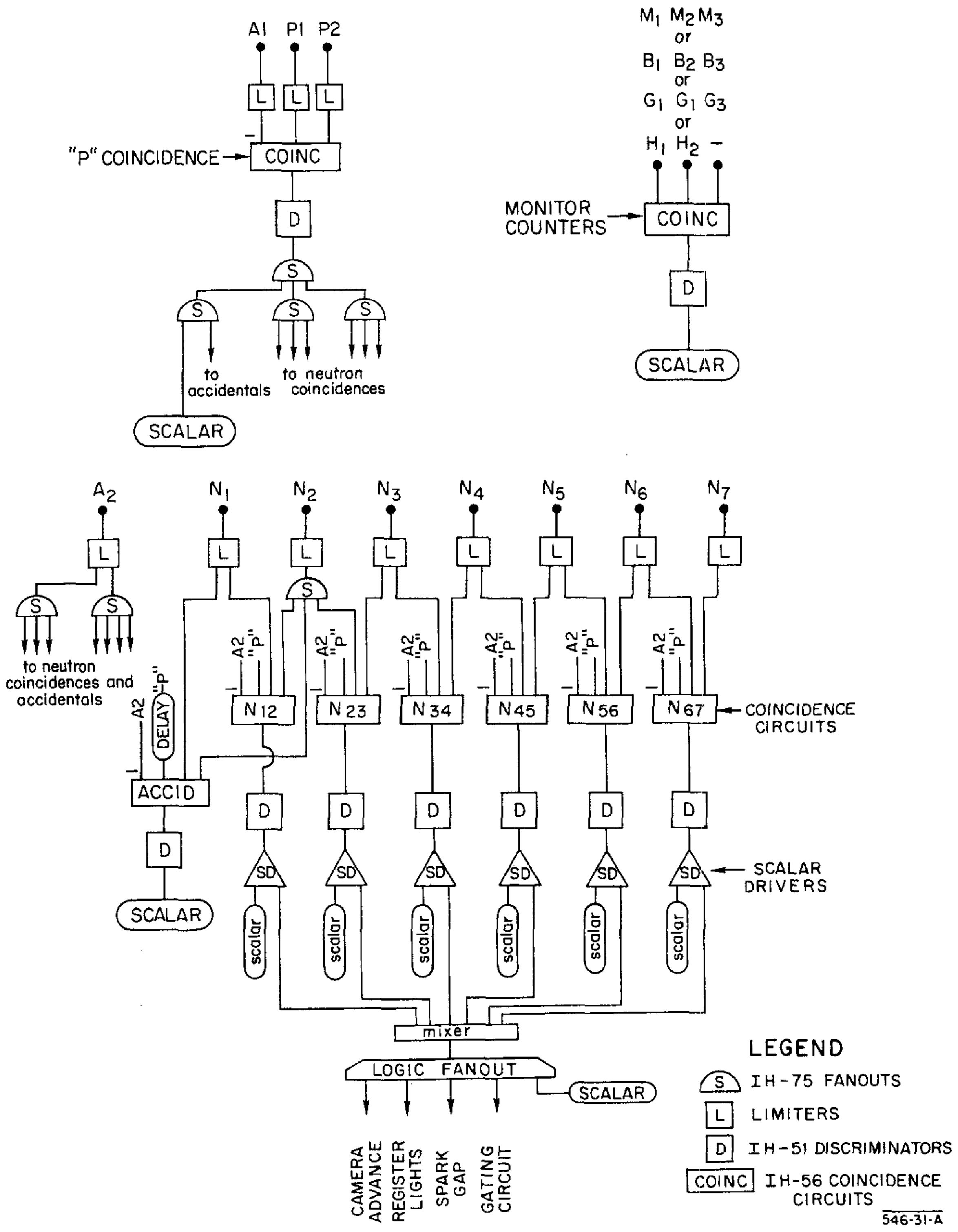

FIG. 13--Block diagram of electronic logic.

split and placed in coincidence with successive pairs of N counters. The outputs from all six of these "$N_{i, i+1}$" coincidences were fed through a "mixer," that is, an "or" gate, the output of which triggered the spark chambers, advanced the camera, flashed register lights, advanced registers, and so forth. IH-56 coincidence circuits[46] and IH-51 discriminators[47] were used to form the coincidences and shape the output pulses.

The spark chambers were fired using a spark gap[48] as a high voltage switch to dump the energy stored in a 6800-pF capacitor at a potential of 15 kV into each chamber. In order to prevent pickup from the spark chambers from causing trouble with the counters and to allow the capacitors sufficient recharging time, all the electronics was gated off for 60 msec after each firing of the spark chambers.

The counting rates in the "P" coincidence and all the "$N_{i, i+1}$" coincidences, as well as the total number of triggers, were recorded on scalars. The scalars also recorded the counting rates in the four sets of monitor telescopes, H, B, G, and M. A check on the accidental rate was obtained by duplicating one of the "$N_{i, i+1}$" coincidences but delaying the input of the "P" coincidence.

Periodic checks on the performance of the scintillation counters as well as the logic system were made using small corona lamps.[49] Because these lamps simulated the scintillations from the passage of charged particles, they were attached to each scintillator and were used as timing lamps.

B. Optics

The fiducial system involved the use of electroluminescent plastic lamps.[50] The fiducial marks were obtained by placing these lamps behind cutouts in a fiducial mask. As described elsewhere,[51, 52] such a system has the following advantages over a system employing an illuminated reticle:

(1) Accuracy is improved, as the edges determined by the fiducial mask are very well defined.

(2) The arrangement of fiducials is more flexible.

(3) The uniformly lit areas provided are convenient for experiments designed to use automatic analysis systems.

In order to put the fiducial masks on the film, the fiducials were pulsed for 10 msec with a wave train having a frequency of 5 kc/sec and a peak voltage of 500 volts. A sketch of the fiducial system is shown in Fig. 14a. The resistors were used to protect the lamps by limiting the peak currents and increasing the rise time of the pulses from the driver. A sketch of two of the spark chambers and the fiducials is shown in Fig. 14b. The large areas of the fiducial marks were designed to accomodate an automatic measuring system and the small dots were used in hand measurement. In addition to these fiducials, there were also a large number of lamps that were only turned on for a few calibration pictures at the start of every run.

The spark chambers were photographed by a system involving an intricate arrangement of mirrors. As sketched in Fig. 15a, there was a mirror for each chamber that allowed both views of the chamber to be observed from above. The proton chambers had individual stereo mirrors, while all seven neutron chambers shared a common stereo mirror. As can be seen in Figs. 15b and 15d, the light from the i^{th} neutron chamber was reflected in the i^{th} neutron mirror, NM_i, brought to a mirror located over the hydrogen target (NTM), and then transported to the camera, which was located outside the experimental blockhouse. (See Fig. 8.) The use of the seven neutron mirrors (NM_i, $i = 1, 2, \ldots 7$) enabled equilization of the light paths for the different chambers. Because each mirror could be adjusted independently, there was no need to use a field lens to view the entire active volume of each chamber.

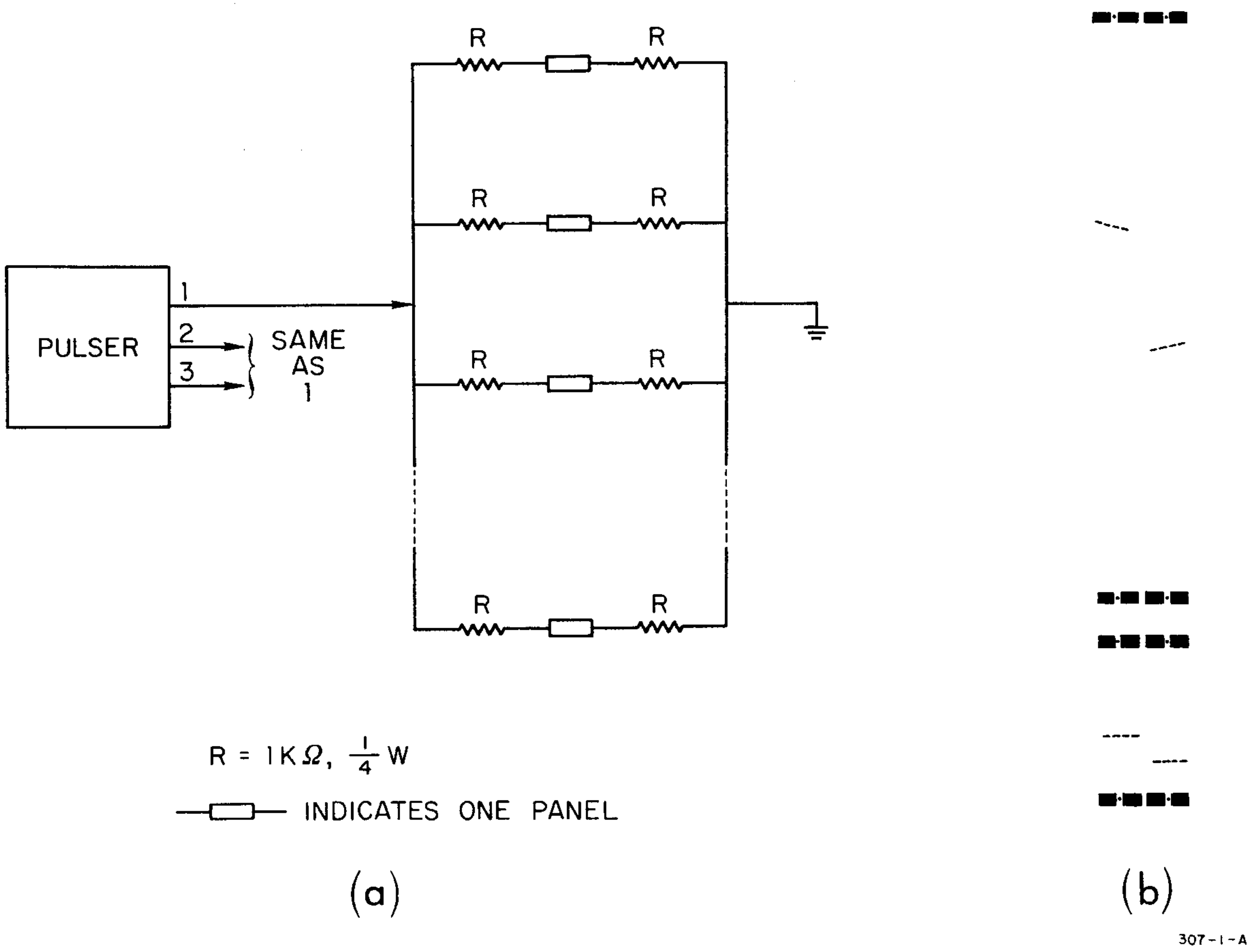

FIG. 14--Layout of fiducial system: (a) Block diagram of driver system; (b) A sketch of two typical spark chambers, top and side views, as they appeared on the film.

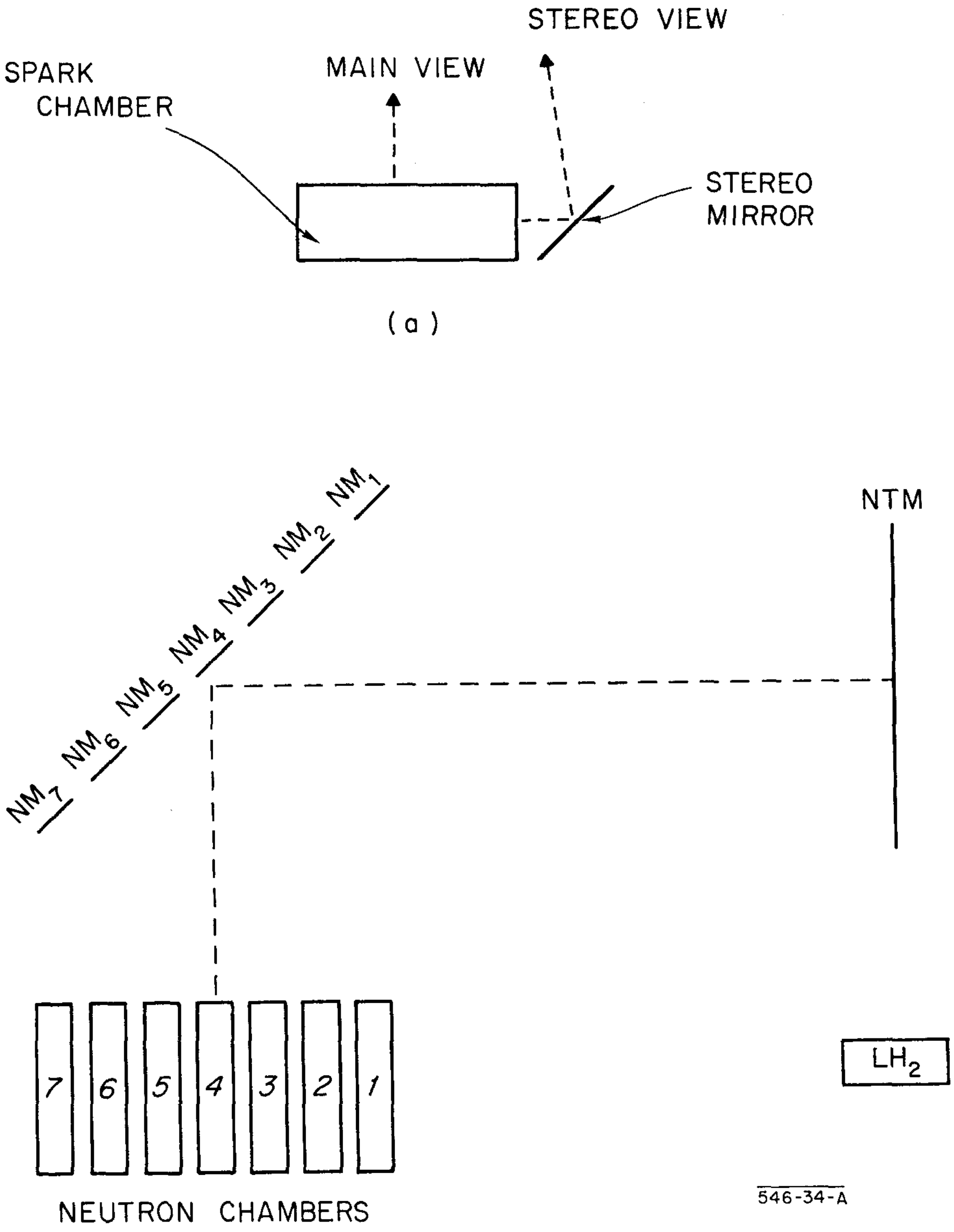

(b)

FIG. 15--Mirror system: (a) Stereo mirror arrangement;
(b) Mirrors for neutron arm.

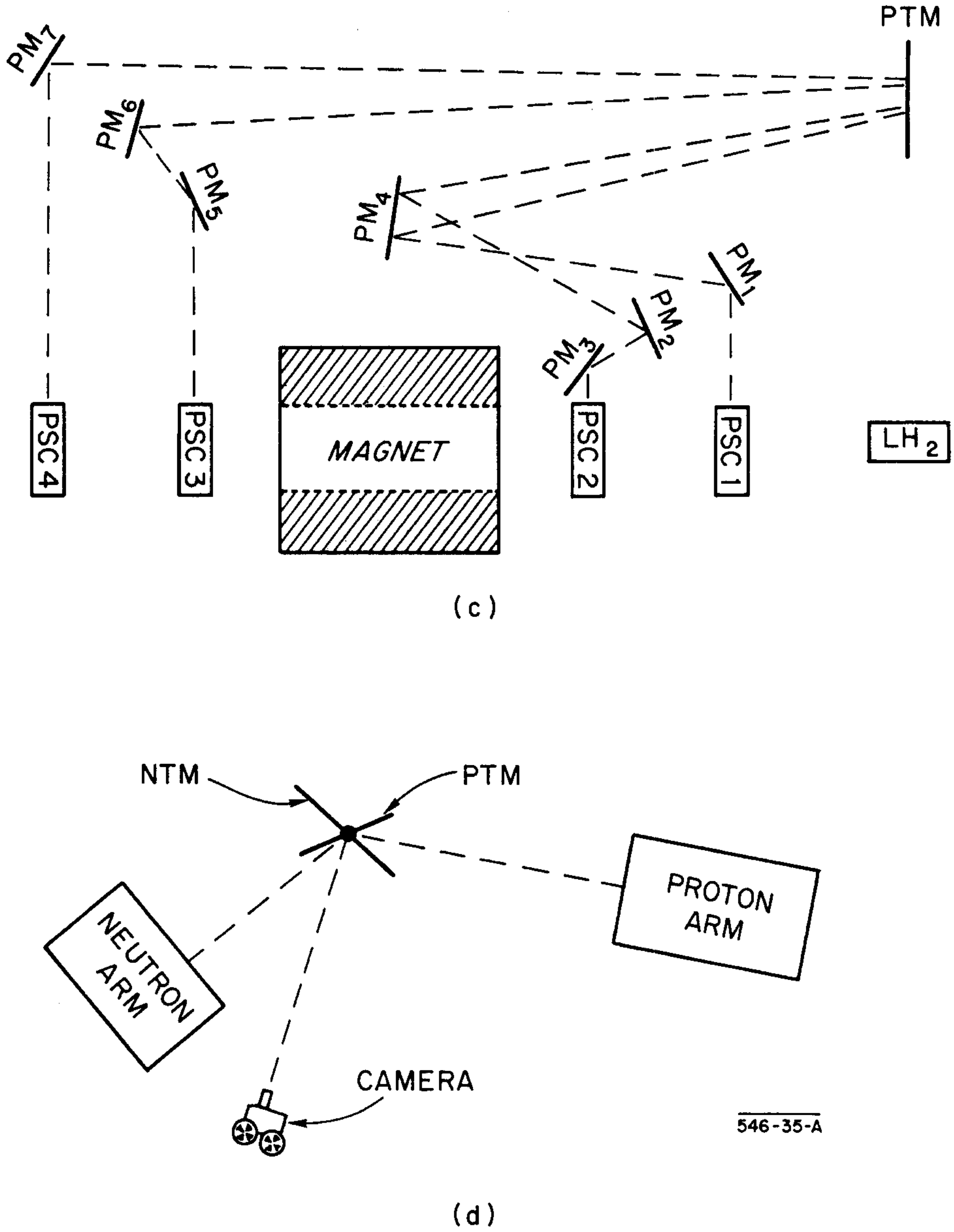

FIG. 15--Mirror system: (c) Mirrors for proton arm; (d) Mirrors located over hydrogen target used to transport the light to the camera.

As shown in Fig. 15c and 15d, the situation for the proton chambers was not as straightforward. To equalize the light paths and to insure that the magnet structure did not obscure any portion of a mirror, the light paths were folded many times. The light from the last proton spark chamber (PSC_4) was reflected in PM_7, brought to a mirror over the target (PTM) and then to the camera. The light paths for the other chambers were:

PSC_3: $PM_5 \rightarrow PM_6 \rightarrow$ PTM $\rightarrow$ CAMERA
PSC_2: $PM_3 \rightarrow PM_2 \rightarrow PM_4 \rightarrow$ PTM $\rightarrow$ CAMERA
PSC_1: $PM_1 \rightarrow PM_4 \rightarrow$ PTM $\rightarrow$ CAMERA

The nominal light path was 400 inches long. The mirrors over the target (PTM and NTM) could be rotated around an axis perpendicular to the plane of the rail system and passing through the center of the rails. Thus, regardless of the relative positions of the neutron and proton arms, PTM and NTM could be rotated to produce the same format on the film.

The information from the spark chambers, as well as information from a data board containing the event number and run number, was recorded on one frame of 35-mm film. The lens used was a 150-mm focal length Schneider-Kreuznach Symmar and had an aperture setting of f/8. During the course of the experiment, approximately 600,000 pictures were taken on Eastman Linograph Shellburst film.[53] The film was developed at a speed of 25 feet/min in Kodak Extra Fast X-Ray developer. The camera was designed[54] to take up to seven pictures during the 300-msec beam spill.

A typical picture is shown in Fig. 16a and the important features are indicated in Fig. 16b. The bend in the proton's path due to the magnet can be seen, and an easily identifiable neutron interaction is present in the neutron chambers. The fiducials and the data box are also shown.

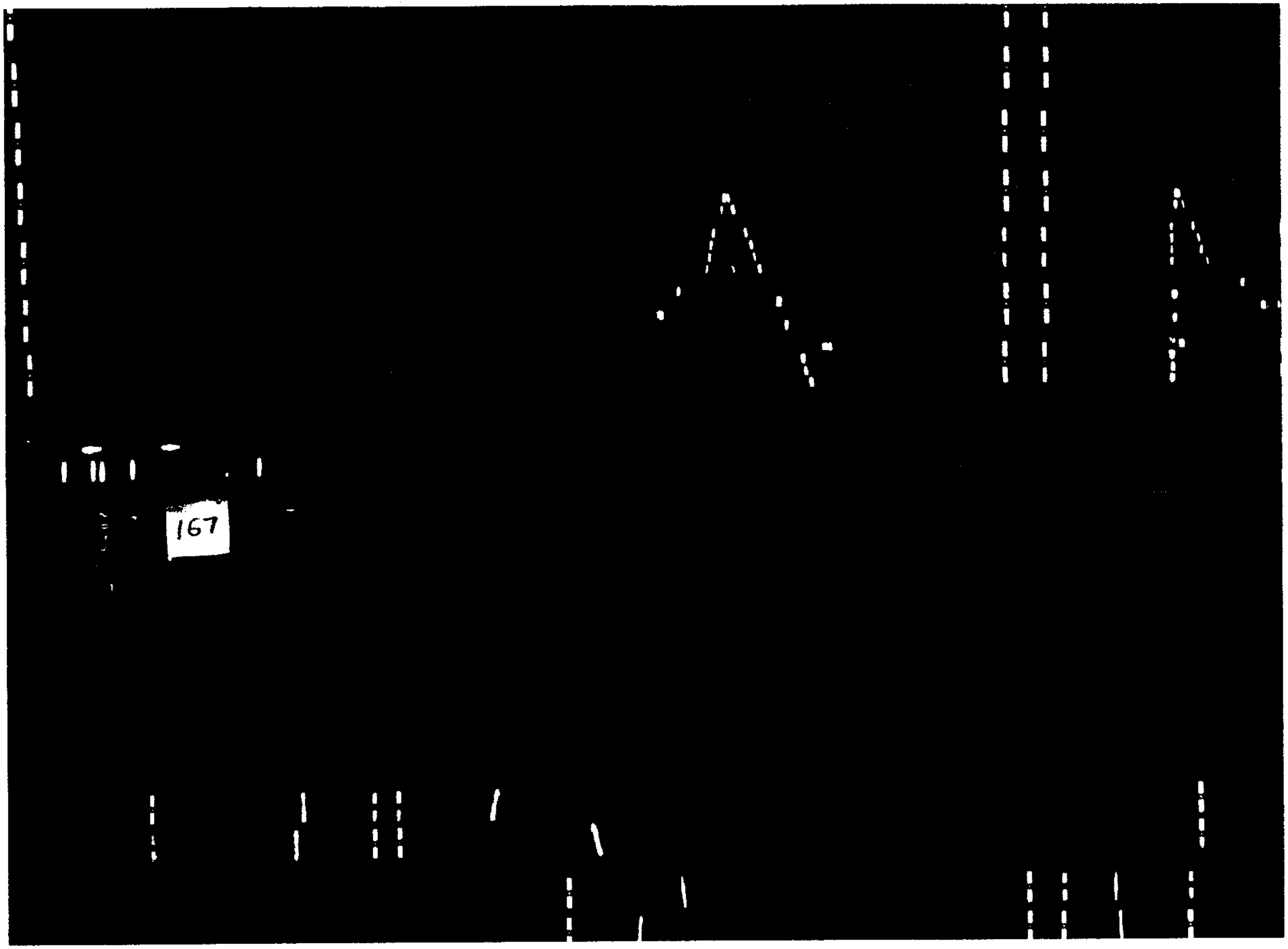

FIG. 16(a)--Print of a typical event frame.

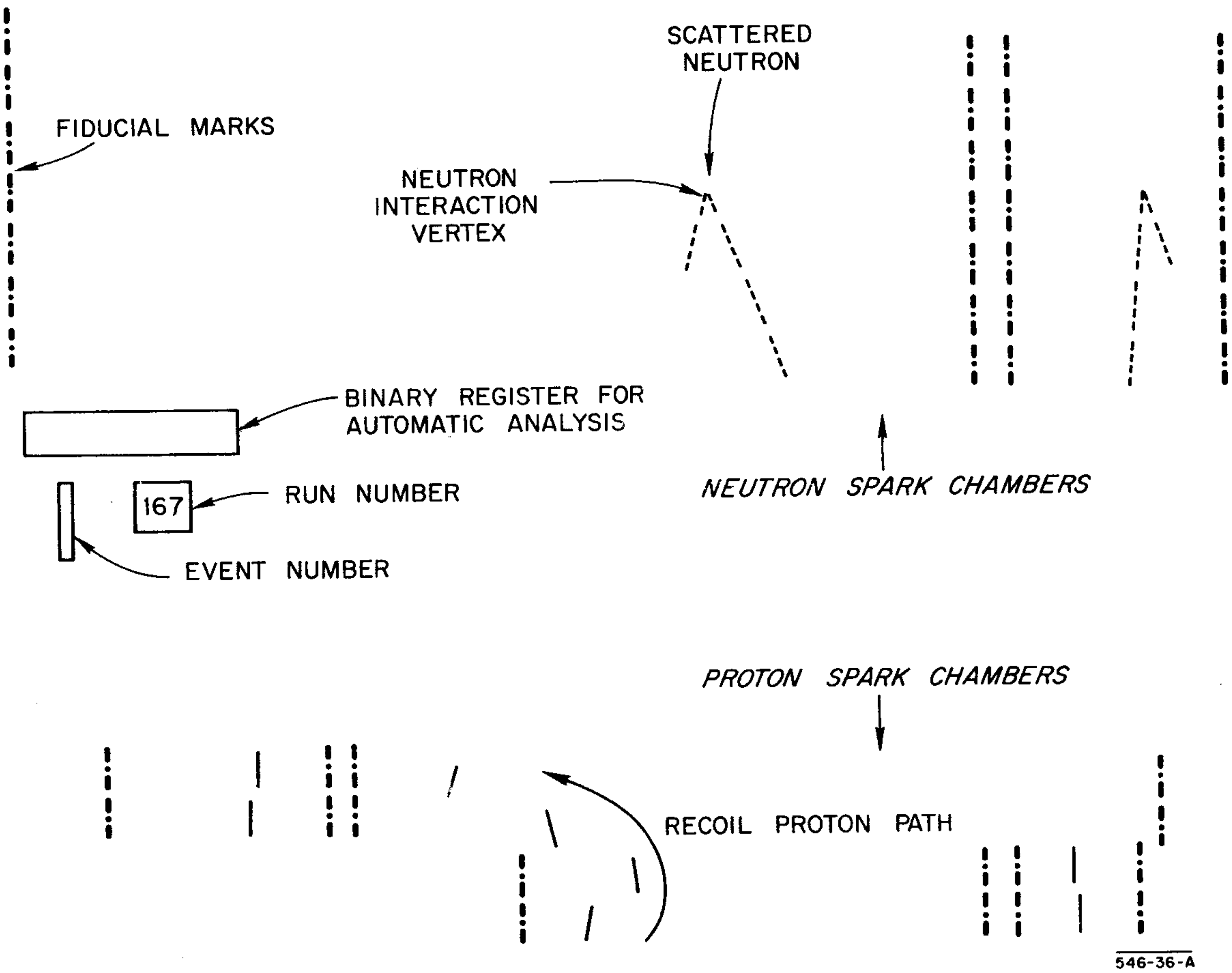

FIG. 16(b)--Explanation of event shown in Fig. 16(a), indicating the data box, the fiducials, the neutron interaction, and the bend in the proton path.

VII. DATA REDUCTION

The film was scanned for possible elastic scattering events, and frames that satisfied all selection criteria were measured. In order for an event to be considered an elastic scattering candidate, the following criteria had to be met:

(1) All proton chambers had to have a track present and the tracks had to indicate that a positive particle had passed through the magnet. This requirement eliminated events in which the particle was negative (probably π^-) and those in which a positive particle had undergone a large-angle scatter from the pole tips or coils of the magnet.

(2) There had to be an identifiable neutron interaction or neutron star in the neutron chambers. In order to facilitate the recognition of the neutron stars by the scanners, five classes of interactions were used. These neutron event types and their topologies are sketched in Fig. 17. Type 1 consisted of a single charged particle; Type 2, a two-pronged Vee; Type 3, a multi-pronged star with all prongs going in the forward direction, that is, in the direction of the scattered neutron; Type 4, a shower; and Types 5a and 5b, stars with prongs going in the backward direction.

Events that satisfied these criteria were measured using a Vanguard[55] measuring machine which utilizes a film plane digitizer with a least count of 10^{-4} inches on the film. The measurements made on each frame were the following:

(1) Three fiducials

At the start of each frame, three fiducials were measured in order to correlate the measurements with a master fiducial grid that allowed accurate

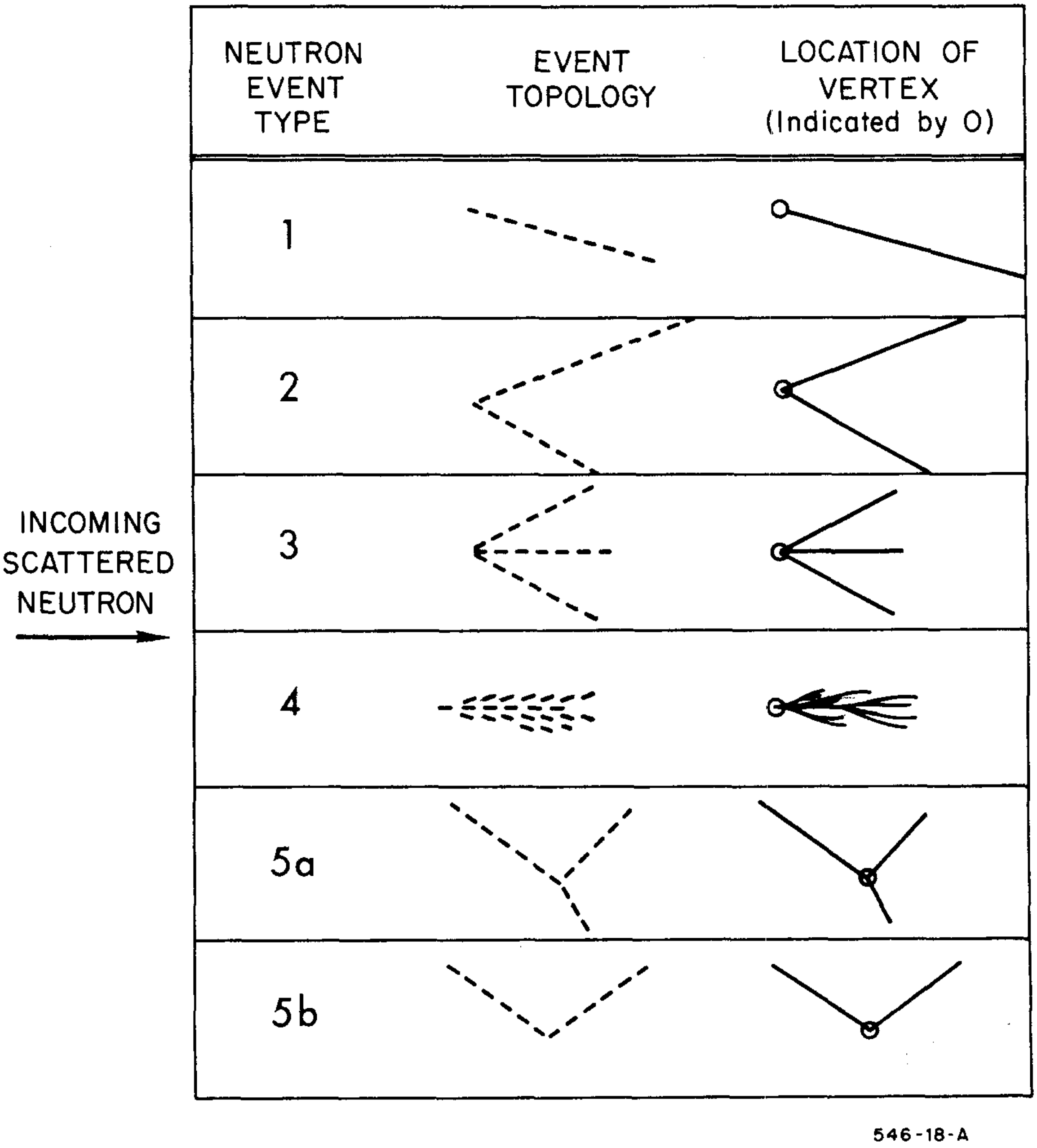

FIG. 17--Neutron event types and topologies. The interaction vertex for each type is indicated.

knowledge of the positions of the spark chambers. Three fiducials enabled a least square fit to be made which corrected for translation, rotation, and magnification.

(2) Proton sparks

In each of the four proton chambers, there were at most four sparks lying along the path of the particle. In each view of the chambers, one of these sparks was selected and the location of the center of this spark was digitized. It was found that the center of a spark on the film plane could be measured to ± 5 microns in the direction perpendicular to the proton trajectory and ± 10 microns along the length of the spark.

(3) Neutron sparks

In each view of the neutron chambers, sufficient sparks on the prongs of the neutron interaction were measured to determine the location of the neutron interaction vertex. The number of prongs used and, thus, the number of sparks that had to be measured varied with the class of interaction. Types 2, 3, and 5 required the measurement of two prongs in each view, the intersection of which yielded the vertex point. A single prong was sufficient for Types 1 and 4. In Type 4, the central ray at the start of the shower was the prong chosen. For these two types, the intersection of the prong and the center of the spark chamber plate immediately before the start of the event determined the vertex point. A sketch of the location of the vertex points for the various classes of events is shown in Fig. 17.

The digitizations of the spark locations were punched onto IBM cards by an IBM 526 Summary Card Punch. Additional information about each event was entered onto these cards by means of a parameter board. This information included the register number of the frame, a scanner identification code, the neutron event class, the run number, the date of measurement, and a code indicating the measuring machine used. This information was transferred to magnetic tapes to serve as the input to a kinematics reconstruction program.

If there were two separate, identifiable neutron types in the neutron conversion chambers, the frame was measured twice, each time with one of the neutron types. A code in the parameter board indicated this duplication, and the chi-squared fitting program to be discussed later selected the neutron type resulting in the best fit or lowest chi-squared. This measurement duplication was performed to minimize any neutron beam intensity-correlated bias in the selection process.

The efficiency for identification of neutron types and for indicating the neutron vertex correctly was measured by rescanning portions of the data. This efficiency, independent of the neutron type assigned, was found to be approximately ninety-five percent. There were, however, some disagreements regarding the neutron event classes assigned. If there was a prong of the star that was not very dark, the interaction could be called either Type 2, 3, or 5a. These disagreements did not affect the measurement of the neutron vertex, however, as the interaction vertex is in the same position for all these classes. There is the worry that there might be some energy-dependent bias inherent in the scanner selection criteria or in the performance of the scanners. Measurements were made to determine the existence of such biases and will be discussed later.

At periodic intervals, measurements were made of the entire fiducial grid. These measurements served as checks on the performance of the measuring machines and insured that any small change in the relative positions of the fiducials would be detected.

The events were reconstructed using the IBM 7090 Digital Computer with a program entitled BARBARA. Using the fiducials on the front and back of each view of each spark chamber, the sparks were put into their real space coordinates, correcting for the magnification of each chamber and taking the conical projection into account. As shown in Fig. 18, the conical projection allowed the true coordinates of a spark to be known only by combining the information from both views of a given chamber. Using these coordinates, the path of the recoil proton, determined from the two spark chambers closest to the target, was projected back into the liquid hydrogen. A candidate for elastic scattering has to originate inside the 10-inch-long cylinder defined by the beam and the central volume of the target, and, therefore, the proton vector had to pass through this volume. In the neutron arm, the interaction vertex was calculated as described above. The momentum of the recoil proton was then calculated by an integration through the magnetic field. The integration procedure is described below.

It can be shown[56] that if $\hat{t}$ is a unit vector along the direction of a particle, then

$$\frac{d\hat{t}}{ds} = \frac{e}{pc}\,\hat{t} \times \vec{B} \tag{32}$$

where s is the length along the particle's path, p is the absolute value of the momentum, and $\vec{B}$ is the magnetic field. Knowledge of the magnetic field at every point then makes it possible to trace the trajectory of a charged particle in the field. The momentum is determined by requiring that the trajectory pass through measured points. For the analysis of this experiment, there were three points used to determine the momentum—the tracks in the two chambers on the side of the magnet furthest from the hydrogen target and a point in the scintillator P1. This latter point was determined by projecting the path of the

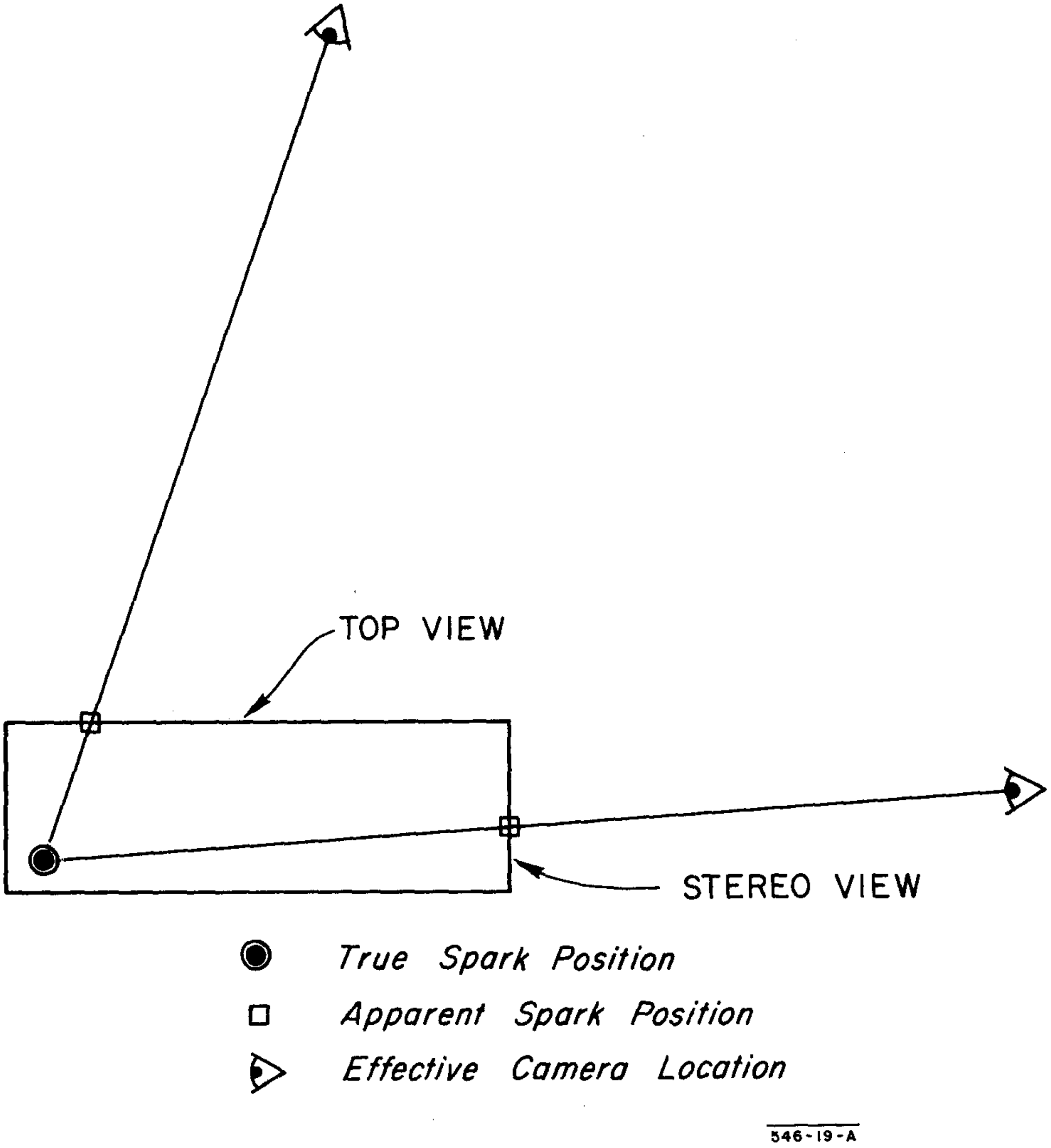

FIG. 18--Conical projection. The true coordinate of a spark could only be determined by using the information from both views of a chamber.

proton calculated from the front chambers into the P1 scintillator. The locations of the sparks in the first two spark chambers could not be used directly in the momentum calculation because Coulomb scattering in scintillator P1 introduced a random change in the trajectory of the proton.

The calculation proceeded as follows:

1. A first choice for the momentum was made using the differences between the entrance and exit angles.
2. The last two spark chambers gave a starting value of $\hat{t}$.
3. The magnetic field $\vec{B}(x, y, z)$ was known at every point on the trajectory from a linear interpolation between measured values of the field. Every point in the magnet could be considered to be inside a small box, on the corners of which the magnetic field had been measured, and these eight values were interpolated to the point under consideration. An estimate of the horizontal components of the magnetic field was made using an approximation to one of Maxwell's equations:

$$B_y \approx \frac{\partial B_z}{\partial y} \Delta z \tag{33}$$

4. Using Eq. (32) the trajectory was traced through the magnet in one-inch steps. At each point, checks were made to insure that the proton did not hit either the pole tips or coils of the magnet.
5. If the intersection of this path and scintillator P1 did not agree with the "measured point," the momentum was corrected and the integration through the field was repeated.

Agreement between the two points was usually obtained in at most three iterations. The momentum calculated in this manner had to be corrected for the finite size of the integration step. A one-inch step size introduced approximately a 1.5% systematic shift in the momentum such that the calculated momentum was always too small. This correction factor was ascertained by varying the step size for different momenta at each value of the magnetic field. One of the curves used to estimate the factor showing the calculated momentum as a function of the step size is shown in Fig. 19a. Figure 19b shows that the factor is a constant percentage of the momentum at a given magnetic field. The maximum error introduced by this correction factor is less than 0.1 MeV/c.

The momentum determinations depended on accurate knowledge of the relative positions of the front and back spark chambers. In order to check the alignment of the apparatus, a number of pictures were taken at each setting with zero field in the magnet. The tracks in the front and back sets of chambers were then projected into scintillator P1. Figure 20 is a histogram of the distance of the position determined by the front chambers from the position determined by the back chambers. A non-zero value of this distance is shown in the coordinate x measured along the length of P1 ($x_{front} - x_{back}$). This indicates a slight shift of the relative positions of the two sets of chambers. The width of the distribution is due to multiple Coulomb scattering of very low momentum protons.

The momentum calculated in the manner described above was the momentum at the center of the magnet-spark chamber system. In order to find the momentum at the scattering point, the momentum was corrected for energy loss along its path. The energy losses in the scintillation counter, in the air, in the Mylar, and in the aluminum through which the proton passed were calculated using the latest tabulated values.[57] The energy loss in the liquid hydrogen was computed using a standard momentum to range – range to momentum subroutine, PINTOR

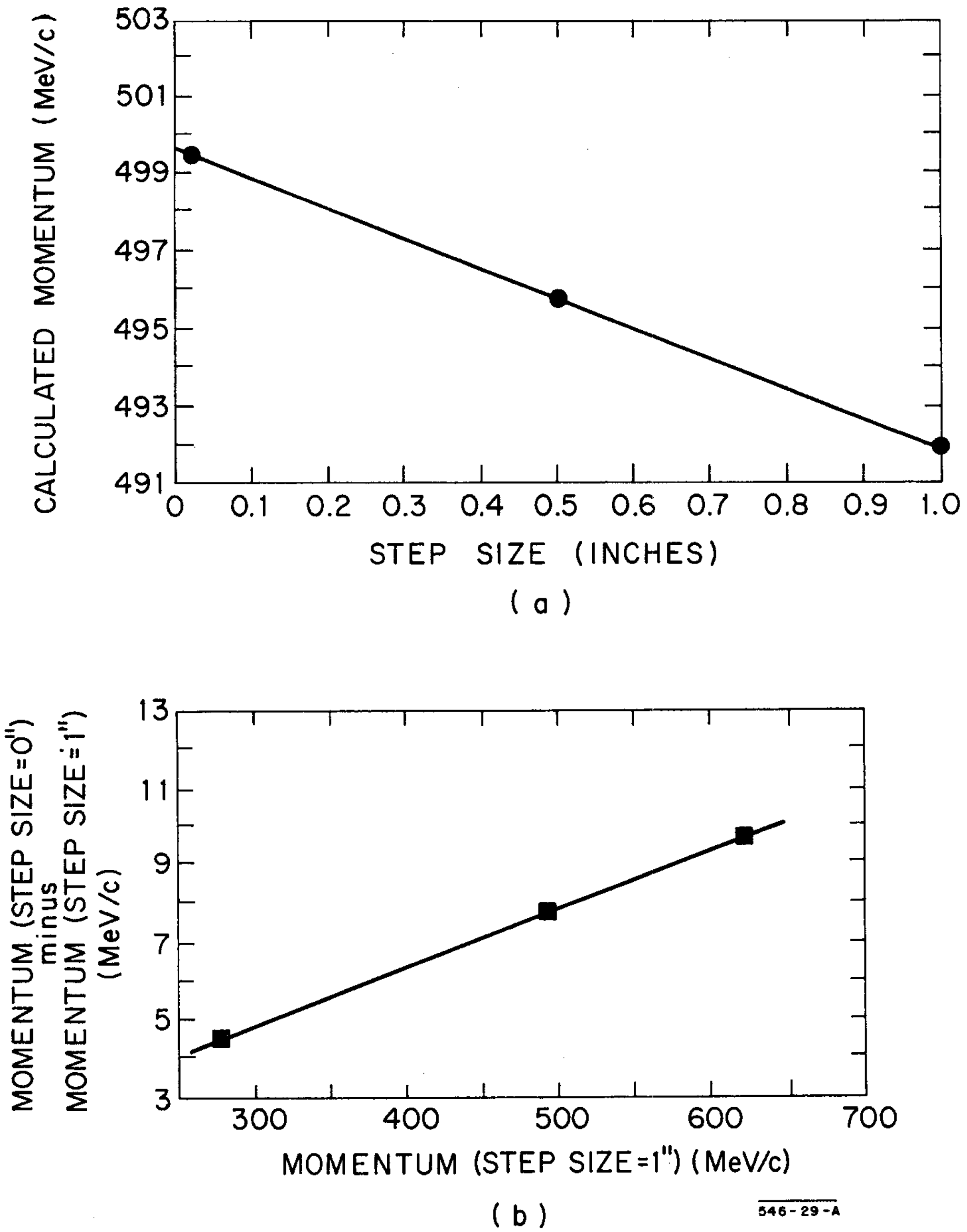

FIG. 19--Momentum correction factor: (a) Calculated momentum as a function of the magnetic integration step size; (b) Linearity of correction factor with momentum for a fixed magnetic field.

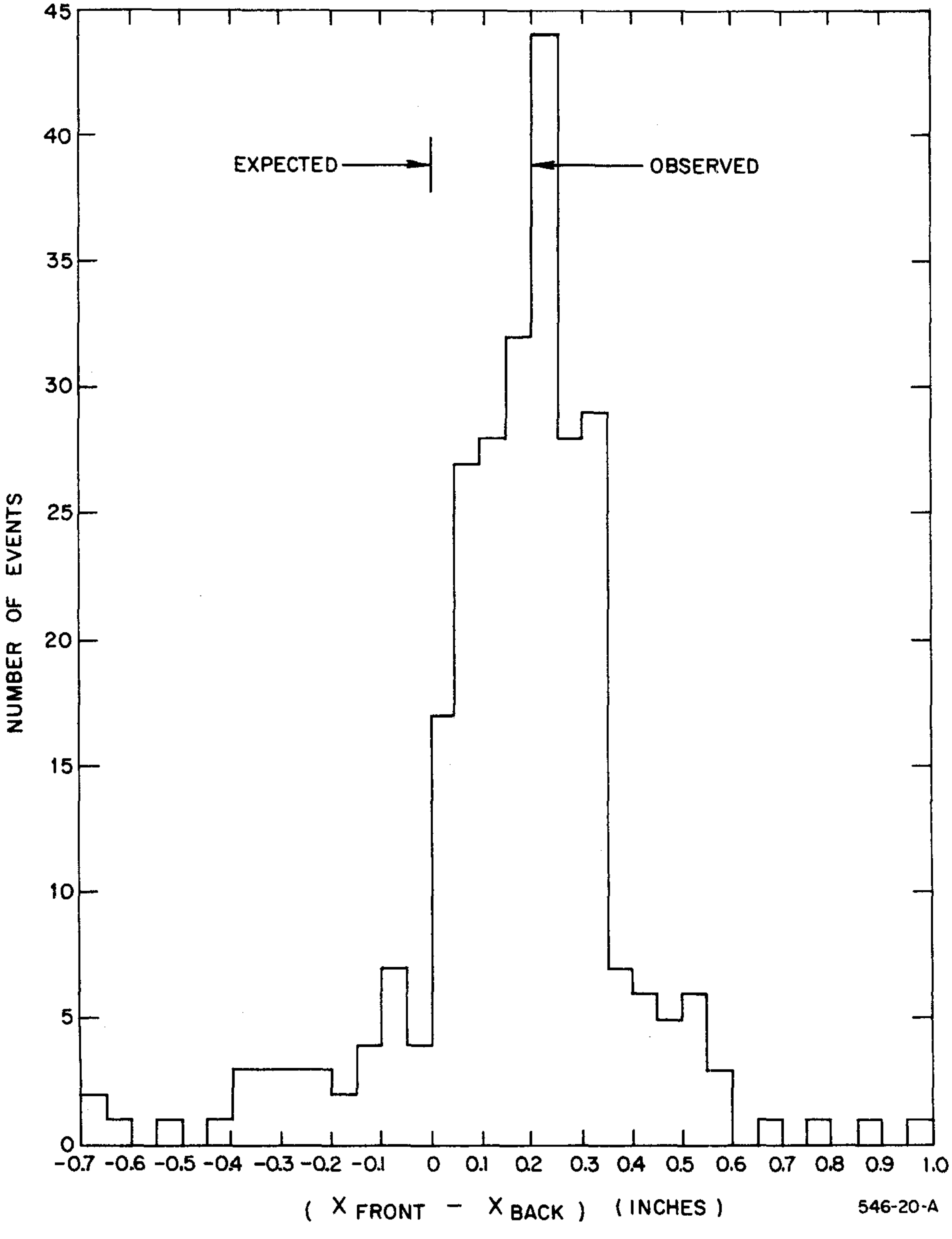

FIG. 20--Alignment check of the proton spark chambers. The non-zero value of $x_{front} - x_{back}$ indicates a slight shift of the relative positions of the front and back chambers.

and RINTOP.[58,59] A first guess at the location of the scattering point was the closest approach of the proton's path to the central ray of the incident neutron beam. The final selection of the scattering point is discussed below.

After an event had successfully gone through the kinematics program, the information about the recoil proton vector, the proton momentum, and the neutron interaction point was fed into a program entitled FIT, which adjusted the measured quantities using the method of least squares, subject to non-linear constraints, yielded a value of chi-squared for these adjusted quantities, and wrote the results on magnetic tape.

The program FIT is closely patterned after GUTS,[60] a fitting routine that is commonly used in the analysis of bubble chamber data. The value of chi-squared for each event is minimized using the non-linear constraints of momentum and energy conservation. The general fitting procedure is described below following the presentation of Berge,[60] and then the specific method used in this experiment is discussed.

The basic inputs to the fitting program are (1) the T measured quantities, x_i^M, $i = 1, 2 \ldots T$; (2) the error matrix, G_{ij}, defined such that

$$G_{ij}^{-1} = \overline{\delta x_i^M \, \delta x_j^M}$$

and (3) the constraint equations. We note that the diagonal elements of the error matrix are just the squares of the errors in the measured quantities. The error matrix for this analysis was taken to be diagonal; that is, there were no correlated errors in the measured quantities,

$$G_{ij}^{-1} = (\text{error in } x_j^M)^2 \quad \delta_{ij} \; .$$

The quantity to be minimized, χ^2, is defined as

$$\chi^2 = \sum_{i,j=1}^{T} (x_i - x_i^M)\, G_{ij}\, (x_j - x_j^M) \tag{34}$$

However, one must include in the calculation the constraints of energy and momentum conservation

$$F_\lambda (x_i) = 0 \qquad \lambda = 1, 2, \ldots, c$$

by introducing Lagrange multipliers, α_λ. Thus, one wants to minimize

$$I = \sum_{i,j=1}^{T} (x_i - x_i^M)\, G_{ij}\, (x_j - x_j^M) + 2 \sum_{\lambda=1}^{c} \alpha_\lambda\, F_\lambda (x_i) \tag{36}$$

with respect to x_i and α_λ subject to Eq. (35). The conditions are

$$\frac{\partial I}{\partial x_i} = 0 = 2 \left\{ \sum_{j=1}^{T} G_{ij}\, (x_j - x_j^M) + \sum_{\lambda=1}^{c} \frac{\partial F_\lambda}{\partial x_i}\, \alpha_\lambda \right\} = 0 \tag{37a}$$

$$\frac{\partial I}{\partial \alpha_\lambda} = 0 = 2\, F_\lambda (x_i) = 0 \tag{37b}$$

Equation 37b is the same as Eq. 35. The problem is to solve these equations for x_i and α_λ. As the F_λ are non-linear, it is necessary to use an iterative process which can be expressed[60] in the following equations.

Given the values of the parameters at the ν^{th} iteration, x_i^ν and α_λ^ν, one can write

$$\begin{aligned}
F_{i\lambda}^\nu &= \left(\frac{\partial F_\lambda}{\partial x_i}\right)\Bigg|_{x_i = x_i^\nu} \\
E_{i\lambda}^\nu &= \sum_{j=1}^{T} G_{ij}^{-1} \; F_{j\lambda}^\nu \\
H_{\lambda\mu}^\nu &= \sum_{j=1}^{T} (E^\nu)_{\lambda j}^{\text{Transpose}} \; F_{j\mu}^\nu \\
b_\lambda^\nu &= F_\lambda^\nu + \sum_{j=1}^{T} (x_j^M - x_j^\nu) \, F_{j\lambda}^\nu \\
\alpha_\lambda^{\nu+1} &= \sum_{\mu=1}^{c} (H^\nu)_{\lambda\mu}^{-1} \; b_\lambda^\nu \\
x_i^{\nu+1} &= x_i^M - \sum_{\lambda=1}^{c} E_{i\lambda}^\nu \, \alpha_\lambda^{\nu+1}
\end{aligned} \tag{38}$$

The iteration begins with

$$x_i^o = x_i^M$$

$$\alpha_\lambda^o = 0$$

At every step, the value of χ^2 is calculated and the process is halted when a minimum χ^2 is found.

There are three measurable quantities associated with each particle at the interaction vertex. The Cartesian coordinate system chosen had its origin at the center of the liquid hydrogen target with the y-axis along the 0° beam and the z-axis pointed upwards (see Fig. 21). The angles θ and ϕ are defined in Fig. 21 with z as the polar axis. With this coordinate system, the measurable quantities for each particle are:

$$\begin{aligned} \boldsymbol{\Phi} &= \phi \\ K &= p \sin\theta \\ s &= 1/\tan\theta \end{aligned} \tag{39}$$

The energy and momentum conservation equations can be expressed in terms of these variables as follows:

$$K_1 s_1 - K_2 s_2 - K_3 s_3 = 0 \tag{40a}$$

$$K_1 \sin\boldsymbol{\Phi}_1 - K_2 \sin\boldsymbol{\Phi}_2 - K_3 \sin\boldsymbol{\Phi}_3 = 0 \tag{40b}$$

$$K_1 \cos\boldsymbol{\Phi}_1 - K_2 \cos\boldsymbol{\Phi}_2 - K_3 \cos\boldsymbol{\Phi}_3 = 0 \tag{40c}$$

$$E_1 + M_p - E_2 - E_3 = 0 \tag{40d}$$

where the subscripts 1, 2, 3 refer to the incident neutron, the scattered neutron and the recoil proton, respectively, and E_i is the total energy of the i^{th} particle. Because K_1 and K_2 are not measured, they are determined by Eqs. (40b) and (40c). This leaves only Eqs. (40a) and (40d) as the two constraint equations F_1 and F_2. For this reason, this type of event is referred to as a two-constraint or 2-c event class. All the partial derivatives used in the iteration process are listed in Fig. 22.

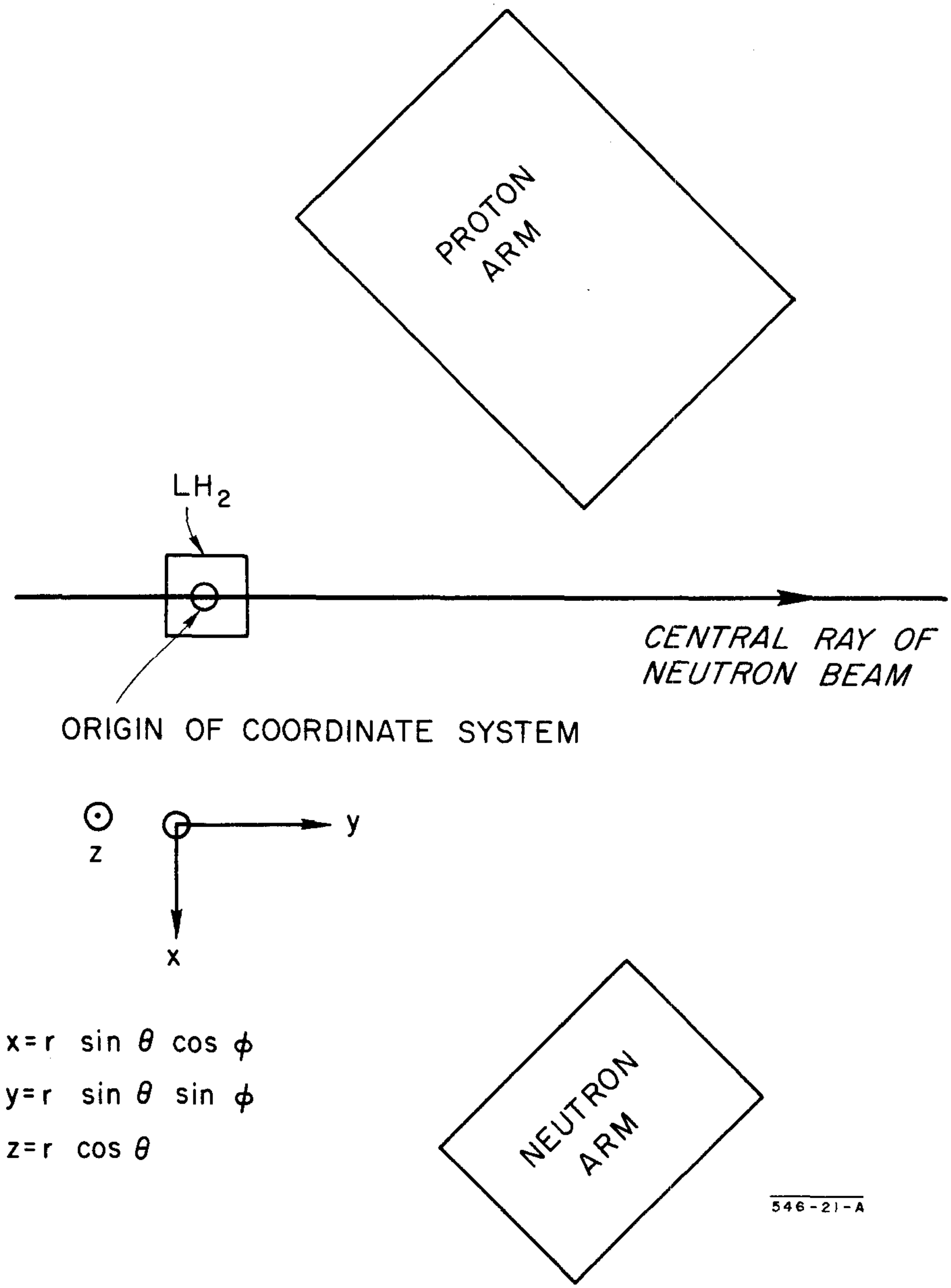

FIG. 21--Coordinate system used in FIT.

$$F_{\lambda\rho\sigma} \equiv \left(\frac{\partial F_\lambda}{\partial x_\rho}\right) \quad \text{for particle } \sigma$$

$$(x_1, x_2, x_3) = (\phi, s, K)$$

$$F_{111} = s_1 \frac{\partial K_1}{\partial \phi_1} - s_2 \frac{\partial K_2}{\partial \phi_1} \qquad F_{211} = \frac{(1+s_1^2)K_1}{E_1} \frac{\partial K_1}{\partial \phi_1} - \frac{(1+s_2^2)K_2}{E_2} \frac{\partial K_2}{\partial \phi_1}$$

$$F_{121} = K_1 \qquad F_{221} = \frac{K_1^2 s_1}{E_1}$$

$$F_{112} = s_1 \frac{\partial K_1}{\partial \phi_2} - s_2 \frac{\partial K_3}{\partial \phi_2} \qquad F_{212} = \frac{(1+s_1^2)K_1}{E_1} \frac{\partial K_1}{\partial \phi_2} - \frac{(1+s_2^2)K_2}{E_2} \frac{\partial K_2}{\partial \phi_2}$$

$$F_{122} = - K_2 \qquad F_{222} = - \frac{K_2^2 s_2}{E_2}$$

$$F_{113} = s_1 \frac{\partial K_1}{\partial \phi_3} - s_2 \frac{\partial K_2}{\partial \phi_3} \qquad F_{213} = \frac{(1+s_1^2)K_1}{E_1} \frac{\partial K_1}{\partial \phi_3} - \frac{(1+s_2^2)K_2}{E_2} \frac{\partial K_2}{\partial \phi_3}$$

$$F_{123} = - K_3 \qquad F_{223} = - \frac{K_3^2 s_3}{E_3}$$

$$F_{133} = \frac{s_1 K_1}{K_3} - \frac{s_2 K_2}{K_3} - s_3 \qquad F_{233} = \frac{(1+s_1^2)K_1^2}{E_1 K_3} - \frac{(1+s_2^2)K_2^2}{E_2 K_3} - \frac{(1+s_3^2)K_3}{E_3}$$

$$\frac{\partial K_1}{\partial \phi_1} = - \frac{K_1 \cos(\phi_1 - \phi_2)}{\sin(\phi_1 - \phi_2)} \qquad \frac{\partial K_2}{\partial \phi_1} = - \left(\frac{K_3 \cos(\phi_3 - \phi_1) + K_2 \cos(\phi_1 - \phi_2)}{\sin(\phi_1 - \phi_2)}\right)$$

$$\frac{\partial K_1}{\partial \phi_2} = - \left(\frac{K_3 \cos(\phi_3 - \phi_2) - K_1 \cos(\phi_1 - \phi_2)}{\sin(\phi_1 - \phi_2)}\right) \qquad \frac{\partial K_2}{\partial \phi_2} = K_2 \frac{\cos(\phi_1 - \phi_2)}{\sin(\phi_1 - \phi_2)}$$

$$\frac{\partial K_1}{\partial \phi_3} = K_3 \frac{\cos(\phi_3 - \phi_2)}{\sin(\phi_1 - \phi_2)} \qquad \frac{\partial K_2}{\partial \phi_3} = K_3 \frac{\cos(\phi_3 - \phi_1)}{\sin(\phi_1 - \phi_2)}$$

$$E_i = \left[K_i^2 (1 + s_i^2) + (\text{Mass})_i^2\right]^{\frac{1}{2}} \quad (i = 1, 2, 3)$$

FIG. 22--Partial derivatives used in FIT.

The error matrix G_{ij} was assumed to be diagonal and the error assignments used are listed in Fig. 23. Note that for low recoil proton momentum, the errors in the proton variables were determined by Coulomb scattering in the liquid hydrogen, in the aluminum vacuum jacket surrounding the target, and in the air through which the proton passed.

After these calculations were performed, the interaction point in the liquid hydrogen target was moved in one-inch steps along the line determined by the proton vector. At each point inside the liquid hydrogen target and inside the cylinder described by the intersection of the beam and the target volume, these calculations were performed and values of χ^2 were computed. The interaction point was then selected on the basis of the lowest value of χ^2.

Elastic events were then selected with the requirement that

$$\chi^2 \leq 8.0 \tag{41}$$

Events with χ^2 greater than this value have less than a 2% chance of being elastic events. Inelastic contaminations in the elastic sample due to this cutoff criteria will be discussed later.

$$G^{-1}_{ij} = \overline{\delta x_i \ \delta x_j}$$

$$(x_1, x_2, x_3, x_4, x_5, x_6, x_7) = (\phi_1, s_1, \phi_2, s_2, \phi_3, s_3, K_3) \qquad \begin{array}{ll} [\phi] & \text{radians} \\ [s] & \text{dimensionless} \\ [K] & \text{MeV/c} \end{array}$$

$$G^{-1}_{ij} = \begin{bmatrix} G^{-1}_{11} & & & & & & \\ & G^{-1}_{22} & & & & \text{\Huge 0} & \\ & & G^{-1}_{33} & & & & \\ & & & G^{-1}_{44} & & & \\ & \text{\Huge 0} & & & G^{-1}_{55} & & \\ & & & & & G^{-1}_{66} & \\ & & & & & & G^{-1}_{77} \end{bmatrix}$$

$$G^{-1}_{11} = 3.0 \times 10^{-6} \quad G^{-1}_{22} = 2.0 \times 10^{-6} \quad G^{-1}_{33} = 3.0 \times 10^{-5} \quad G^{-1}_{44} = 3.0 \times 10^{-5}$$

$$G^{-1}_{55} = G^{-1}_{66} = \begin{cases} \left(\dfrac{15.0 \times 0.107}{p\beta}\right)^2 & \text{if} \quad p \le 1000 \text{ MeV/c} \\ 1.0 \times 10^{-5} & \text{if} \quad p > 1000 \text{ MeV/c} \end{cases}$$

Where: $p \equiv$ momentum of recoil proton

$$\beta = p/(p^2 + M^2)^{\frac{1}{2}}$$

$$G^{-1}_{77} = (a \cdot p)^2 \qquad a = \begin{cases} 0.05 & p \le 350 \text{ MeV/c} \\ 0.04 & 350 < p \le 400 \text{ MeV/c} \\ 0.03 & 400 < p \le 500 \text{ MeV/c} \\ 0.02 & p > 500 \text{ MeV/c} \end{cases}$$

FIG. 23--Error assignments for FIT. For low momentum protons, the errors in the proton variables are determined by Coulomb scattering.

VIII. CORRECTIONS TO THE DATA

A. Energy Dependence of Neutron Detection Efficiency

In order to insure that there was no energy-dependent bias introduced by the neutron detection method, it was necessary to investigate the detection efficiency in the following manner.

While the apparatus was set up to measure scattering in the diffraction peak region, the triggering system was altered: The neutron counters were removed from the coincidences, leaving the triggering requirement of $\overline{A1}\ \overline{A2}\ P1\ P2$. Therefore, all the chambers were pulsed whenever the system indicated that a charged particle had passed through the magnet. If one assumed that the event was elastic, the angle and momentum of the recoil proton were sufficient to determine all parameters – including the angle and momentum of the scattered neutron. This assumption is justified, as it had been found that in this small angle region, more than 85% of all triggers were elastic events. One then looked in the neutron chambers for a neutron interaction at the predicted angle.

Figure 24 shows the ratio of observed interactions to the total number expected versus the kinetic energy of the scattered neutron. This ratio represents the product of the efficiency of the chambers to "convert" neutrons to charged particles, and of the efficiency of the scanners to identify the interactions. At the higher neutron energies, the ratio is roughly flat and is approximately 55 to 60%, which is consistent with the total number of collision lengths represented by the chambers. There is a slight dip in the ratio around 2 GeV, which may possibly be due to a change in the neutron cross section on steel, a change in the multiplicity of prongs in the neutron stars and a corresponding scanner bias, an increase in inelastic contamination at this energy, or some

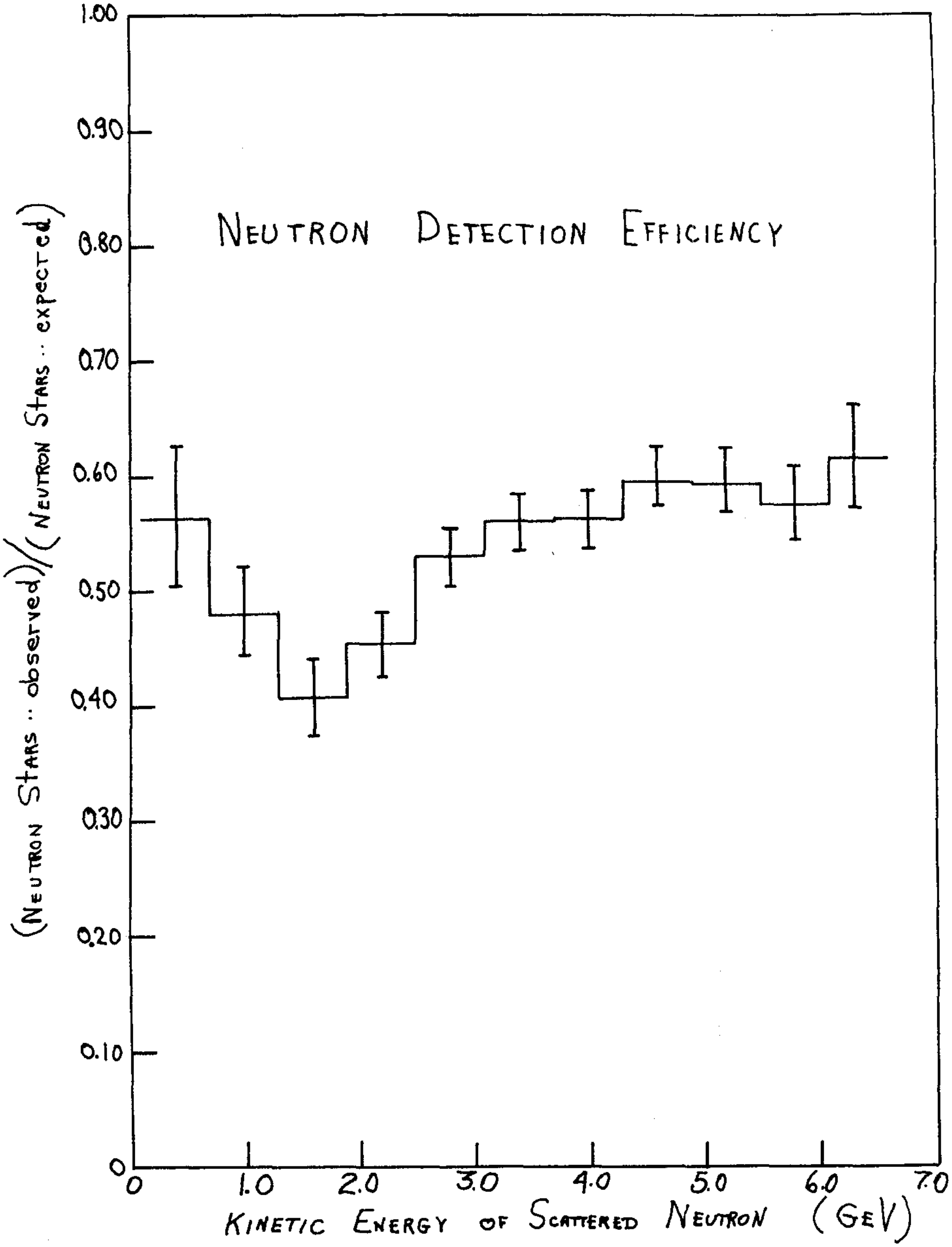

FIG. 24--Neutron detection efficiency as a function of the kinetic energy of the scattered neutron.

combination of these effects. Estimates of these effects have shown then to be too small to explain the dip at present. As the data presented represents approximately 20% of the data available in this mode, the reasons for the dip may become apparent as the rest of the data is analyzed.

B. Weighting Function

Because of the length of the target and the solid angle acceptances of the neutron and proton arms, the probability at a given setting of the arms for observing an elastic scattering involving a particular four-momentum transfer $|t|_i$ is a function of the incident neutron energy and the point of interaction in the target. This probability was calculated using Monte Carlo methods, and when cross sections were calculated, every elastic event was weighted according to this probability. Figure 25 shows a plot of two of the probability functions versus $|t|$ for two successive settings. Events that had less than a 40% chance of being seen were not included in the final sample of elastic events.

C. Target Empty

Evaluation was made of the contamination of the elastic sample from interactions not taking place in the hydrogen. Because of the care taken in constructing the target vessel, the number of "fake" elastic events present when running without hydrogen in the target--"target empty"--was found to be negligible.

D. Beam Contaminants

Because every elastic event was overdetermined, it was possible to test for the presence in the beam of contamination from particles other than neutrons which could fake n-p scattering. The method was to consider each event to be

$$X + p \rightarrow X + p \qquad (42)$$

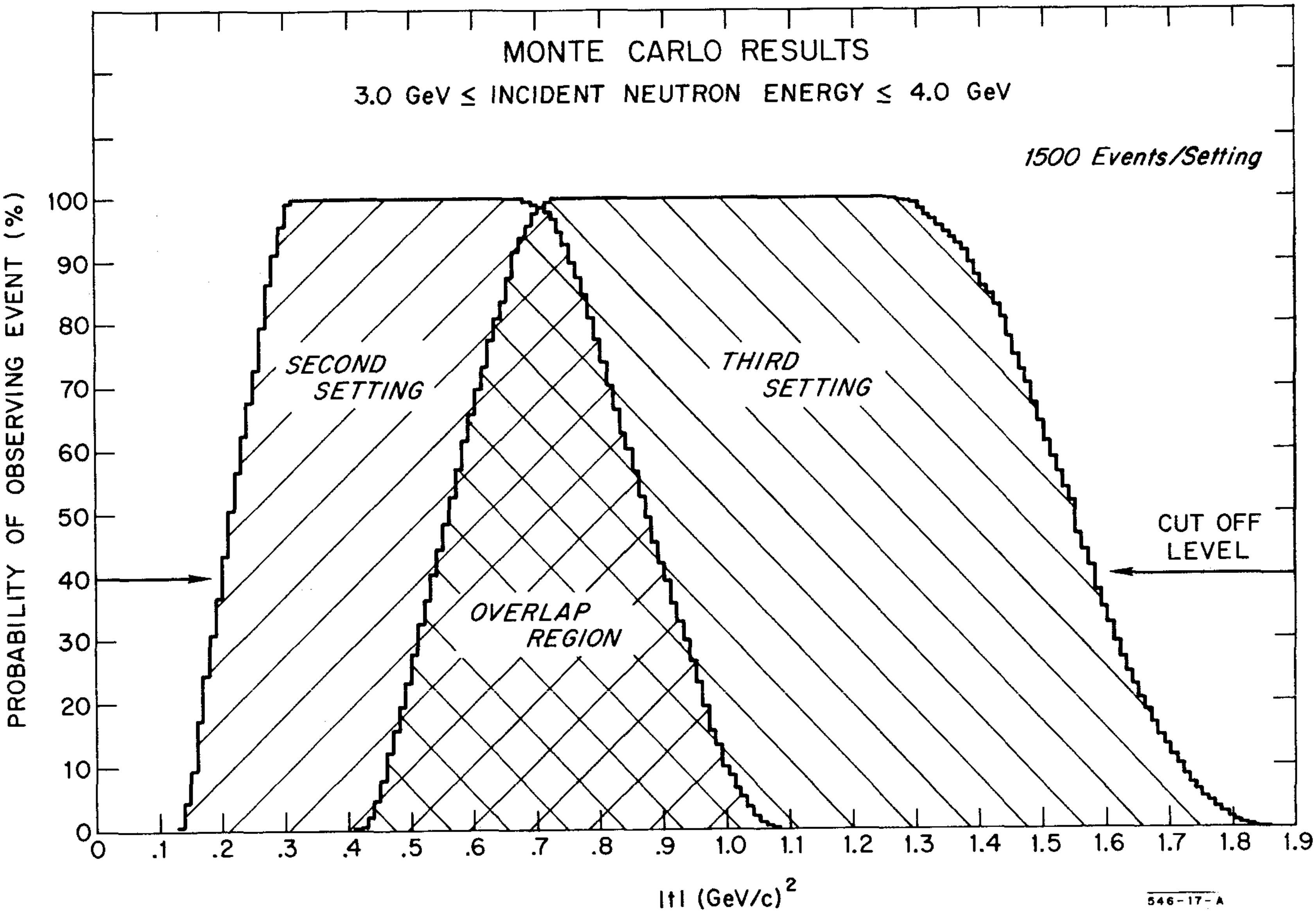

FIG. 25--Probability of observing an elastic scattering involving a particular four momentum transfer versus |t| for two successive settings of the apparatus. For each setting, 1500 "events" were used in the Monte Carlo calculation.

where the mass of the X-particle is unknown. The distribution of the mass of X for all measured frames shows a large peak at the neutron mass value and a fairly uniform background—presumably from inelastic events which shift the mass of the neutron when the reaction

$$n + p \rightarrow n + p + k\,\pi \; (k = 1, 2 \ldots) \tag{43}$$

is interpreted as the two-body reaction, Eq. (42). When one removes those events rejected by the elastic scattering fitting program, a clean neutron peak remains. Figure 26 shows the results of the calculation for a small portion of the data. The same kind of result was also obtained when the events were interpreted as

$$n + p \longrightarrow p + X \tag{44}$$

Again, the neutron peak is quite prominent, indicating that there were no very large contaminations present.

E. χ^2 Distribution

A more sensitive test for inelastic contaminations involves the distribution of χ^2. The distribution of χ^2 for a set of measurements subjected to a two-constraint fit is known[61, 62] to fall off steeply for large values χ^2. As mentioned before, if this set of measurements contains no background, then less than 2% of the measurements will have χ^2 greater than 8.0. Thus, the distribution of χ^2 for large χ^2 is primarily due to the presence of background. It can be shown[61, 62, 63] that when the background is randomly distributed a two-constraint fit produces a flat distribution of χ^2 for this background.

Assuming that there was no pathological behavior in our inelastic contamination, a background estimate was made using the distribution of χ^2 between 19 and 50. This calculation was done for small $|t|$ intervals over the entire

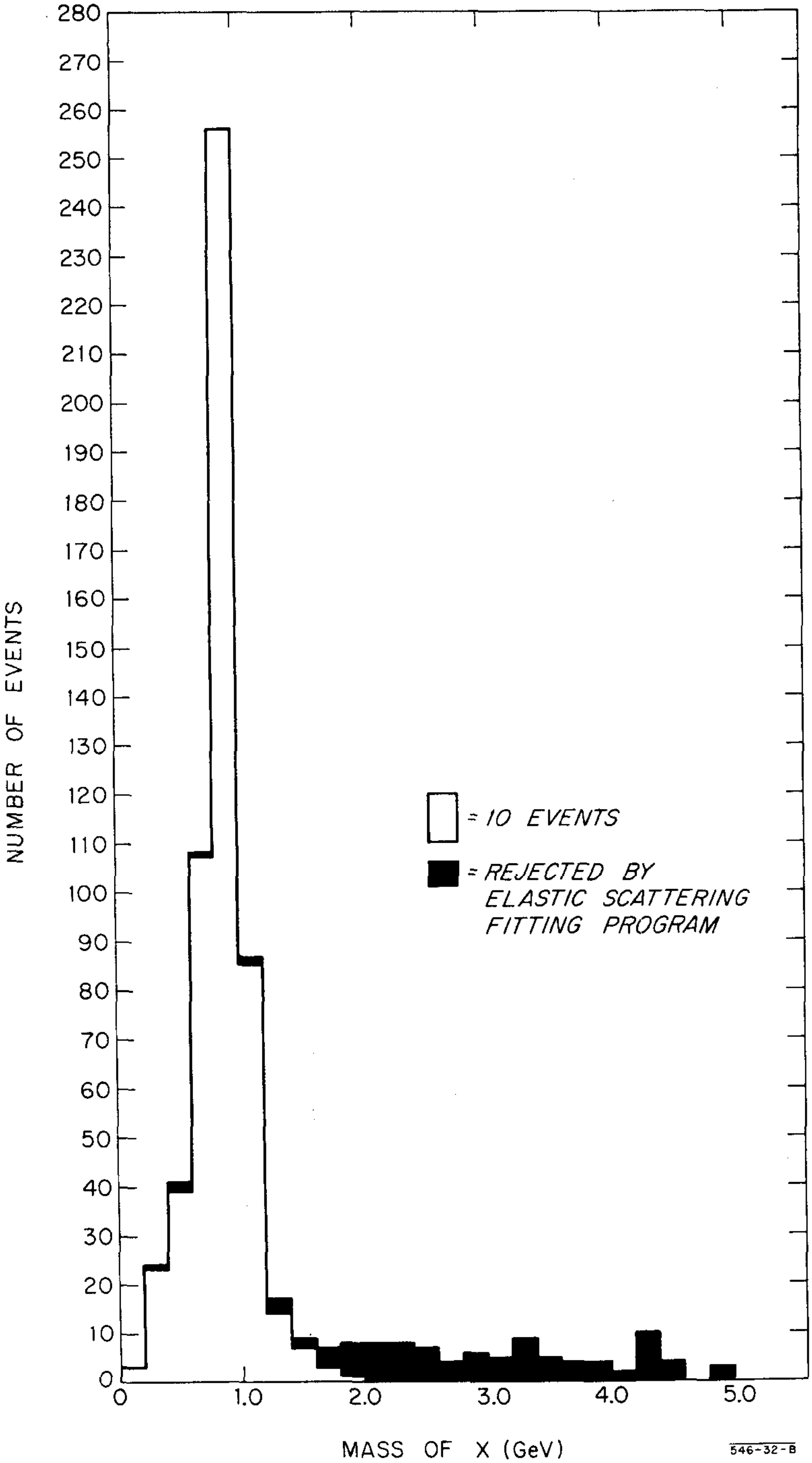

FIG. 26--Distribution of the mass of the X particle when the scatterings are interpreted as $X + p \rightarrow X + p$. A large peaking at the neutron mass is observed. Events rejected by FIT are indicated.

angular range covered by the experiment. It was found that the inelastic contamination was less than one percent at the smallest $|t|$ and only 10 ± 5 percent at the largest $|t|$. Corrections for these small backgrounds were made.

IX. PRESENTATION OF THE DATA

A. Neutron Spectrum

The shape of the energy distribution of the incident neutron beam shown in Fig. 27 was obtained from the analysis of the elastic events. The spectrum is seen to peak at high energies with the maximum around 5.0 GeV and with two-thirds of the observed neutrons having kinetic energies greater than 4.0 GeV. This high energy spectrum was, in fact, a more favorable one than had been anticipated. The neutron intensity, with the collimator system subtending approximately 3.87×10^{-6} sr at 1° with respect to the external proton beam, was roughly 1.5×10^{5} neutrons for 10^{10} protons in the external beam. This intensity represents the total number of neutrons in the energy range from 1 to 6.3 GeV.

It is interesting to see if this spectrum is consistent with production data for other elementary particles, in particular for proton production. The data for inelastic production of protons from beryllium have been examined,[64] and the information has been summarized in terms of an empirical fit valid for a large range of energies. The formula giving the number of protons of momentum p into a solid angle $d\Omega = \sin\theta \, d\theta \, d\phi$ is:

$$\frac{d^2N}{dp\,d\Omega} = p^2\left[1 + 0.47\,\frac{P_B}{p^2}\right]\left[\frac{0.56}{P_B} + \frac{0.44}{P_B^2}\,p\left(1 - \frac{0.47\,P_B}{p^2}\right)\right] e^{-3.0(p\theta)^2} \tag{45}$$

where P_B is the momentum of the incident beam. If the production of inelastic nucleons is relatively charge independent for small θ and large P_B, this formula may be applied to the neutron spectrum. It is reasonable to expect such charge independence, because in a nucleon-nucleon collision

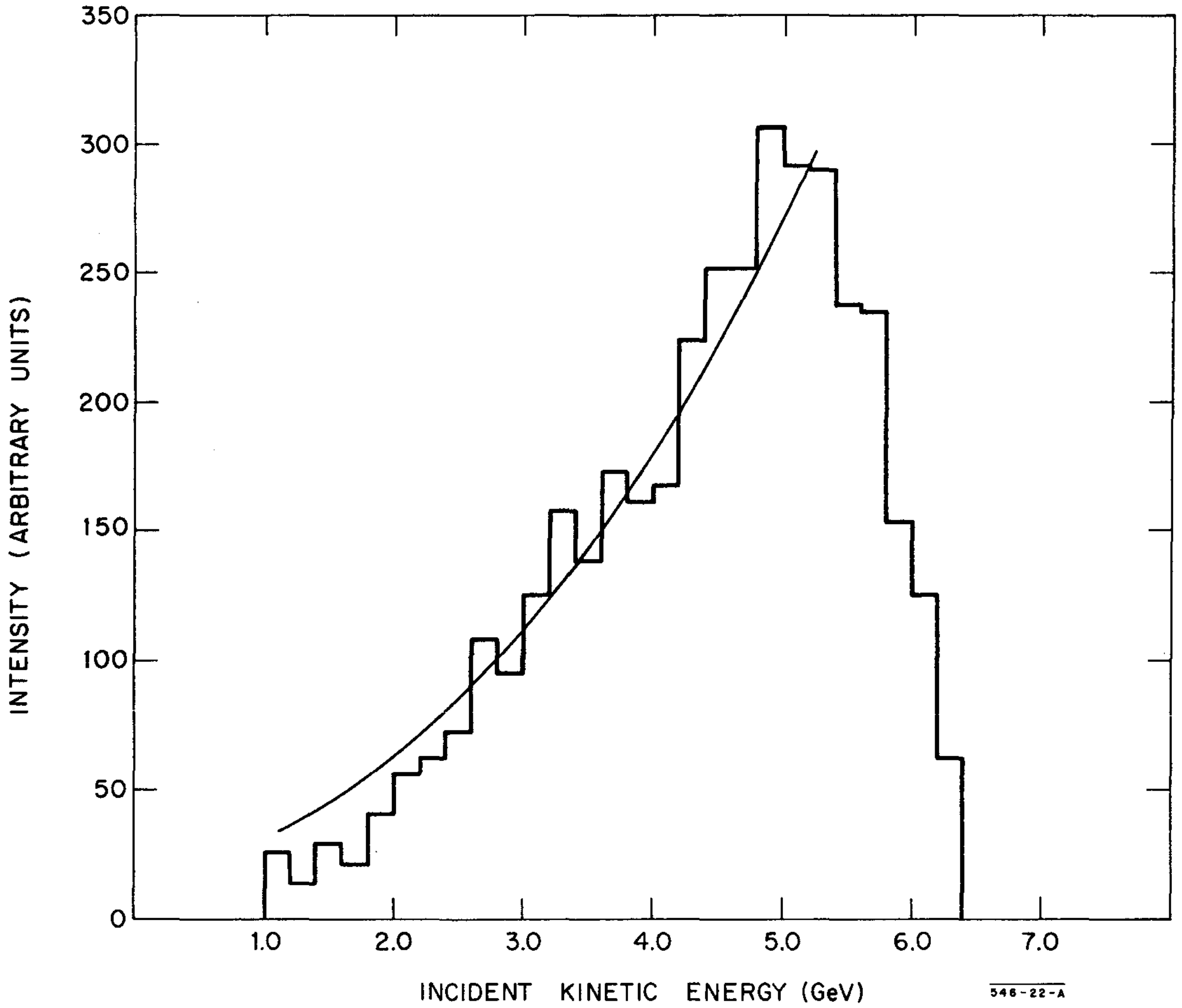

FIG. 27--Energy spectrum of neutron beam. The curve is an expression obtained for inelastic proton production [Eq. (45)].

accompanied by the emission of more than one pion, the inelastically produced nucleon is as likely to be a neutron as a proton. Also, because the production target is low Z, one does not expect nuclear effects to be important. As shown in Fig. 27, the expression (45) does seem to agree with the observed spectrum for energies up to about 5.5 GeV.

B. Normalizations

There are two questions of normalization involved in the presentation of the differential cross sections – relative and absolute.

As mentioned before, four sets of counter telescopes were used to monitor the incident beam, the G, H, B, and M counters (see Fig. 12). Since the rates in these counters are proportional to the incident neutron flux, they were used to provide the relative normalization between settings. Unfortunately, it was not possible to use the B and M counters for all settings. Approximately halfway through the run, movement of a large shielding block caused the position of the B counters to shift slightly, changing the counting rate. The counting rate in the M counters also varied, for when the magnet system was positioned to measure recoil protons with small lab angles, part of the magnet and its support carriage blocked the M counters. None of these troubles affected the G and H counting rates, which were found to be reproducible within statistics.

Another method was used to check this normalization. As shown in Fig. 25, the regions of the differential cross section measured by successive settings overlapped. Comparison of the cross sections in the overlap region measured at the two settings serves as a consistency check of the normalization. This method agrees with the normalizations attained from the G and H counters within the statistics presently available.

The experiment itself did not allow a measurement of the absolute normalization. However, this was obtained as follows: The expression (2) for the differential cross section can be written as

$$\frac{d\sigma}{d\Omega} = \left(\mathrm{Re}\, f(\theta)\right)^2 + \left(\mathcal{I}m\, f(\theta)\right)^2 \tag{46}$$

Considering the 0^o cross section and using the optical theorem (see Appendix), this becomes

$$\left.\frac{d\sigma}{d\Omega}\right|_{\theta=0^o} = \left(\frac{4\pi}{p}\,\sigma_{\text{total}}\right)^2 (1+\rho_n^2) \tag{47}$$

where

$$\rho_n = \frac{\mathrm{Re}\, f(0^o)}{\mathcal{I}m\, f(0^o)} \tag{48}$$

Equation (47) indicates that the absolute values of the differential cross section at 0^o depend upon total cross section measurements and on the value of ρ_n.

Note that the assumptions of the optical model which led to Eqs. (10a) and (10b) imply that ρ_n is zero. However, the predicted exponential behavior of the differential cross section is not affected if ρ_n is non-zero as long as the real part of the scattering amplitude is small and does not have any drastic $|t|$ dependence.

Measurements of the total neutron-proton cross section have been of two types – the direct method and the subtraction method. The few direct measurements[65, 66] are transmission experiments using neutron beams. The data, which have quoted errors ranging from 4 to 10 percent, unfortunately give the cross sections at only a few energies in the range of interest. The subtraction measurements,[67] however, cover the energy interval from 1 to 7 GeV in great detail. The analysis involves the comparison of the total cross sections for proton-proton and proton-deuteron scattering. It can be shown[67, 68, 69, 70] that the p-d cross section can be expressed in terms of the p-p and n-p cross sections as:

$$\sigma_{\text{total}}(\text{p-d}) = \sigma_{\text{total}}(\text{p-p}) + \sigma_{\text{total}}(\text{p-n}) - \sigma_{\text{total}}(\text{pp})\,\sigma_{\text{total}}(\text{pn})(1 - \rho_n \rho_p)\cdot F \qquad (49)$$

where ρ_p is the ratio of the real part to the imaginary part of the scattering amplitude for proton-proton scattering, and F is a factor depending on the deuteron form factor and the form factors for the imaginary amplitudes for np and pp scattering. Values of the neutron-proton total cross section can be obtained using Eq. (49)with accuracies from 2.5 to 5 percent, as the last factor in Eq. (49) is small and relatively insensitive to the actual value of ρ_n.

An experimental determination of ρ_n can be made using Eq. (49), and a direct measurement of $\sigma_{\text{total}}(\text{n-p})$[71, 72] or can be performed by using a formula equivalent to Eq. (49) which compares the small angle p-d and pp differential cross sections.[68] The data at energies near 20 GeV[68] indicate that ρ_n is approximately -0.33, but the data in the energy range from 1 to 6 GeV are consistent with the real part being zero. While calculations of ρ_n[73, 74] based on the present data and dispersion relations agree at very high energies, there are large differences in the 1 to 6 GeV region. Because this confusion exists and because the data is consistent with a vanishing ρ_n, the cross sections were normalized with the assumption that $\rho_n = 0$.

Because the neutron beam contained all energies of neutrons, the differential cross sections are presented in roughly 1-GeV intervals. Therefore, the calculation of the zero-degree cross sections for a given energy interval had to take the energy spectrum in the interval into consideration. The value at 0° was a weighted average of the 0° values for all energies in an interval, each value weighted according to the intensity of the observed neutron spectrum at that energy. The cross sections were then normalized by fitting the small angle region with an exponential in $|t|$ (see Eq. 10b), extrapolating to 0°, and using the 0° values given in Table II.

C. Differential Cross Sections

The neutron-proton elastic differential cross sections are shown in Figs. 28a-e in 1-GeV energy intervals as semi-logarithmic plots versus $|t|$, and the values of the cross section are given in Table III. The point corresponding to $\theta = 90^{\circ}$ is indicated on each plot. The values of $d\sigma/d\Omega$ given in Table III were calculated from the values of $d\sigma/d|t|$ using the weighted averages of p which are shown in Table IV for each incident energy range. This data is based on 6219 elastic events representing about 15% of the available data.

The cross sections cover a very wide range in $|t|$, going from 0.2 $(\mathrm{GeV/c})^2$ to 9.050 $(\mathrm{GeV/c})^2$. The magnitude of cross sections measured extends from 24 $\mathrm{mb/(GeV/c)}^2$ to 0.002 $\mathrm{mb/(GeV/c)}^2$, representing a drop of four orders of magnitude.

All of the cross sections have the following general characteristics. For values of $|t|$ less than 0.7 $(\mathrm{GeV/c})^2$, the behavior is roughly exponential, as had been expected. As $|t|$ increases past 1.0 $(\mathrm{GeV/c})^2$, the differential cross sections deviate from the exponential and begin to flatten out as $\theta = 90^{\circ}$ is approached. They are roughly flat in the region of 90°; the higher energy plots approach symmetry around 90°, with the minima in the cross sections at or just beyond 90°.

A detailed examination of the cross sections is made in the next section.

TABLE II

Values of Zero Degree Cross Sections

Incident Energy Range (GeV)	$d\sigma/d\|t\|$ at 0° $\left(\mathrm{mb}/(\mathrm{GeV}/c)^{2}\right)$
1.0 - 2.0	91.69
2.0 - 3.0	93.69
3.0 - 4.0	91.59
4.0 - 5.0	90.18
5.0 - 6.3	88.34

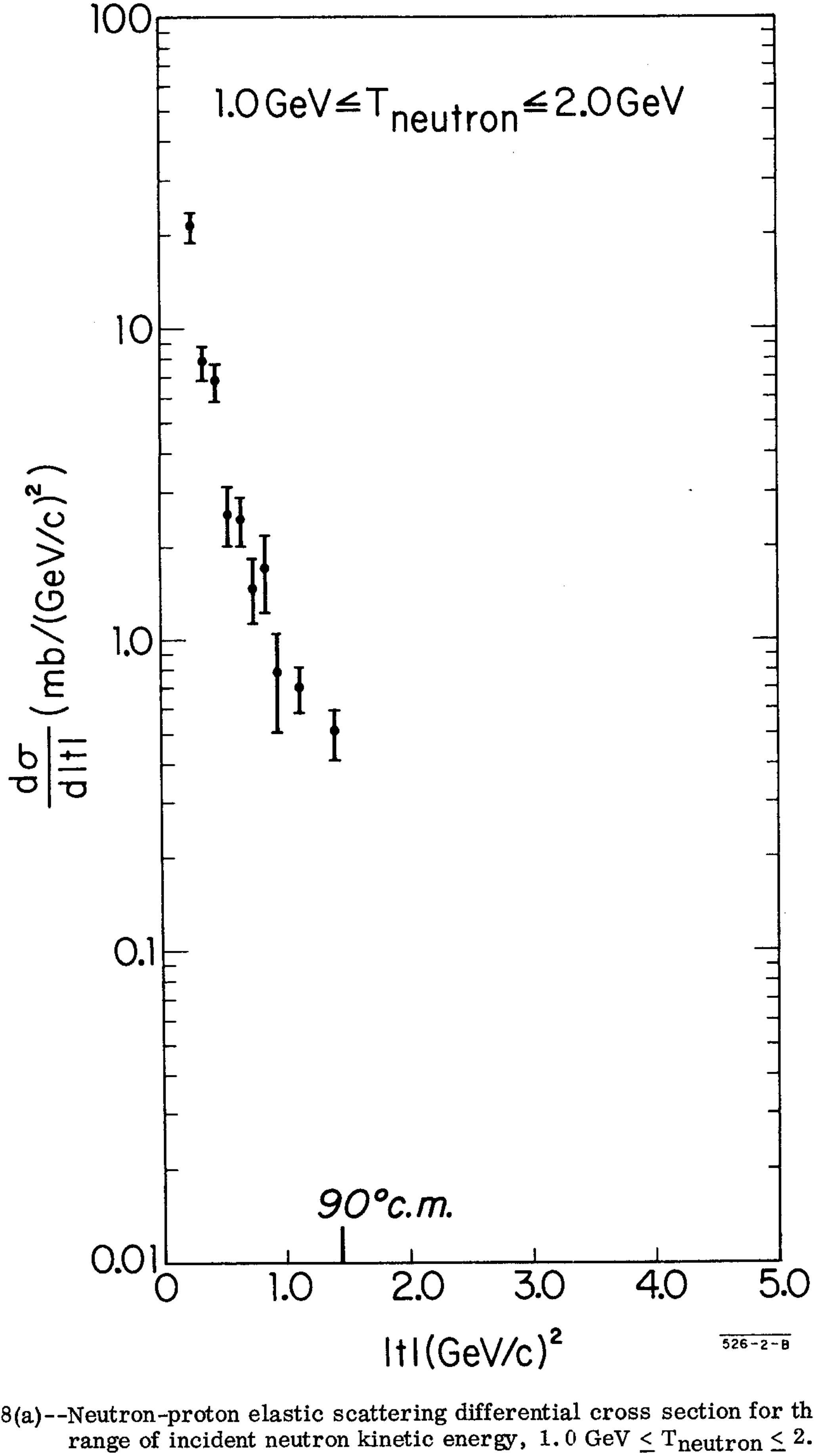

FIG. 28(a)--Neutron-proton elastic scattering differential cross section for the range of incident neutron kinetic energy, 1.0 GeV $\leq T_{neutron} \leq$ 2.0 GeV.

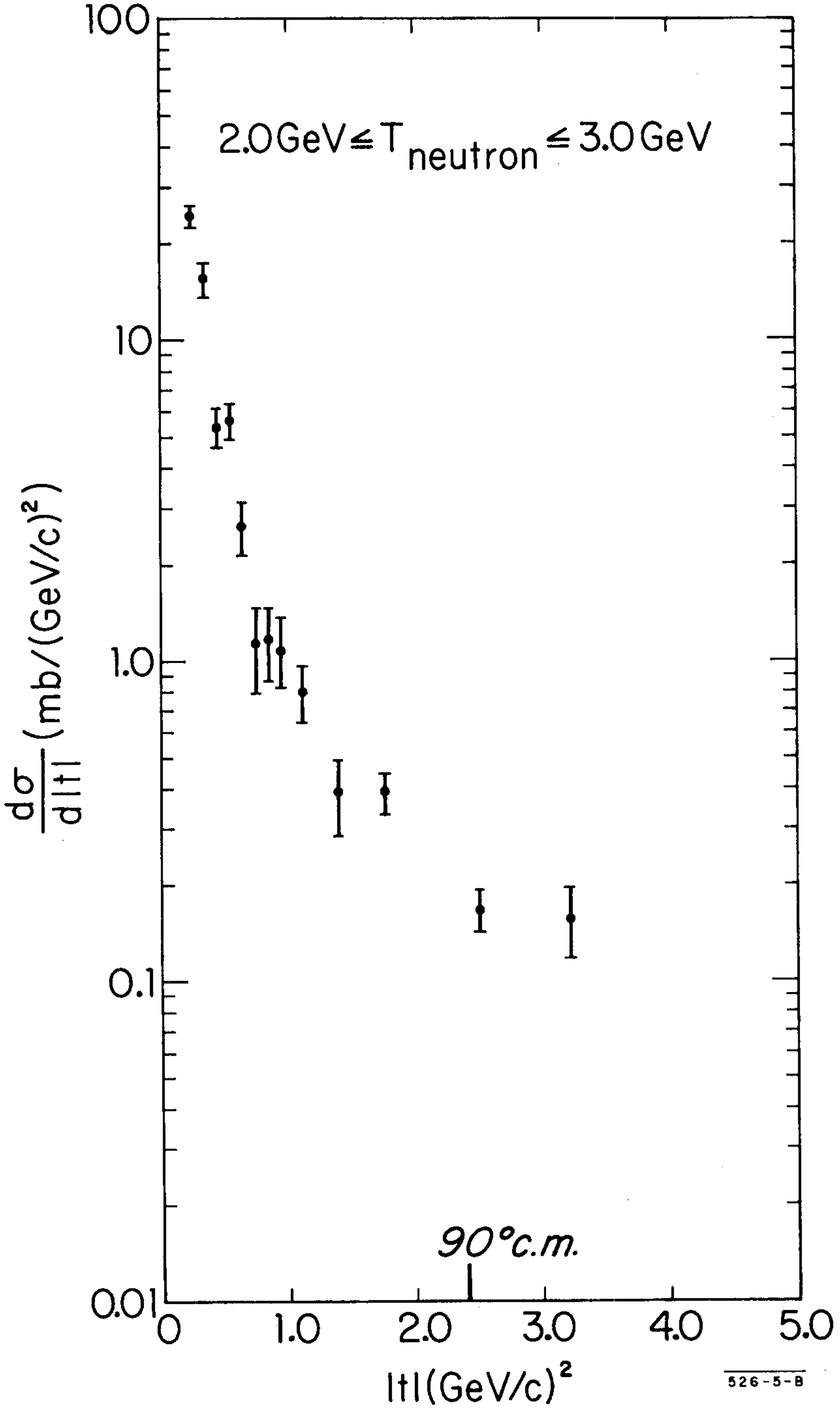

FIG. 28(b)--Neutron-proton elastic scattering differential cross sections for the range of incident neutron kinetic energy, 2.0 GeV $\leq T_{neutron} \leq$ 3.0 GeV.

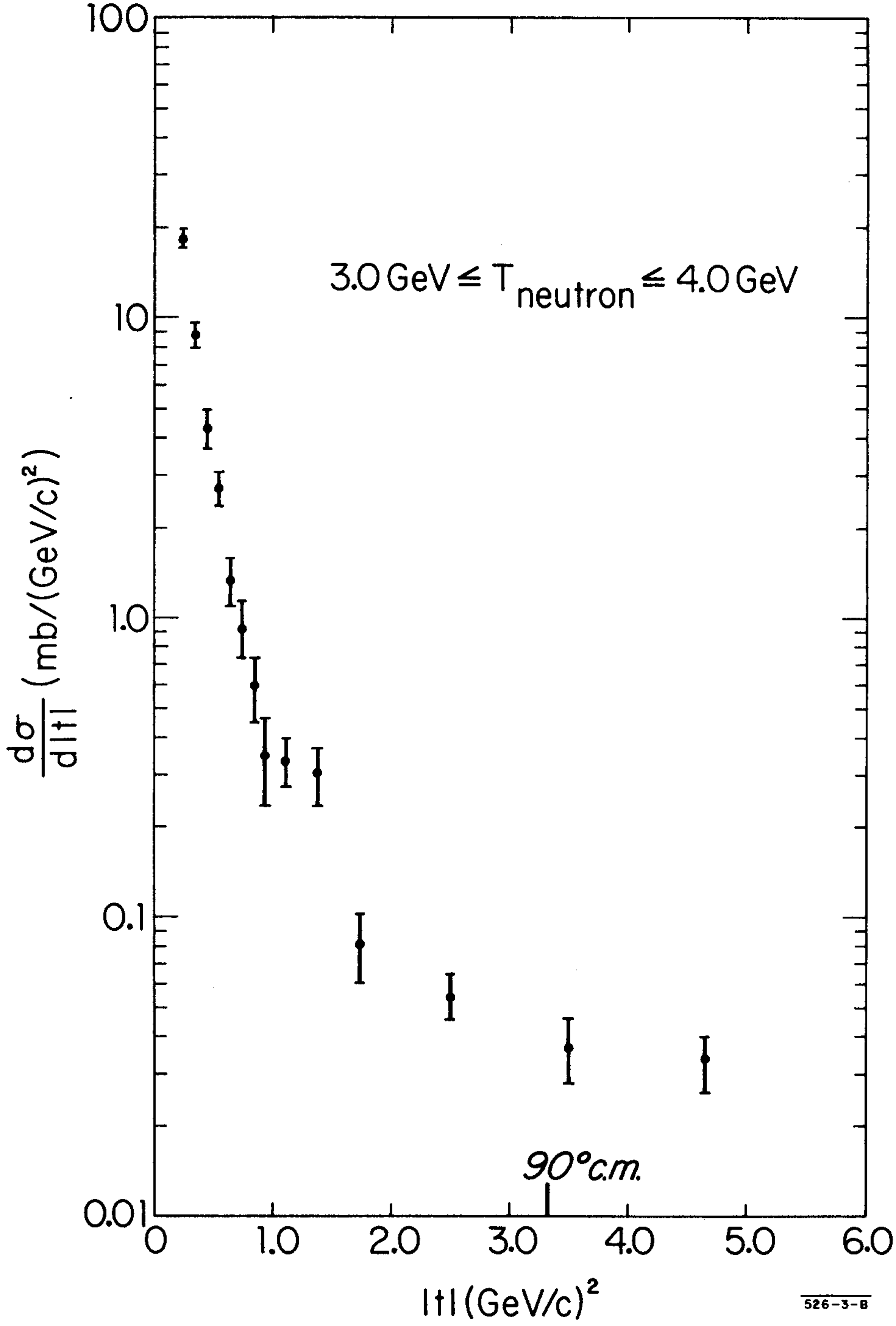

FIG. 28(c)--Neutron-proton elastic scattering differential cross section for the range of incident neutron kinetic energy, 3.0 GeV ≤ $T_{neutron}$ ≤ 4.0 GeV.

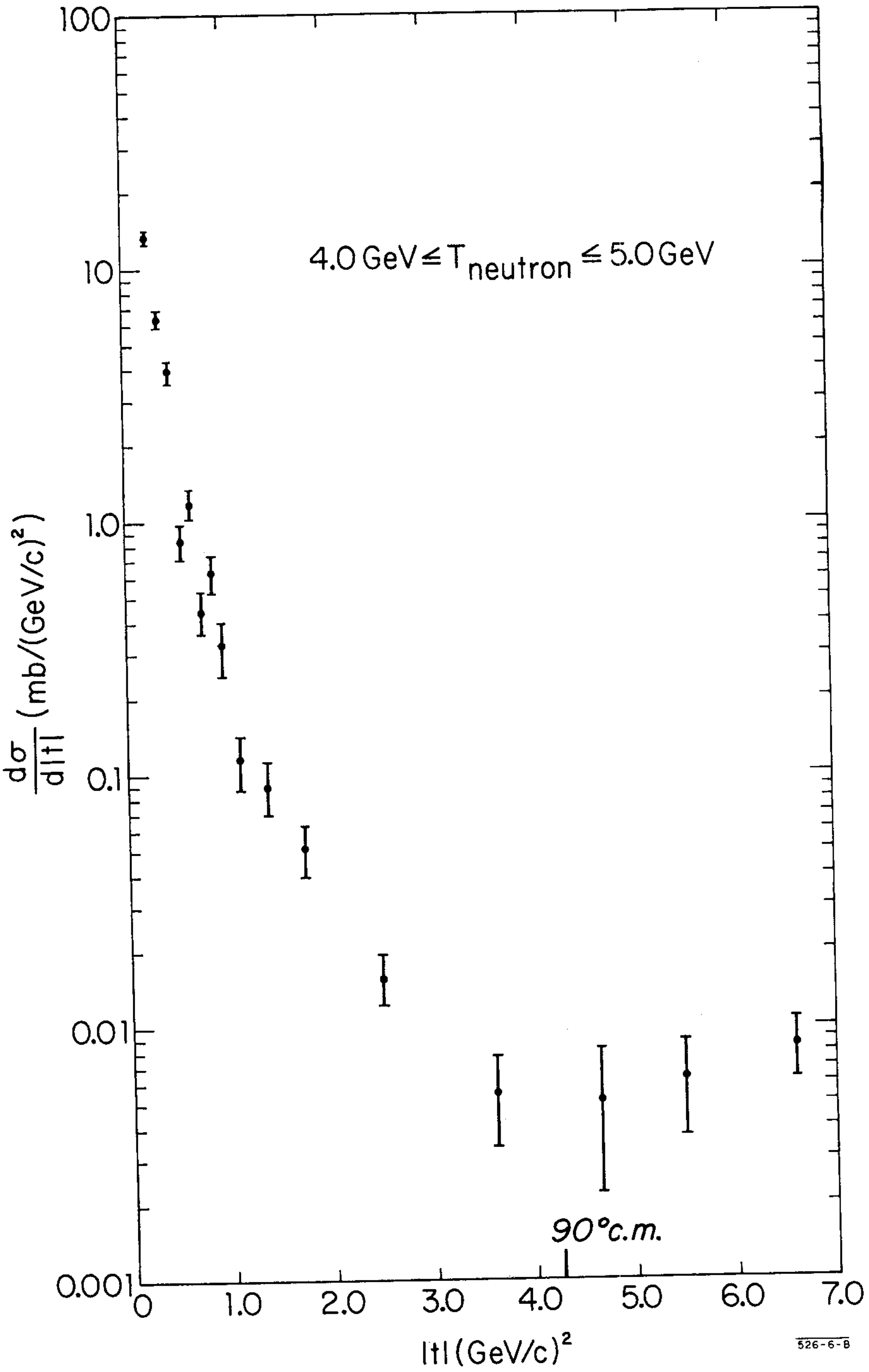

FIG. 28(d)--Neutron-proton elastic scattering differential cross sections for the range of incident neutron kinetic energy, 4.0 GeV $\leq T_{neutron} \leq$ 5.0 GeV.

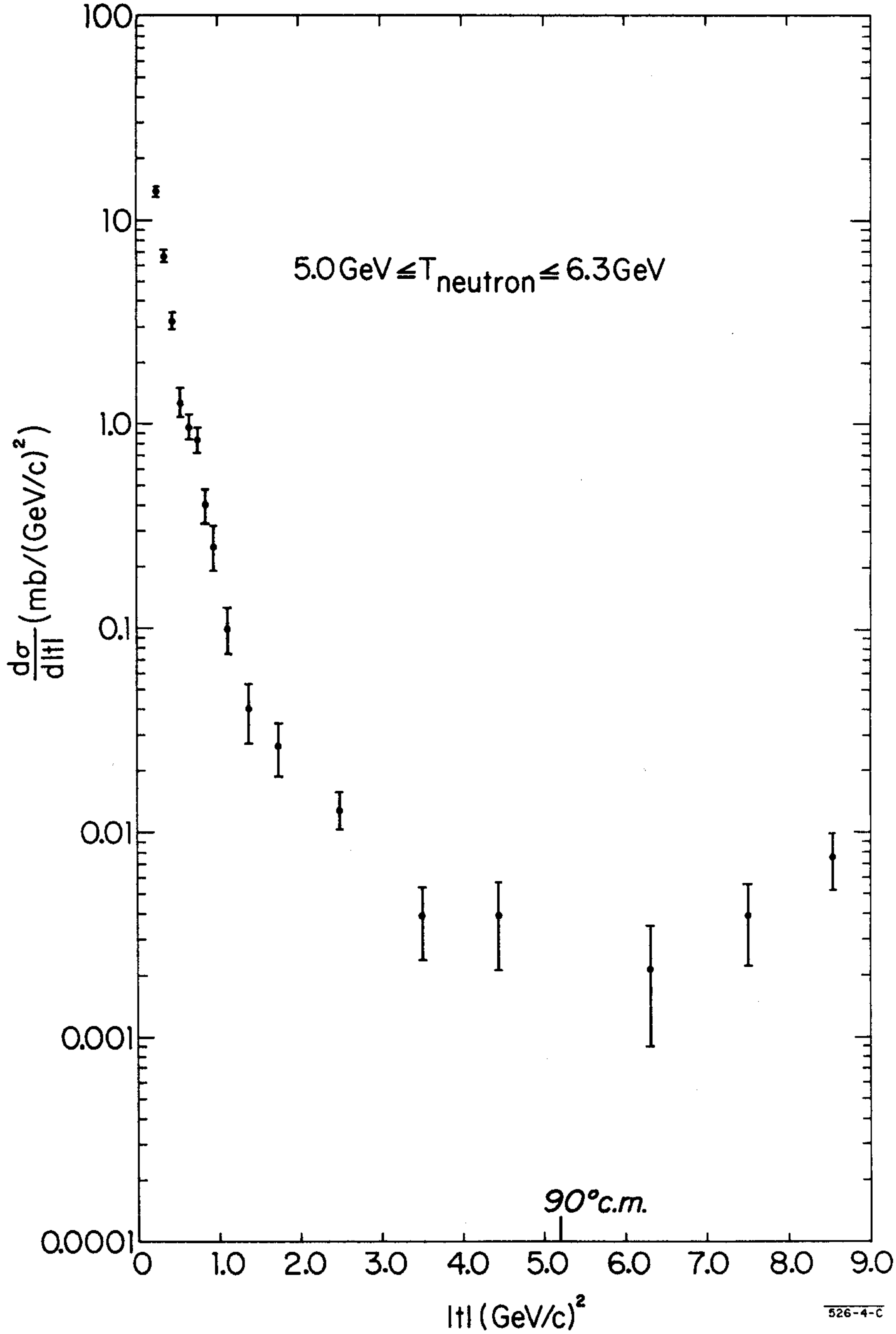

FIG. 28(e)--Neutron-proton elastic scattering differential cross section for the range of incident neutron kinetic energy, 5.0 GeV ≤ $T_{neutron}$ ≤ 6.3 GeV.

TABLE III

Neutron-Proton Elastic Scattering Differential Cross Sections

|t| Range $(GeV/c)^2$	|t| Central $(GeV/c)^2$	$\frac{d\sigma}{d\|t\|}$ $\left(mb/(GeV/c)^2\right)$	$\cos\theta$	$\frac{d\sigma}{d\Omega}$ (mb/sr)
		1.0 GeV ≤ T neutron ≤ 2.0 GeV [782 events]		
0.200 - 0.300	0.250	21.254 ± 2.201	0.827	4.902 ± 0.508
0.300 - 0.400	0.350	7.864 ± 0.960	0.758	1.814 ± 0.221
0.400 - 0.500	0.450	6.866 ± 0.879	0.689	1.583 ± 0.203
0.500 - 0.600	0.550	2.579 ± 0.559	0.620	0.595 ± 0.129
0.600 - 0.700	0.650	2.457 ± 0.431	0.551	0.567 ± 0.099
0.700 - 0.800	0.750	1.497 ± 0.340	0.482	0.345 ± 0.079
0.800 - 0.900	0.850	1.720 ± 0.479	0.413	0.397 ± 0.110
0.900 - 1.000	0.950	0.781 ± 0.267	0.344	0.180 ± 0.062
1.000 - 1.250	1.125	0.701 ± 0.115	0.224	0.162 ± 0.027
1.250 - 1.550	1.400	0.506 ± 0.090	0.034	0.117 ± 0.021
		2.0 GeV ≤ T neutron ≤ 3.0 GeV [992 events]		
0.200 - 0.300	0.250	24.398 ± 1.855	0.896	9.323 ± 0.709
0.300 - 0.400	0.350	15.562 ± 1.803	0.854	5.947 ± 0.689
0.400 - 0.500	0.450	5.360 ± 0.712	0.812	2.048 ± 0.272
0.500 - 0.600	0.550	5.660 ± 0.737	0.771	2.163 ± 0.282
0.600 - 0.700	0.650	2.633 ± 0.481	0.729	1.006 ± 0.184
0.700 - 0.800	0.750	1.138 ± 0.345	0.688	0.435 ± 0.132
0.800 - 0.900	0.850	1.181 ± 0.303	0.646	0.451 ± 0.116
0.900 - 1.000	0.950	1.086 ± 0.257	0.604	0.415 ± 0.098
1.000 - 1.250	1.125	0.800 ± 0.153	0.531	0.306 ± 0.058
1.250 - 1.500	1.375	0.391 ± 0.103	0.428	0.149 ± 0.040
1.500 - 2.000	1.750	0.391 ± 0.056	0.271	0.150 ± 0.022
2.000 - 3.000	2.500	0.167 ± 0.024	-0.041	0.064 ± 0.009
3.000 - 3.430	3.215	0.157 ± 0.038	-0.339	0.060 ± 0.015
		3.0 GeV ≤ T neutron ≤ 4.0 GeV [1154 events]		
0.200 - 0.300	0.250	18.399 ± 1.105	0.926	9.699 ± 0.582
0.300 - 0.400	0.350	8.762 ± 0.796	0.894	4.619 ± 0.420
0.400 - 0.500	0.450	4.289 ± 0.606	0.864	2.261 ± 0.319
0.500 - 0.600	0.550	2.694 ± 0.354	0.834	1.420 ± 0.187
0.600 - 0.700	0.650	1.315 ± 0.230	0.804	0.693 ± 0.121
0.700 - 0.800	0.750	0.918 ± 0.183	0.774	0.484 ± 0.096
0.800 - 0.900	0.850	0.588 ± 0.143	0.743	0.310 ± 0.075
0.900 - 1.000	0.950	0.345 ± 0.109	0.713	0.182 ± 0.058
1.000 - 1.250	1.125	0.332 ± 0.061	0.660	0.175 ± 0.032
1.250 - 1.500	1.375	0.307 ± 0.060	0.585	0.162 ± 0.032
1.500 - 2.000	1.750	0.081 ± 0.020	0.472	0.043 ± 0.011
2.000 - 3.000	2.500	0.055 ± 0.009	0.245	0.029 ± 0.005
3.000 - 4.000	3.500	0.037 ± 0.009	-0.057	0.019 ± 0.005
4.000 - 5.300	4.650	0.033 ± 0.007	-0.404	0.018 ± 0.004

(continued)

TABLE III (Cont.)

$\|t\|$ Range $(\mathrm{GeV}/c)^2$	$\|t\|$ Central $(\mathrm{GeV}/c)^2$	$\frac{d\sigma}{d\|t\|}\left(\mathrm{mb}/(\mathrm{GeV}/c)^2\right)$	$\cos\theta$	$\frac{d\sigma}{d\Omega}$ (mb/sr)
		4.0 GeV $\leq$ T neutron $\leq$ 5.0 GeV [1548 events]		
0.200 - 0.300	0.250	13.402 ± 0.670	0.941	9.090 ± 0.454
0.300 - 0.400	0.350	6.386 ± 0.422	0.918	4.332 ± 0.286
0.400 - 0.500	0.450	3.956 ± 0.407	0.894	2.683 ± 0.276
0.500 - 0.600	0.550	0.844 ± 0.133	0.871	0.573 ± 0.090
0.600 - 0.700	0.650	1.196 ± 0.163	0.847	0.811 ± 0.111
0.700 - 0.800	0.750	0.446 ± 0.085	0.824	0.303 ± 0.058
0.800 - 0.900	0.850	0.632 ± 0.105	0.801	0.429 ± 0.071
0.900 - 1.000	0.950	0.326 ± 0.081	0.777	0.221 ± 0.055
1.000 - 1.250	1.125	0.114 ± 0.027	0.736	0.078 ± 0.019
1.250 - 1.500	1.375	0.090 ± 0.021	0.677	0.061 ± 0.014
1.500 - 2.000	1.750	0.051 ± 0.011	0.589	0.035 ± 0.008
2.000 - 3.000	2.500	0.016 ± 0.003	0.413	0.011 ± 0.002
3.000 - 4.250	3.625	0.006 ± 0.002	0.149	0.004 + 0.001
4.320 - 5.000	4.660	0.005 ± 0.003	-0.093	0.004 ± 0.002
5.000 - 6.000	5.500	0.006 ± 0.003	-0.291	0.004 ± 0.002
6.000 - 7.180	6.590	0.008 ± 0.002	-0.546	0.006 ± 0.001
		5.0 GeV $\leq$ T neutron $\leq$ 6.3 GeV [1743 events]		
0.200 - 0.300	0.250	13.872 ± 0.636	0.952	11.472 ± 0.526
0.300 - 0.400	0.350	6.639 ± 0.397	0.933	5.491 ± 0.328
0.400 - 0.500	0.450	3.237 ± 0.317	0.913	2.677 ± 0.262
0.500 - 0.600	0.550	1.298 ± 0.202	0.894	1.073 ± 0.167
0.600 - 0.700	0.650	0.975 ± 0.136	0.875	0.806 ± 0.113
0.700 - 0.800	0.750	0.842 ± 0.116	0.856	0.696 ± 0.096
0.800 - 0.900	0.850	0.402 ± 0.074	0.836	0.333 ± 0.061
0.900 - 1.000	0.950	0.252 ± 0.062	0.817	0.209 ± 0.051
1.000 - 1.250	1.125	0.100 ± 0.025	0.784	0.083 ± 0.021
1.250 - 1.500	1.375	0.040 ± 0.013	0.735	0.033 ± 0.011
1.500 - 2.000	1.750	0.027 ± 0.008	0.663	0.022 ± 0.006
2.000 - 3.000	2.500	0.013 ± 0.003	0.519	0.011 ± 0.002
3.000 - 4.000	3.500	0.004 ± 0.001	0.326	0.003 ± 0.001
4.000 - 4.860	4.430	0.004 ± 0.002	0.147	0.003 ± 0.002
5.640 - 7.000	6.320	0.002 ± 0.001	-0.216	0.002 ± 0.001
7.000 - 8.000	7.500	0.004 ± 0.002	-0.443	0.003 ± 0.001
8.000 - 9.050	8.525	0.008 ± 0.002	-0.641	0.006 ± 0.002

TABLE IV

Slopes of the Diffraction Peak for Neutron-Proton Scattering

Incident Kinetic Energy Range (GeV)	P Average (Momentum in Center-Of-Mass) (GeV/c)	b $(GeV/c)^{-2}$	R (fermis)
1.0 - 2.0	0.851	-6.321 ± 0.647	0.992 ± 0.051
2.0 - 3.0	1.096	-5.527 ± 0.463	0.928 ± 0.039
3.0 - 4.0	1.287	-6.655 ± 0.432	1.018 ± 0.033
4.0 - 5.0	1.460	-7.720 ± 0.411	1.097 ± 0.029
5.0 - 6.3	1.612	-7.562 ± 0.391	1.085 ± 0.028

X. COMPARISON WITH MODELS

A. Small Angle Region

As mentioned before, the small angle region of the differential cross section, $0.2(\mathrm{GeV}/c)^2 \leq |t| \leq 0/6\,(\mathrm{GeV}/c)^2$, was fit with an exponential of the form

$$\frac{d\sigma}{d|t|} = \left.\frac{d\sigma}{d|t|}\right|_{\theta=0^0} e^{b|t|} \tag{50}$$

The values of the parameter b for each energy interval as well as the values of the effective radius of interaction

$$R = 2\sqrt{-b} \tag{51}$$

are given in Table IV.

These values can be compared to those obtained from proton-proton scattering. According to recent data from Clyde et al.,[75] the values of -b for p-p scattering at 2.2, 4.1, and 6.2 GeV are 6.50 ± 0.03, 7.44 ± 0.04 and $7.69 \pm 0.04\,(\mathrm{GeV}/c)^{-2}$, respectively. The n-p and p-p values are quite similar except perhaps at the lowest energies, which implies that the radii of interaction are also quite similar.

The n-p system indicates a shrinkage of the diffraction peak with increasing energy. This can be seen from the values of the slope of the peak or in the following manner. From Eq. (11),

$$\frac{d\sigma}{d|t|} = \left|g(|t|)\right|^2 s^{2\alpha(|t|)-2} \tag{52}$$

Therefore,

$$\ln\left(\frac{d\sigma}{d|t|}\right) = \ln\left(g(|t|)^2\right) + \left[(2\alpha(|t|)-2)\right]\ln s \tag{53}$$

Using Eq. (53), and the values of the cross sections for $|t| = 0.250$ and $0.350\ (\mathrm{GeV/c})^2$ for energies between 2 and 6.3 GeV, the value of $\alpha(|t|)$ is found to be

$$\alpha(|t|) = (0.89 \pm 0.40) - (1.75 \pm 1.38)\,|t| \tag{54a}$$

If $\alpha(|t|)$ is required to be 1 at $|t| = 0$, then we find

$$\alpha(|t|) = 1.0 - (2.14 \pm 0.40)\,|t| \tag{54b}$$

Recent p-p values in this energy range are as follows: Using p-p cross sections measured at 2.2, 4.12, and 6.1 GeV,[75] we calculate that

$$\alpha(|t|) = (0.827 \pm 0.028) - (0.839 \pm 0.117)\,|t| \tag{55a}$$

At incident energies of 1.35, 2.1, and 2.9 GeV,[76] it was shown that

$$\alpha(|t|) = 1.0 - (2.58 \pm 0.36)\,|t| \tag{55b}$$

In the latter value, $\alpha(|t|)$ at $|t| = 0$ was required to be 1.

Thus the "shrinkage score" is now: three shrink, two expand, and two stay the same.

B. Intermediate Angles

In the region around $1.0\ (\mathrm{GeV/c})^2$, the cross sections in general deviate from the exponential in a smooth manner. Although not statistically significant, there are some ambiguous indications of structure in this region. This is most obvious for the energy range of 3 to 4 GeV. When the remainder of the data is analyzed, it should be possible to resolve the question of whether this is due to statistical fluctuations, relative normalization problems, or real structure. For the present, however, the data is consistent with no statistically significant second peak in the n-p system.

C. Large Angle Region

Figure 29 shows a composite of the n-p cross sections, the p-p cross sections, and some of the charge exchange measurements. The first observation to be made is that it appears as though the differential cross sections begin to increase past $\theta = 90^{\circ}$ even though the values of $|t|$ are very large. This may be interpreted as an indication that $|t|$ is not the meaningful parameter to describe the interaction. Past 90°, the reaction may consist of the neutron and proton exchanging their charges, and the momentum transfer of interest may be from the incident neutron to the recoil proton. In terms of $|t|$, this momentum transfer, u, is

$$|u| = 4p^2 - |t|$$

and as θ approaches 180°, $|u|$ decreases.

It can also be seen on Fig. 29 that the large angle measurements should increase smoothly into the charge exchange peak. However, in the regions past 90°, the slope of the differential cross section

$$d\left[\ell n\left(d\sigma/d|u|\right)\right]/d|u|$$

is about $0.6\,(\mathrm{GeV}/c)^{-2}$ compared with 4 to 5 $(\mathrm{GeV}/c)^{-2}$ near $\theta = 160^{\circ}$ and 40 or $50(\mathrm{GeV}/c)^{-2}$ near $\theta = 180^{\circ}$. These large changes in the slopes, when interpreted in terms of radii of interaction, suggest that n-p large angle scattering may involve the participation of three different regions in the scattering process, each region producing diffraction scattering with a different slope.

The similarity of the p-p and n-p systems for $\theta < 90^{\circ}$ implies that the Krisch[34] model may be applied to the n-p system. However, it is difficult to see a simple method of extending this model to include backward scattering, as this region seems to involve contributions from either three different exponentials or from some other mechanism.

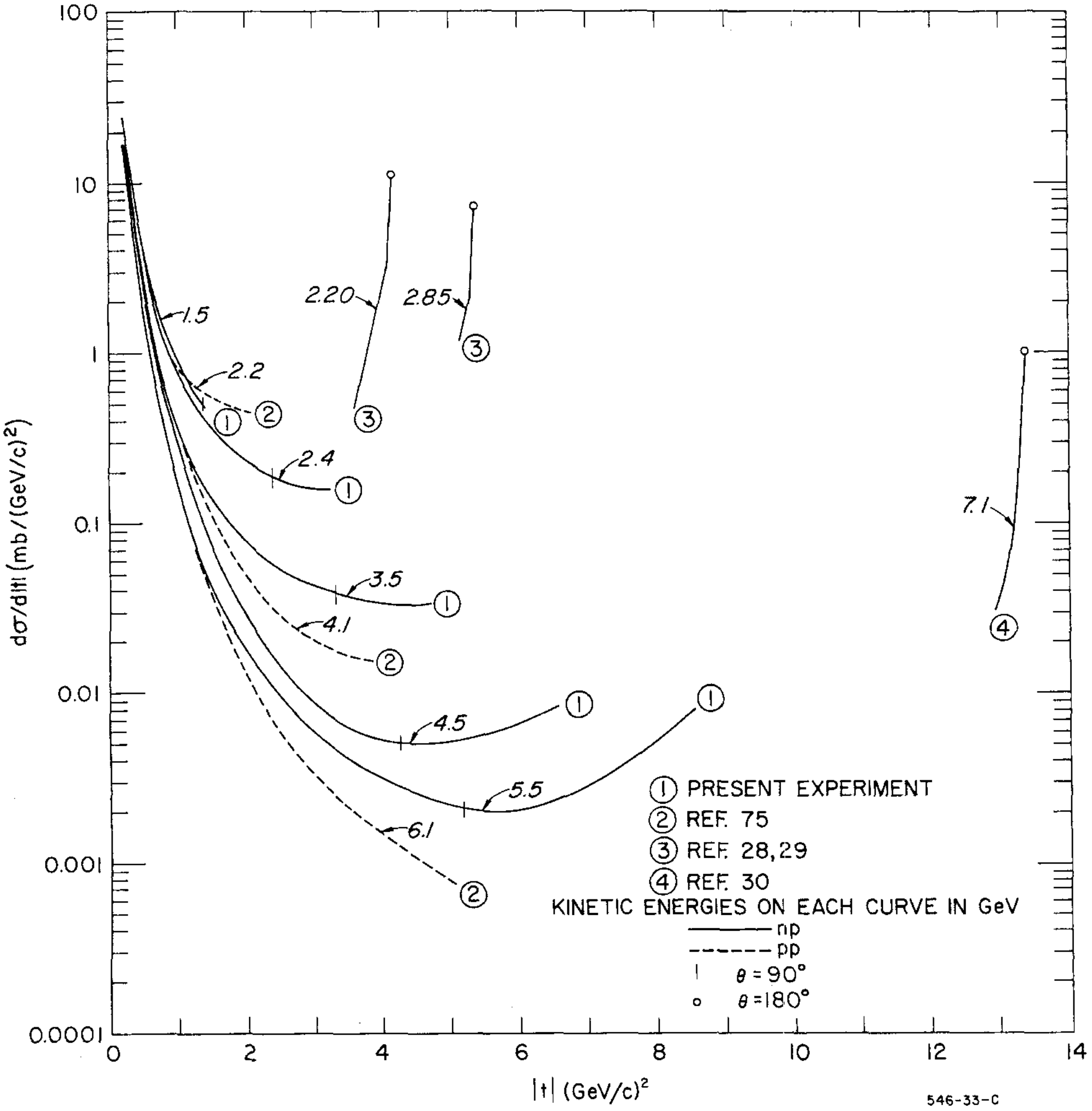

FIG. 29--Composite of n-p cross sections, p-p cross sections, and n-p charge exchange cross sections. The n-p cross sections represent smooth cruves hand-fitted to the data (Fig. 28).

A comparison of the data with the predictions of the statistical model was made by plotting the values of the differential cross section at 90° against $W^* = \sqrt{s}$ (Fig. 30). As shown in Eq. (13), this model predicts an exponential decrease of the cross section W^* of the form

$$(d\sigma/d\Omega)_{90^o} = A \exp(-gW^*)$$

A weighted least-square fit to the data yields

$$g = 3.73 \pm 0.38 \text{ GeV}^{-1} \tag{56}$$

which is not very different from the p-p value [Eq. (21)]. This exponential fall-off can also be interpreted, using Cocconi's thermodynamic model, in terms of the "temperature" of the system

$$T = 1.9 \pm 0.2 \; m_\pi \tag{57}$$

which is only slightly lower than that of the p-p system.

The 90° data was also fit with a power of W^*, namely

$$(d\sigma/d\Omega)_{90^o} = CW^{*-N}$$

N was found to be 11.04 ± 1.15. Since $|t|$ is approximately proportional to W^{*2}, this implies that the cross section drops off roughly as the inverse of $|t|$ to the 5.5 ± 0.5 power. This seems to agree with Serber's prediction of a $1/|t|^6$ law.

In order to compare the cross sections at 90° with the proton-proton values, the exponential fit was used to extrapolate the n-p values to the energies of the most recent p-p data. The comparison of the cross sections is shown in Table V. As can be seen, the 90° cross sections for the two systems agree within errors. This can be explained by the assumption that at high energies and large angles, the scattering amplitudes do not have very strong spin or

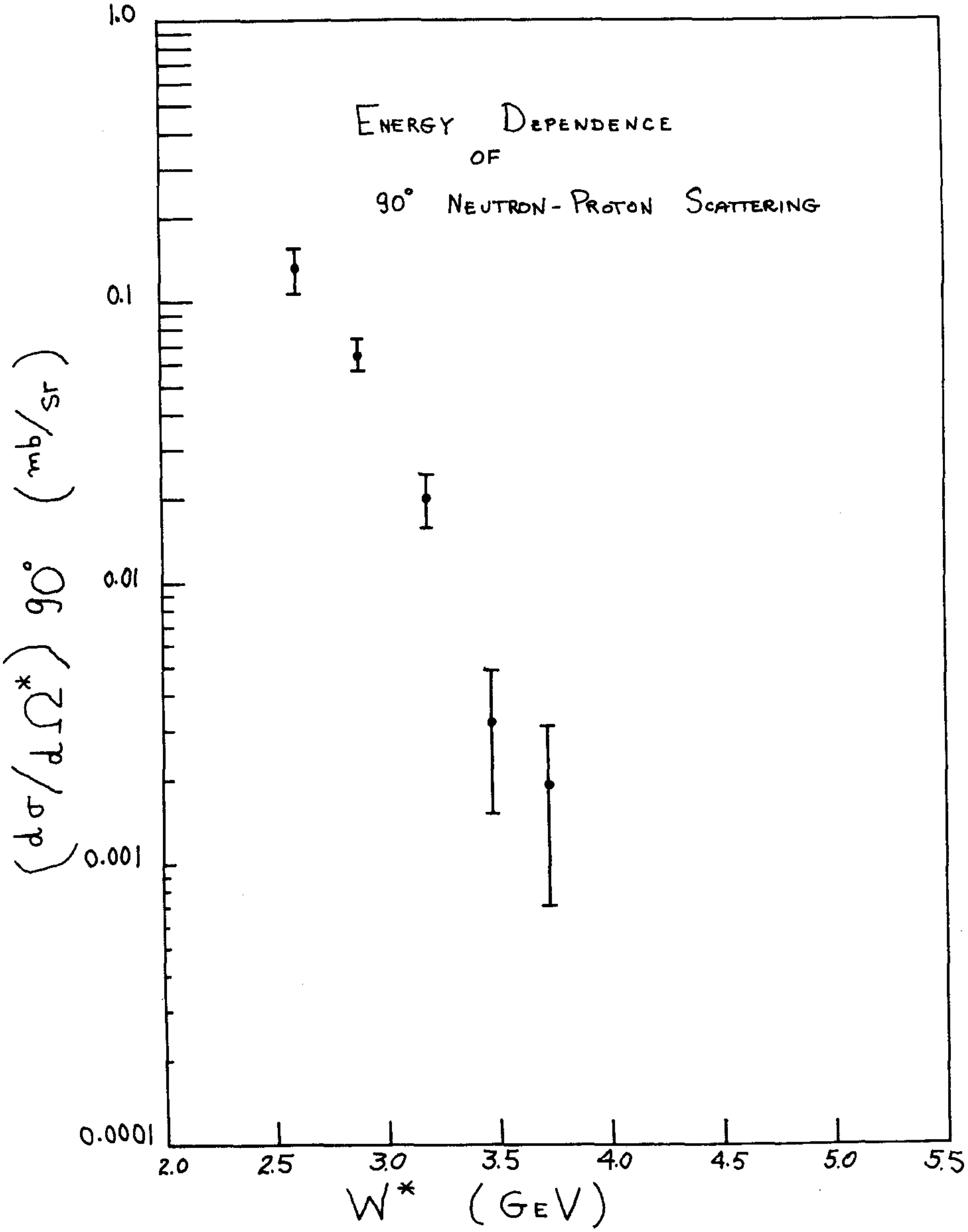

FIG. 30--Energy dependence of 90° n-p cross sections.

TABLE V

Comparison of 90° np and pp Cross Sections

	$(d\sigma/d\lvert t\rvert)90^{\circ}$ $(\mathrm{mb}/\mathrm{GeV}/c)^2$	
Incident Energy (GeV)	np (interpolated)	pp*
2.2	0.32 ± 0.05	0.45 ± 0.01
4.1	0.017 ± 0.006	0.016 ± 0.0009
6.2	0.0014 ± 0.0008	0.00078 ± 0.00004**

*From Reference 75

**pp value at 86.3°

isotopic spin dependence,

$$A(I = 0, S = 1) \approx A(I = 1, S = 0)$$

Thus, one cannot say anything about the charge independence of nuclear forces because Eq. (29) is easily satisfied:

$$\left(\frac{d\sigma}{d\Omega}\right)^{np}_{90^o} \approx \left(\frac{d\sigma}{d\Omega}\right)^{pp}_{90^o} > \frac{1}{4}\left(\frac{d\sigma}{d\Omega}\right)^{pp}_{90^o} \qquad (58)$$

The apparent symmetry around 90° is in agreement with the predictions of the "rigid" proton model. The large angle p-p and n-p values also agree with this theory. The near equality of the large angle p-p and n-p values shown in Table V implies that the system probably is not dominated by the statistical properties demanded by the "random phase" isotopic spin model.

In conclusion, this new technique using neutron beams and spark chambers as neutron detectors has allowed a detailed investigation of the neutron-proton system. There are numerous future applications of this technique. A few of the experiments using this or similar techniques which are either being planned or are now in progress are (1) a measurement of the n-p cross sections in the 8- to 25-GeV energy region,[77] (2) an investigation of n-p near 1.5 GeV,[78] and (3) a measurement at 991 MeV.[79]

APPENDIX

Scattering Formalism

Given the Schroedinger equation for a spherically symmetric potential,[80] the solution that gives an incident plane wave and a scattered spherical wave is

$$\psi_{\text{scatt}} = e^{ipz} + \frac{e^{ipr}}{r} f(\theta) \tag{A.1}$$

using units such that $\hbar = c = 1$. The most general form of the solution of the radial part of the Schroedinger equation is of the form:

$$\psi = \sum_{\ell=0}^{\infty} \frac{A_\ell}{r} g_\ell(r) P_\ell(\cos\theta)$$

$$= \sum_{\ell=0}^{\infty} \frac{A_\ell}{r} P_\ell(\cos\theta)\left[S_\ell\, e^{i(pr-\ell\pi/2)} - e^{-i(pr-\ell\pi/2)}\right] \tag{A.2}$$

The second term represents an incoming spherical wave and the first term an outgoing wave. In elastic scattering without absorption, the current density in must equal the current density out, as there are no sinks or sources present. Therefore,

$$\left|S_\ell\right|^2 = 1$$

which is usually expressed by letting

$$S_\ell = e^{2i\delta_\ell} \tag{A.3}$$

By expanding Eq. (A.1) and comparing it with Eq. (A.2), one solves for the A_ℓ's and then finds that

$$A_\ell = i^\ell (2\ell + 1)/2ip \tag{A.4}$$

and

$$f(\theta) = \frac{1}{2ip} \sum_{\ell=0}^{\infty} (2\ell + 1) P_\ell (\cos \theta)(S_\ell - 1) \qquad \text{(A.5)}$$

Thus, the total elastic cross section becomes

$$\sigma_{\text{elastic}} = \int \left|f(\theta)\right|^2 d\Omega = \frac{\pi}{p^2} \sum_{\ell=0}^{\infty} \left|S_\ell - 1\right|^2 (2\ell + 1) \qquad \text{(A.6)}$$

In the case of absorption, however, the current density out can be less than the current density in. Thus

$$\left|S_\ell\right|^2 \leq 1 \qquad \text{(A.7)}$$

The total absorption cross section is the difference between the flux in and the flux out:

$$\sigma_{\text{absorption}} = \int d\Omega \left\{ \left| \sum_{\ell=0}^{\infty} \frac{(2\ell + 1)P_\ell (\cos \theta)}{2ip} \right|^2 - \left| \sum_{\ell=0}^{\infty} \frac{(2\ell + 1)P_\ell (\cos \theta)\, S_\ell}{2ip} \right|^2 \right\}$$

$$= \frac{\pi}{p^2} \sum_{\ell=0}^{\infty} (2\ell + 1)(1 - \left|S_\ell\right|^2) \qquad \text{(A.8)}$$

The total cross section is then the sum of the elastic cross section and the absorption cross section:

$$\sigma_{\text{total}} = \frac{\pi}{p^2} \sum_{\ell=0}^{\infty} (2\ell + 1) \left[1 - \left|S_\ell\right|^2 + \left|S_\ell - 1\right|^2\right]$$

$$= \frac{2\pi}{p^2} \sum_{\ell=0}^{\infty} (2\ell + 1)(1 - \text{Re } S_\ell) \qquad \text{(A.9)}$$

Using the assumptions of the optical model, we find

$$\sigma_{\text{total}} = \frac{2\pi}{p^2} \sum_{\ell=0}^{pR} (2\ell + 1)(1 - \eta)$$

$$= \frac{2\pi(1 - \eta)}{p^2} (p^2 R^2 + 1)$$

$$\sigma_{\text{total}} \approx 2\pi (1 - \eta) R^2 \qquad \text{(A.10)}$$

Without using the optical model, the optical theorem can be derived by an examination of Eqs. (A. 5) and (A. 9), yielding

$$\sigma_{\text{total}} = \frac{4\pi}{p} \mathcal{I}m \; f(0^{\circ}) \qquad \text{(A.11)}$$

REFERENCES

1. S. J. Lindenbaum, Proceedings of the Oxford International Conference on Elementary Particles, September 19-25, 1965; p. 93.
2. J. Orear, The Review Lectures from the Institute of Physics and Physical Society Birmingham Conference on Elementary Particles, Imperial College, London (1965); p. 65.
3. R. Wilson, The Nucleon-Nucleon Interaction, Experimental and Phenomenological Aspects (Interscience Publishers, New York, 1963).
4. M. N. Kreisler, F. Martin, M. L. Perl, M. J. Longo, and S. T. Powell III, Phys. Rev. Letters 16, 1217 (1966); M. N. Kreisler, F. Martin, M. L. Perl, M. J. Longo, and S. T. Powell III, Bull. Am. Phys. Soc. 11, 9 (1966); M. N. Kreisler, F. Martin, M. L. Perl, M. J. Longo, and S. T. Powell III, Abstract presented at Oxford International Conference on Elementary Particles, September 19-25, 1965.
5. N. S. Amaglobeli and Yu. M. Kazarinov, Sov. Phys. JETP 7, 37 (1958).
6. N. S. Amaglobeli and Yu. M. Kazarinov, Sov. Phys. JETP 10, 1125 (1960).
7. G. Martelli, H. B. van der Raay, R. Rubinstein, K. R. Chapman, J. D. Dowell, W. R. Frisken, B. Musgrave, and D. H. Reading, Il Nuovo Cimento 21, 581 (1961).
8. R. R. Larsen, Il Nuovo Cimento 18, 1039 (1960); R. R. Larsen, UCRL Report 9292, Lawrence Radiation Laboratory, University of California, Berkeley, California (1962) (thesis-unpublished).
9. M. L. Perl and M. C. Corey, Phys. Rev. 136, 787 (1964); additional references are given in this paper.
10. L. I. Schiff, Quantum Mechanics, 2nd Edition (McGraw-Hill, New York, 1955); p. 96 ff.

11. A. M. Wetherell, Proceedings of the 1965 Easter School for Physicists (CERN Report 65-24), Vol. I, p. 65 (1965).

12. W. Rarita, private communication.

13. R. Levi Setti, Elementary Particles (University of Chicago Press, Chicago, 1963); p. 139.

14. D. E. Damouth, L. W. Jones and M. L. Perl, Phys. Rev. Letters 11, 287 (1963).

15. C. T. Coffin, N. Dikmen, L. Ettinger, D. Meyer, A. Saulys, K. Terwilliger, and D. Williams, Phys. Rev. Letters 15, 838 (1965).

16. R. Crittenden, H. J. Martin, W. Kernan, L. Leipuner, A. C. Li, F. Ayer, L. Marshall, and M. L. Stevenson, Phys. Rev. Letters 12, 429 (1964).

17. C. T. Coffin, private communication.

18. B. Escoubes, A. Fedrighini, Y. Goldschmidt-Clermont, M. Guinea-Moorhead, T. Hofmokl, R. Lewisch, D. R. O. Morrison, M. Schneeberger, S. de Unamuno, H. C. Dehne, E. Lohrmann, E. Raubold, P. Söding, M. W. Teucher and G. Wolf, Phys. Letters 5, 132 (1963).

19. G. Cocconi, V. T. Cocconi, A. D. Krisch, J. Orear, R. Rubenstein, D. B. Scarl, W. F. Baker, E. W. Jenkins, and A. L. Read, Phys. Rev. Letters 11, 499 (1963).

20. W. Chinowsky, G. Goldhaber, S. Goldhaber, T. O'Halloran, and B. Schwarzschild, Phys. Rev. 139, B1411 (1965).

21. M. L. Perl, "Elastic Scattering above 2 GeV/c in Strong Interactions," Lecture Notes (unpublished)(1966); M. L. Perl, private communication.

22. G. Fast, R. Hagedorn, and L. W. Jones, Il Nuovo Cimento 27, 856 (1963).

23. G. Cocconi, Il Nuovo Cimento 33, 643 (1964).